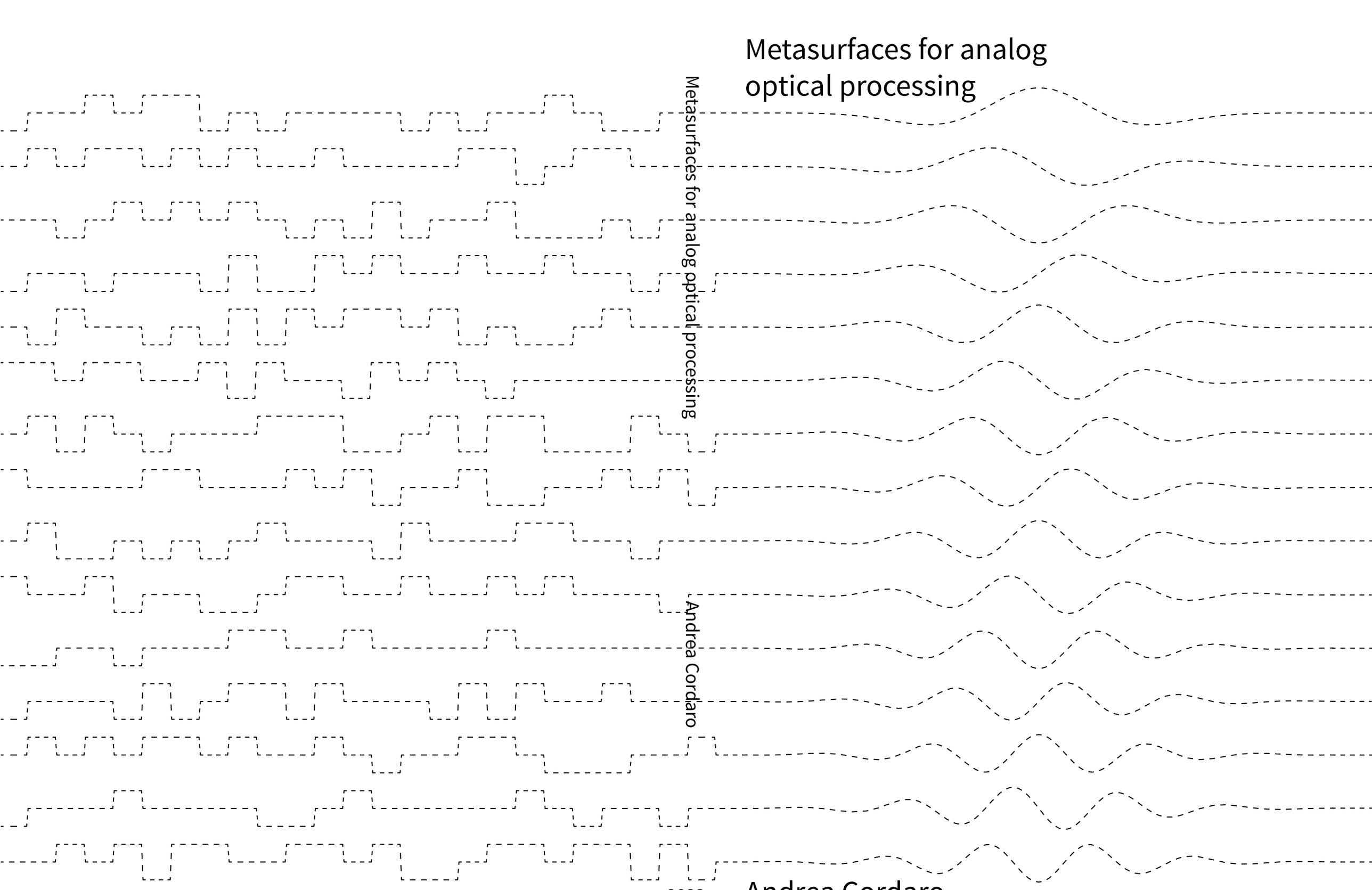
Metasurfaces for analog optical processing
Metasurfaces for analog optical processing
Andrea Cordaro
Andrea Cordaro
2022

METASURFACES FOR ANALOG OPTICAL PROCESSING

HIGH-INDEX DIELECTRIC METASURFACES PERFORMING MATHEMATICAL OPERATIONS

Ph.D. Thesis, University of Amsterdam, June 2022
Metasurfaces for analog optical processing
Concetto Eugenio Andrea Cordaro

Cover: illustration of a digital signal, representing data as a sequence of discrete values (back), transforming into a continuous analog signal (front).

ISBN 978-94-6421-760-5

The work described in this thesis was performed between September 2017 and March 2022 at NWO-institute AMOLF, Science Park 104, 1098 XG Amsterdam, The Netherlands. This work is part of the Dutch Research Council (NWO).

An electronic version of this dissertation is available at `https://ir.amolf.nl/`.

METASURFACES FOR ANALOG OPTICAL PROCESSING

HIGH-INDEX DIELECTRIC METASURFACES PERFORMING MATHEMATICAL OPERATIONS

Academisch proefschrift

ter verkrijging van de graad van doctor
aan de Universiteit van Amsterdam,
op gezag van de Rector Magnificus
prof. dr. ir. K.I.J. Maex
ten overstaan van een door het College voor Promoties ingestelde commissie,
in het openbaar te verdedigen in de Agnietenkapel
op donderdag 2 juni 2022, te 10.00 uur

door

Concetto Eugenio Andrea CORDARO

geboren te Catania

Promotiecommissie

Promotores:	
prof. dr. A. Polman	Universiteit van Amsterdam
prof. dr. A. Alù	The City University of New York
Copromotor:	
dr. J. van de Groep	Universiteit van Amsterdam
Overige leden:	
prof. dr. F.E. Schreck	Universiteit van Amsterdam
prof. dr. A.F. Koenderink	Universiteit van Amsterdam
prof. dr. W.C. Sinke	Universiteit van Amsterdam
prof. dr. R. Quidant	ETH Zürich
dr. G. Tagliabue	EPFL Lausanne

Faculteit der Natuurwetenschappen, Wiskunde en Informatica

Ai nonni

E allora sentì che la notte aveva cangiato odore: era un odore leggero, fresco,
era odore d'erba giovane, di citronella, di mentuccia.

L'odore della notte - Andrea Camilleri

CONTENTS

1

INTRODUCTION

1

THE amount of data that is globally being created, processed, and stored is increasing at a remarkable pace. Furthermore, the advent of new technologies, such as augmented reality (AR), autonomous driving, computer vision, and many other emerging techniques, requires on-the-fly processing of large data files, such as images, at an increasing rate. Image processing is usually performed digitally but the speed and power consumption limits of standard microelectronic components have become a true bottleneck. Analog optical processing provides a promising route that may overcome these limitations. Also, processing signals in the optical domain enables massive parallelization and may potentially avoid unnecessary analog-to-digital conversion.

While a lot of data is nowadays stored, guided, and routed in the optical domain, computing is still mainly performed digitally. The idea of computing optically can be traced back to the early 1960s prompted by pioneering work that ingeniously exploited concepts of Fourier optics [1–4]. Among others, all-optical pattern recognition and optical processing of synthetic–aperture radar (SAR) data were the most successful. The freedom of choice about the linear transformation allowed by a generic spatial filter prompted the idea of designing responses in k–space specific to a certain type of input. This is the concept at the base of matched spatial filters and, in turn, at the core of optical pattern recognition [5–8]. As shown in Figure 1.1a, an optical processor is able to discriminate the character contained in the input image and signals the answer with a bright spot under the letter "P". More elaborate approaches even achieved real–time face recognition [9].

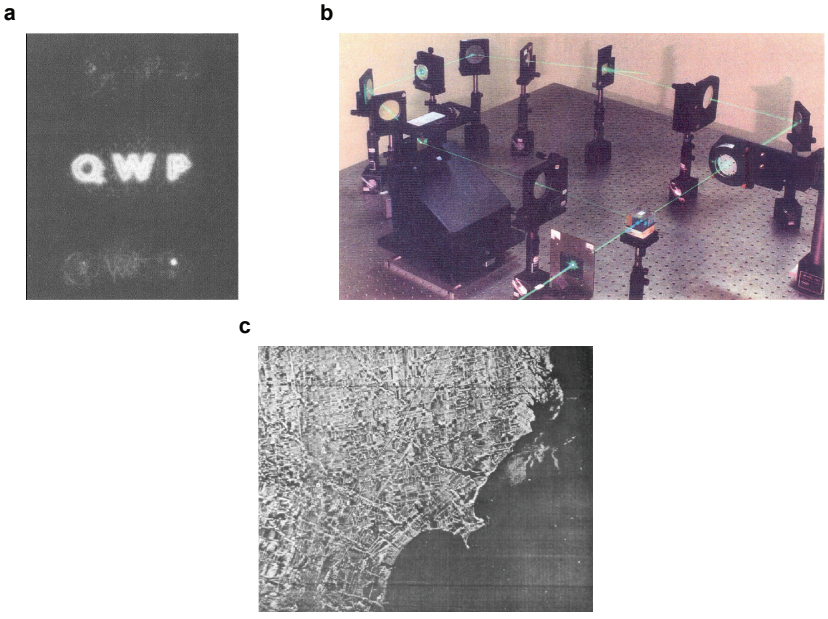

Figure 1.1: **a** A set of matched spatial filters can recognize an input character. The bright spot signals the outcome of the recognition scheme [10]. **b** Photograph of a pattern–recognition system [4]. **c** Synthetic–aperture radar image of Monroe, MI (USA) [2].

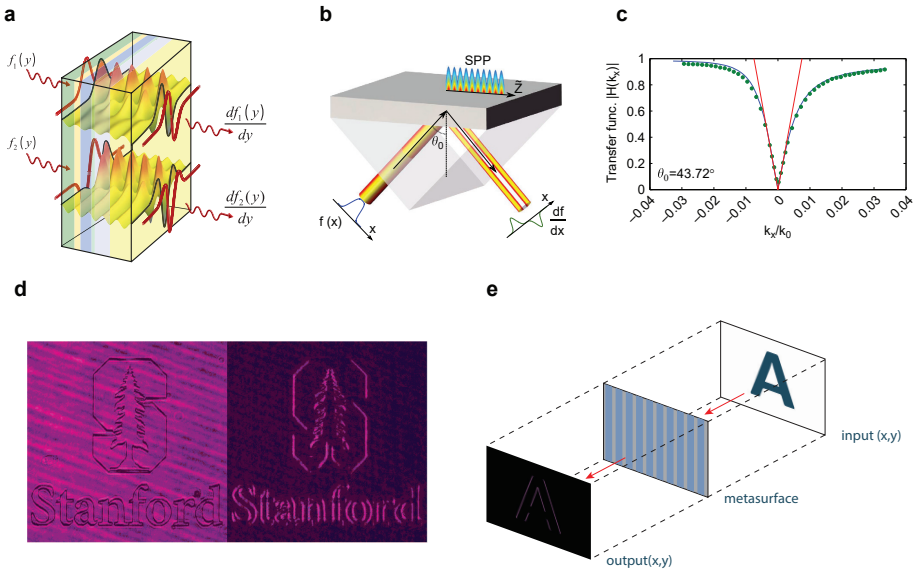

Figure 1.2: **a** Conceptual sketch of a GRIN–based metamaterial performing 1st– or 2nd–order derivative. Re-adapted from Ref. [11]. **b** Plasmonic spatial differentiator exploiting SPP. **c** Spatial transfer function spectra of the sample sketched in b, experimental measurement (dotted lines) and numerical fitting (solid lines). **d** Input image modulated in phase and output image demonstrating edge detection. Panels b-d re-adapted from Ref. [14]. **e** Schematics of a metasurface performing edge filtering in transmission [19].

Optical processors based on Fourier optics were also successfully used to apply linear transformations on data sets that are not human-readable. Specifically, in the mid-1960s, Cutrona et al. [2] found a way to convert the microwave reflectivity signals acquired by special side–looking airplane radars (SARs) into high–resolution pictures (see Figure 1.1c). These elegant all-optical solutions, however, require bulky optical components that are not integrable into nanophotonic or microelectronic systems; hence, as the transistor size scaled-down dramatically and digital computational power skyrocketed, these approaches became quickly obsolete.

The unprecedented control of light propagation over a sub-wavelength thickness that has been recently enabled by optical metasurfaces opens entirely new opportunities for analog optical computing [11–19]. In fact, "computing metasurfaces" may benefit from the speed and low power consumption of optics while being amenable to on-chip integration, thus enabling hybrid optical and electronic data processing on a single chip.

In this context, the work of Silva et al. [11] is groundbreaking as it introduced the idea of using suitably designed metamaterials to perform arbitrary mathematical operations. As conceptually illustrated in Figure 1.2a, a series of optimized graded–index (GRIN) dielectric slabs can transform a given input wave signal $f(y)$ into its 1st– or 2nd–order derivative. Despite the high conceptual impact, this approach remained experimentally unpractical given the complexity of the design.

More recently, a simpler approach based on plasmonic resonances [14] demonstrated

experimentally all-optical edge detection. This work exploits the possibility of coupling to Surface Plasmon Polaritons (SPP) at the interface between air and metal by means of a prism (Kretschmann configuration) [20]. Indeed, for a given metal thickness, light is efficiently coupled only at a specific angle due to momentum matching while the metal surface is completely reflective when this condition is not met. This, in turn, results in a sharp dip in the transfer function of the system which can be used efficiently as a high pass filter (see Figure 1.2b-d): the edges of an input image (Stanford tree logo) modulated in phase are enhanced in the output image as a result of the spatial filtering. The drawbacks of this configuration are the limited numerical aperture (NA) and the use of bulky elements: while the former (NA~ 0.01) implies low spatial resolution and does not allow readily integration in imaging systems (which usually have larger NA), the latter further hinders on-chip implementation.

Sparked by these and other pioneering works, the possibility of shaping the spatial content of an image by suitably engineering a structure's response in k–space prompted a multitude of interesting studies [21–23]. These, either exploit resonant effects of different nature induced by nanopatterns or are based on planar stacks of different materials or even single interfaces. In the latter category, as an example, the well known Brewster effect, where TM-polarized light is not reflected off a single interface at a specific angle, has been exploited to create a zero in the transfer function and thus perform optical differentiation [24]. Similarly, other studies utilize effects observed when an incident polarized beam reflected from a flat surface is subsequently analyzed with a polarizer [25–28]. In this configuration, Zhu et al. [28] established a connection between two-dimensional optical spatial differentiation and a nontrivial topological charge in the optical transfer function. Similar to the example described in Figure 1.2b-d, these elegant solutions are very insightful and further deepen the understanding of analog image processing. Nevertheless, these examples are impractical from an application point of view.

While more difficult to fabricate, spatial differentiators based on thin nanopatterned surfaces (see Figure 1.2e) are more flexible in terms of transfer function design and more applicable to real imaging devices. In theoretical studies, Guo et al. [17, 18] designed photonic crystal slab spatial filters by engineering the photonic band structure, and related guided-mode resonances, to be isotropic at the Γ-point. Using this rationale, they proposed two different structures capable of performing the Laplacian operator [17] and isotropic high-pass, low-pass, band-reject, and band-pass filtering [18]. However, also in these cases the NA~ 0.01. Following up, Zhou et al. [29] realized experimentally a quasi-isotropic second order differentiator based on a Si metasurface. Moreover, the latter was coupled to a metalens obtaining a monolithic compound flat optical elements. Whereas the possibility of vertically stacking metasurfaces opens new exciting prospects also for the design of more complex mathematical operations, this specific combination (metalens and metasurface-based differentiator) does not really translate into a dramatically more compact optical device. The footprint of this monolithic image-processing system remains constrained by the focal distance between the metalens and the imaging camera.

Interestingly, also in this context, structures with judiciously optimized k-space response can be exploited to miniaturize optical systems by "compressing" the free space in between the components [30, 31]. To achieve this, one has to engineer metasurfaces

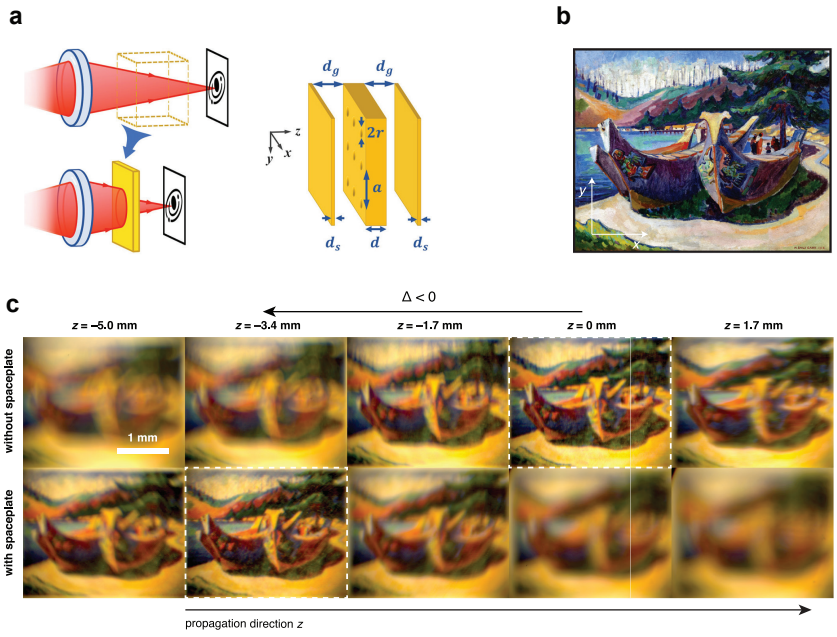

Figure 1.3: **a** Schematics showing a general optical system and the concept of free-space compression. The free-space in the yellow dashed box can be replaced by a smarty designed photonic crystal slab. Re-adapted from Ref. [30]. **b** Painting illuminated with incoherent white light used as image object. **c** The image of the print is formed in either a background medium (glycerol), or through the calcite spaceplate in glycerol. Camera images at various distances z. The spaceplate advances the focal plane of the image by −3.4 mm relative to the glycerol alone. Panels b-c re-adapted from Ref. [31].

with a physical thickness t having the transfer function corresponding to free space propagation over a distance $d > t$. The ratio d/t can be thought of as a compression factor. The transfer function of free space imparts the appropriate phase lag to each plane wave constituting the spatial content of an image without altering the amplitude. Figure 1.3a illustrates schematically how a portion of free space (yellow dashed box) can be substituted by a properly designed photonic crystal slab design [30]. Almost at the same time, Reshef et al. [31] proposed metamaterial "spaceplates" composed of alternating layers of Si and SiO_2 with compression factors up to ~ 4.9. Moreover, they experimentally demonstrated free space compression with a bulk calcite sample. Using a standard imaging system, a 3.4 mm shift in the optimal focus distance was observed (see Figure 1.3b-c). It is worth noting that the spaceplate does not change the magnification.

The concept of optical analog computing goes beyond image processing and filtering. Indeed, fueled by the recent advances in inverse design algorithms [32–37], the group of Engheta demonstrated a metamaterial platform that can solve integral equations in an analog fashion [38]. Specifically, an arbitrary input function is encoded into wave signals that are sent to the structure in Figure 1.4a and are transformed into the integral of the input upon interaction with the metamaterial. The latter is governed by

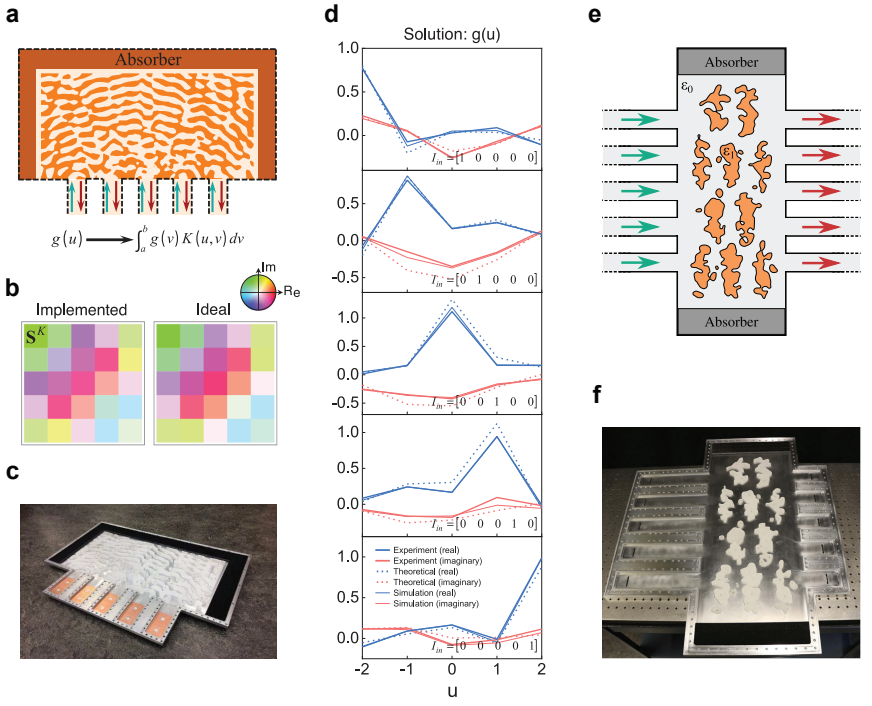

Figure 1.4: **a** Schematics of the analog integral solver in a reflective set-up, consisting of the inverse designed metamaterial kernel and in/out coupling elements to excite and probe the waves. **b** Comparison between the implemented and the desired kernel operator. **c** Photograph of the constructed metamaterial structure. The device width ~ 66 cm. **d** Experimentally measured output signals as the solutions to the integral equation with kernel in panel b. Measurements are compared with the expected theoretical results (dashed lines) and full-wave simulations (thin lines), for applied input signals at each of the five ports (one by one). Panels a-d re-adapted from Ref. [38]. **e** Inverse-designed dielectric distribution that reproduces the two desired mathematical kernels when two waves with two frequencies ω_1 and ω_2 are used. **f** Photograph of the constructed device. Panels e-f re-adapted from Ref. [39].

the scattering matrix of the metastructure that acts as the kernel of the integral operator. Such scattering matrix can be designed at will via inverse design, as shown in Figure 1.4b. Next, by repeatedly returning the signal to the structure with a feedback loop the input function rapidly converges to the solution of the integrals equation associated with the designed kernel.

This approach was experimentally demonstrated at microwave frequencies proving the solution of a generic integral equation. Figure 1.4d highlights the comparison between the experimentally measured output signals (in real and imaginary part) and the theoretical solution to the integral equation featuring the desired kernel in Figure 1.4b for applied input signals at each of the five ports. In a follow-up study [39] the same group investigated and experimentally fabricated a single metastructure that simultaneously solves different integral equations at different frequencies in a parallel way (see

Figure 1.4e-f). It is worth highlighting that, the two devices showcased can also be used to invert arbitrary matrices by suitably designing the kernel. Finally, the main limitation of such analog implementations in the microwave frequency range is the meter-scale device footprint.

MOTIVATION AND OUTLINE OF THE THESIS

The ever-growing need for efficient computing has been driving researchers from diverse research fields to explore alternatives to the current digital computing paradigm. As mentioned, the processing speed and energy efficiency of standard electronics have become limiting factors for novel disruptive applications entering our everyday life, such as artificial intelligence, machine learning, computer vision, and many more.

In this context, analog computing has resurfaced and regained significant attention as a complementary route to traditional architectures. Specifically, the tremendous recent advances in the field of metamaterials and metasurfaces have been unlocking new opportunities for all-optical computing strategies, given the possibility of shaping optical fields in extreme ways over sub-wavelength thicknesses. The absence of bulky optical elements, in turn, enables on-chip integration.

In this thesis, we introduce different metasurface-based platforms that perform image processing tasks or solve complex mathematical problems within a form factor that remains on-chip amenable. In fact, all-optical processing is not meant to replace digital computing but rather to ease its burden, paving the way for hybrid optical and electronic data processing. To achieve this, we design and demonstrate experimentally for the first time all-optical processing metasurfaces that are sub-wavelength in thickness and work in transmission with significantly larger and practical NA, further facilitating application into standard imaging systems (e.g. smartphone cameras). Furthermore, we explore the possibility of tuning the operation imparted on an input signal in a CMOS compatible configuration. Finally, we apply the concept of a wave base integral solver to the optical wavelength range. This, in turn, implies a drastic footprint reduction and thus, again, makes the device on-chip amenable. Moreover, smaller size results in an increased processing speed as light has to travel shorter distances.

In **Chapter 2**, we introduce dielectric metasurfaces that perform optical image edge detection in the analog domain using a sub–wavelength geometry that can be readily integrated with detectors. The metasurface is composed of a suitably engineered array of nanobeams designed to perform either 1^{st}– or 2^{nd}–order spatial differentiation in the visible spectral range. We present a design recipe to tailor the spatial dispersion of the metasurface by introducing a Fano resonance in transmission and the resulting optimized transfer functions are tested numerically demonstrating close-to-ideal performances. Next, the fabrication process is described step by step both for the metasurface and for the images that are used as diapositives. We experimentally demonstrate the 2^{nd}–derivative operation on input images, showing the potential of all-optical edge detection using a silicon metasurface geometry working at a practically relevant numerical aperture as large as 0.35. Finally, we extend the formalism used to 2D operations and unpolarized illumination. Optimized designs performing quasi-isotropic even– and odd–order spatial differentiation are presented and demonstrate numerically edge detection in all directions. Appendix A contains the calculations supporting Chapter 2,

including the coupled–mode theory derivation needed in the design section.

Chapter 3 describes the first proof-of-concept of an electrically controllable metasurface for optical processing. To achieve this, a metasurface sustaining a Fano resonance is coupled to an electrically gated WS_2 monolayer. The suppression of the excitonic resonance in the quasi-two-dimensional material has a big impact on its optical response and thus alters the metasurface transfer function. This rationale is used to design a switchable Fourier spatial filter. Specifically, the device acts as a high-pass filter that can be perturbed by the presence (or absence) of excitons in the WS_2 monolayer. Numerical tests on an optimized design clearly demonstrate reliable edge filtering that can be turned on and off at specific illumination wavelengths. Next, a chip containing several devices is realized and the fabrication steps are discussed in detail. Optical characterization under an applied external bias shows a small modulation of the Fano resonance in reflectance following the same trends of the simulations, showing the potential of the proposed hybrid metasurface–2D-TMD platform. The results shown in the chapter are the first step for optical computing metasurfaces devices with functionalities that can be tuned during operation.

Within **Chapter 4**, we present an ultra-thin Si metasurface-based platform for analog computing that is able to solve Fredholm integral equations of the second kind using free-space visible radiation. A Si-based metagrating is inverse-designed to implement the scattering matrix synthesizing a prescribed Kernel corresponding to the mathematical problem of interest. Next, a semi-transparent mirror is incorporated into the sample to provide adequate feedback and thus perform the required Neumann series solving the corresponding equation in the analog domain at the speed of light. The solution provided by the metasurface in simulation effectively solves the problem of interest and is very close to its ideal counterpart. Electron beam lithography and reactive ion etching provide the resolution required to create a hardware representation of a predefined kernel, with relatively small deviations between experiment and simulations. We optically characterize the output for different input signals showing good agreement with the ideal simulated response and we use the spectral data to retrieve the experimental solution again showing good agreement with theory. Visible wavelength operation enables a highly compact, ultra-thin device that can be interrogated from free-space, implying high processing speeds and the possibility of on-chip integration.

Finally, in **Chapter 5** we apply the gained knowledge about gratings to a completely different task. The results presented in this chapter demonstrate a nanophotonic light trapping scheme aimed at boosting the efficiency of high-performance III-V/Si triple-junction solar cells. A silver diffractive back reflector at the bottom of the cell is designed to steer incoming light to diffraction angles at which total internal refection occurs, in a wavelength range where light is poorly absorbed by Si. The performance dependence on the structural parameters is analyzed and explained with a simple interference model. Next, the impact of the optimized design on the absorption in a thick Si slab is evaluated, highlighting an increase over a planar back–reflector and over the design that is featured in the current world–record cell. Large area Si bottom cells and full two–terminal triple–junction cells are patterned via Substrate Conformal Imprint Lithography (SCIL) and characterized optically and electronically. The experimental external quantum efficiencies and one-sun current-voltage characteristics demonstrate a significant performance

improvement over the planar reference for complete triple-junction solar cells and over the current record cell design for the single-junction Si cells. These results highlight the potential to achieve efficiencies above the current record cell. Moreover, similar strategies can be applied to other Si-based tandem cells where standard random texture is not viable.

Overall, this thesis provides new insights into the design and understanding of metasurfaces for optical processing at visible wavelengths, and presents novel experimental demonstrations that can be realistically applied in hybrid optical–electronic devices opening new exciting opportunities for computing at high speed, low power, and small dimensions.

1

REFERENCES

[1] D. Psaltis and R. A. Athale, *High accuracy computation with linear analog optical systems: a critical study,* Applied Optics **25**, 3071 (1986).

[2] L. J. Cutrona, E. N. Leith, L. J. Porcello, and W. E. Vivian, *On the Application of Coherent Optical Processing Techniques to Synthetic-Aperture Radar,* Proceedings of the IEEE **54**, 1026 (1966).

[3] R. Athale and D. Psaltis, *Optical Computing: Past and Future,* Optics and Photonics News **27**, 32 (2016).

[4] Y. S. Abu-Mostafa and D. Psaltis, *Optical Neural Computers,* Scientific American **256**, 88 (1987).

[5] J. D. Armitage and A. W. Lohmann, *Character recognition by incoherent spatial filtering,* Applied Optics **4**, 461 (1965).

[6] H. J. Caulfield and W. T. Maloney, *Improved discrimination in optical character recognition,* Applied Optics **8**, 2354 (1969).

[7] D. L. Flannery and J. L. Horner, *Fourier optical signal processors,* Proceedings of the IEEE **77**, 1511 (1989).

[8] A. Lugt, *Coherent optical processing,* Proceedings of the IEEE **62**, 1300 (1974).

[9] H. Y. S. Li, Y. Qiao, and D. Psaltis, *Optical Network For Real-time Face Recognition,* Applied Optics **32**, 5026 (1993).

[10] J. W. Goodman, *Introduction to Fourier Optics*, 4th ed. (W. H. Freeman, 2017).

[11] A. Silva, F. Monticone, G. Castaldi, V. Galdi, A. Alu, and N. Engheta, *Performing Mathematical Operations with Metamaterials,* Science **343**, 160 (2014).

[12] A. Pors, M. G. Nielsen, and S. I. Bozhevolnyi, *Analog computing using reflective plasmonic metasurfaces,* Nano Letters **15**, 791 (2015).

[13] D. R. Solli and B. Jalali, *Analog optical computing,* Nature Photonics **9**, 704 (2015).

[14] T. Zhu, Y. Zhou, Y. Lou, H. Ye, M. Qiu, Z. Ruan, and S. Fan, *Plasmonic computing of spatial differentiation,* Nature Communications **8**, 15391 (2017).

[15] H. Kwon, D. Sounas, A. Cordaro, A. Polman, and A. Alù, *Nonlocal Metasurfaces for Optical Signal Processing,* Physical Review Letters **121**, 173004 (2018).

[16] A. Roberts, D. E. Gómez, and T. J. Davis, *Optical image processing with metasurface dark modes,* Journal of the Optical Society of America A **35**, 1575 (2018).

[17] C. Guo, M. Xiao, M. Minkov, Y. Shi, and S. Fan, *Isotropic wavevector domain image filters by a photonic crystal slab device,* Journal of the Optical Society of America A **35**, 1685 (2018).

[18] C. Guo, M. Xiao, M. Minkov, Y. Shi, and S. Fan, *Photonic crystal slab Laplace operator for image differentiation,* Optica **5**, 251 (2018).

[19] A. Cordaro, H. Kwon, D. Sounas, A. F. Koenderink, A. Alù, and A. Polman, *High-index dielectric metasurfaces performing mathematical operations,* Nano Letters **19**, 8418 (2019).

[20] S. A. Maier, *Plasmonics: Fundamentals and Applications*, 1st ed. (Springer US, New York, NY, 2007).

[21] F. Zangeneh-Nejad, D. L. Sounas, A. Alù, and R. Fleury, *Analogue computing with metamaterials,* Nature Reviews Materials **6**, 207 (2021).

[22] S. Abdollahramezani, O. Hemmatyar, and A. Adibi, *Meta-optics for spatial optical analog computing,* Nanophotonics **9**, 4075 (2020).

[23] L. Wesemann, T. J. Davis, and A. Roberts, *Meta-optical and thin film devices for all-optical information processing,* Applied Physics Reviews **8**, 031309 (2021).

[24] A. Youssefi, F. Zangeneh-Nejad, S. Abdollahramezani, and A. Khavasi, *Analog computing by brewster effect,* Opt. Lett. **41**, 3467 (2016).

[25] T. Zhu, Y. Lou, Y. Zhou, J. Zhang, J. Huang, Y. Li, H. Luo, S. Wen, S. Zhu, Q. Gong, M. Qiu, and Z. Ruan, *Generalized Spatial Differentiation from the Spin Hall Effect of Light and Its Application in Image Processing of Edge Detection,* Physical Review Applied **11**, 034043 (2019).

[26] T. Zhu, J. Huang, and Z. Ruan, *Optical phase mining by adjustable spatial differentiator,* Advanced Photonics **2**, 1 (2020).

[27] S. He, J. Zhou, S. Chen, W. Shu, H. Luo, and S. Wen, *Wavelength-independent optical fully differential operation based on the spin–orbit interaction of light,* APL Photonics **5**, 036105 (2020).

[28] T. Zhu, C. Guo, J. Huang, H. Wang, M. Orenstein, Z. Ruan, and S. Fan, *Topological optical differentiator,* Nature Communications **12**, 680 (2021).

[29] Y. Zhou, H. Zheng, I. I. Kravchenko, and J. Valentine, *Flat optics for image differentiation,* Nature Photonics **14**, 316 (2020).

[30] C. Guo, H. Wang, and S. Fan, *Squeeze free space with nonlocal flat optics,* Optica **7**, 1133 (2020).

[31] O. Reshef, M. P. DelMastro, K. K. M. Bearne, A. H. Alhulaymi, L. Giner, R. W. Boyd, and J. S. Lundeen, *An optic to replace space and its application towards ultra-thin imaging systems,* Nature Communications **12**, 3512 (2021).

[32] C. M. Lalau-Keraly, S. Bhargava, O. D. Miller, and E. Yablonovitch, *Adjoint shape optimization applied to electromagnetic design,* Optics Express **21**, 21693 (2013).

[33] A. Y. Piggott, J. Lu, K. G. Lagoudakis, J. Petykiewicz, T. M. Babinec, and J. Vucković, *Inverse design and demonstration of a compact and broadband on-chip wavelength demultiplexer,* Nature Photonics **9**, 374 (2015).

[34] D. Sell, J. Yang, S. Doshay, R. Yang, and J. A. Fan, *Large-Angle, Multifunctional Metagratings Based on Freeform Multimode Geometries,* Nano Letters **17**, 3752 (2017).

[35] A. Y. Piggott, J. Petykiewicz, L. Su, and J. Vučković, *Fabrication-constrained nanophotonic inverse design,* Scientific Reports **7**, 1786 (2017).

[36] T. W. Hughes, M. Minkov, I. A. D. Williamson, and S. Fan, *Adjoint Method and Inverse Design for Nonlinear Nanophotonic Devices,* ACS Photonics **5**, 4781 (2018), 1811.01255 .

[37] S. Molesky, Z. Lin, A. Y. Piggott, W. Jin, J. Vucković, and A. W. Rodriguez, *Inverse design in nanophotonics,* Nature Photonics **12**, 659 (2018).

[38] N. Mohammadi Estakhri, B. Edwards, and N. Engheta, *Inverse-designed metastructures that solve equations,* Science **363**, 1333 (2019).

[39] M. Camacho, B. Edwards, and N. Engheta, *A single inverse-designed photonic structure that performs parallel computing,* Nature Communications **12**, 1466 (2021).

2

DIFFERENTIATION

In this chapter, we introduce dielectric metasurfaces that perform optical image edge detection in the analog domain using a subwavelength geometry that can be readily integrated with detectors.

The first section will briefly review known notions of Fourier optics defining concepts that are useful throughout the thesis. Next, the idea of using a Fano resonant metasurface as a spatial filter is introduced. Section 2.3 describes how to tailor the spatial dispersion of the metasurface by manipulating its leaky modes dispersion and the related Fano resonance asymmetry and linewidth. In Section 2.4 the optimized transfer functions are used to numerically test how well the ideal 1^{st}– and 2^{nd}–order differentiation are approximated by our realistic metasurface designs.

In Section 2.5 the fabrication process is described step by step both for the metasurface and for the images used as diapositives. Next, the fabrication results are presented and the samples' optical characterization is discussed. In Section 2.6 the optical setups used are described along with the measurements. Finally, the experimental 2^{nd}–order differentiation is compared to its ideal counterpart showing significant agreement. The last section extends these concepts to 2D operations and unpolarized illumination, numerically demonstrating edge–detection regardless of the orientation.

Parts of the calculations supporting this Chapter are presented in Appendix A.

The first part of Section 2.1 dealing with Fourier optics follows the notation and the description of Ref. [1].

2.1. FOURIER OPTICS

An arbitrary two–dimensional input wave signal (i.e. an image) can be represented in general by a complex function $f(x,y)$. If the latter function is absolutely integrable (i.e. $f \in L^1(\mathbb{R}^2)$) it can be thought as the superposition of spatial harmonic functions of the form

$$F(\nu_x,\nu_y)\exp\left[i2\pi(\nu_x x+\nu_y y)\right] \tag{2.1}$$

where $F(\nu_x,\nu_y)$ is a complex amplitude and ν_x, ν_y are called *spatial frequencies* and define the harmonic functions' periodicities $\Lambda_x = 1/\nu_x$ and $\Lambda_y = 1/\nu_y$ along the x and y directions. This concept is intuitively shown in Figure 2.1 and can be rigorously formalized as

$$f(x,y) = \iint_{-\infty}^{\infty} F(\nu_x,\nu_y)\exp\left[i2\pi(\nu_x x+\nu_y y)\right]\mathrm{d}\nu_x\mathrm{d}\nu_y \tag{2.2}$$

where $F(\nu_x,\nu_y)$ is the Fourier transform of $f(x,y)$. Next, it is important to show that these harmonic functions can be mapped one–to–one to simple plane waves (see Figure 2.2a). In fact, any arbitrary harmonic function can be seen as a slice of the monochromatic plane wave $U(x,y,z) = A\exp\left[i(k_x x+k_y y+k_z z)\right]$, with wavevector $\mathbf{k} = (k_x,k_y,k_z)$, complex amplitude A and wavelength λ, at the plane $z=0$, provided that $k_x = 2\pi\nu_x$ and $k_y = 2\pi\nu_y$. Vice-versa, the knowledge of the spatial frequencies of a harmonic function completely determines the corresponding plane wave as the knowledge of k_x and k_y is sufficient to determine the k_z via the relation $k_x^2+k_y^2+k_z^2 = 2\pi/\lambda^2$.

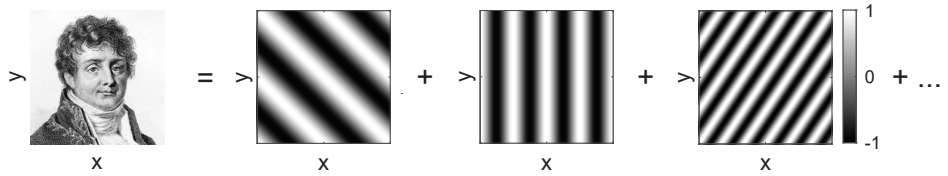

Figure 2.1: An arbitrary image can be expanded into a set of harmonic functions. Here the real part of Eq. (2.1) is plotted for three couples (ν_x,ν_y) and $F(\nu_x,\nu_y) = 1$.

Suppose that a monochromatic plane wave with unit amplitude propagating along the z axis impinges on a thin optical element (e.g. a transparency or a diapositive) with a certain complex transmission function $f(x,y)$. All the harmonic functions composing $f(x,y)$ can be seen as a slice of a corresponding plane wave propagating in a certain direction making angles $\theta_x = \arcsin(\lambda\nu_x)$ and $\theta_y = \arcsin(\lambda\nu_y)$ with the y-z and x-z planes, respectively. Hence, as the plane wave is passing through the transparency it is also dispersed into its spatial components and the transmitted wave $U(x,y,z)$ is a superposition of plane waves

$$U(x,y,z) = \iint_{-\infty}^{\infty} F(\nu_x,\nu_y)\exp\left[i2\pi(\nu_x x+\nu_y y)\right]\exp(ik_z z)\mathrm{d}\nu_x\mathrm{d}\nu_y. \tag{2.3}$$

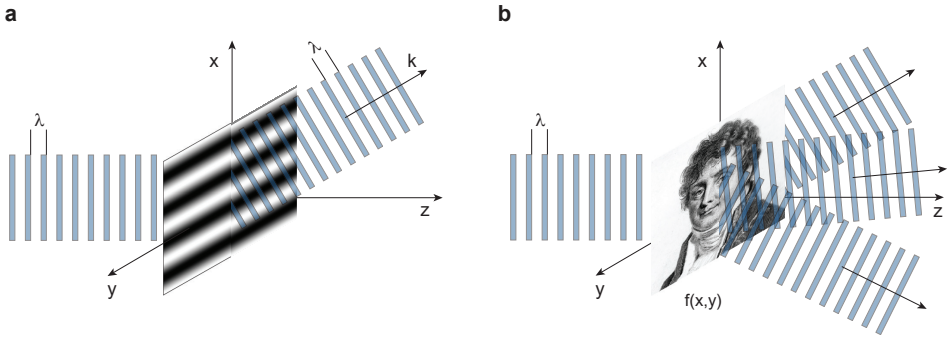

Figure 2.2: **a** A thin optical element that has a complex transmission equal to the harmonic function $\exp[i2\pi\nu_x x]$ bends light at an angle $\theta_x = \text{acrsin}(\lambda\nu_x)$. This is the working principle of a phase grating. **b** the same concept can be extended to an arbitrary complex transmission $f(x,y)$ composed of many harmonic functions.

This bundle of plane waves, schematically illustrated in Figure 2.2b, is the spatial content of the image and contains its information just as $f(x,y)$ does. Manipulating the plane waves composing it is equivalent to performing a certain operation on $f(x,y)$ itself.

The advantage of such theoretical framework becomes clear when dealing with arbitrary traveling waves that are interacting with optical systems. Indeed, if the system response is known for every plane wave composing the arbitrary input signal then the output can be readily calculated. In particular, if the two dimensional optical system relating an input function $f_1(x,y)$ to the output function $f_2(x,y)$ is *linear* and *shift–invariant* (or isoplanatic)[1] then

$$F_2(\nu_x,\nu_y) = H(\nu_x,\nu_y)F_1(\nu_x,\nu_y) \tag{2.4}$$

where $F_1(\nu_x,\nu_y)$ and $F_2(\nu_x,\nu_y)$ are the Fourier transforms of f_1 and f_2 and $H(\nu_x,\nu_y)$ is a function describing the response of the optical system to plane waves called *transfer function*. Intuitively, by modulating its spatial content, $H(\nu_x,\nu_y)$ transforms $f_1(x,y)$ into $f_2(x,y)$.

Among the vast realm of operations, n^{th}–order spatial differentiation is of great appeal in the field of augmented reality and object recognition. In fact, performing the derivative of an image reveals its edges and, in turn, edge detection is a fundamental tool for object recognition. Thus, it is important to assess what transfer function corresponds to the latter operation. Moving to the 1D case, if $f(x)$ is an arbitrary wave input signal, then its n^{th}–order derivative $\frac{d^n f(x)}{dx^n}$ equals $(ik_x)^n F(k_x)$ in the spatial domain, where $F(k_x)$ is the Fourier transform of $f(x)$. Thus, the transfer function corresponding to the n^{th}–order derivative is $H_n(k_x) = (ik_x)^n$.

Proof. $\frac{d^n f(x)}{dx^n} \rightarrow (ik_x)^n F(k_x)$
Suppose $f(x)$ is an arbitrary function $\in L^1(\mathbb{R})$ and let us introduce the notation $\mathscr{F}[f(x)]$

[1] A system is said linear if the response to the sum of any linear combination of inputs is the linear combination of the responses to each input. A system is said isoplanatic if a shift to the input function in space corresponds to the same shift in output.

for the Fourier transform of $f(x)$

$$\mathscr{F}[f(x)] = \int_{-\infty}^{\infty} f(x)e^{-ik_x x}\mathrm{d}x \tag{2.5}$$

then the transform of the first derivative $f'(x)$ of the function reads

$$\mathscr{F}[f'(x)] = \int_{-\infty}^{\infty} f'(x)e^{-ik_x x}\mathrm{d}x. \tag{2.6}$$

This integral can be solved by parts

$$\int_{-\infty}^{\infty} f'(x)e^{-ik_x x}\mathrm{d}x = f(x)e^{-ik_x x}\Big|_{-\infty}^{+\infty} + ik_x\int_{-\infty}^{\infty} f(x)e^{-ik_x x}\mathrm{d}x \tag{2.7}$$

the first term goes to zero since $f \in L^1(\mathbb{R})$ while the second term is just $\mathscr{F}[f(x)]$. Hence

$$\mathscr{F}[f'(x)] = ik_x\mathscr{F}[f(x)] \tag{2.8}$$

and the transfer function corresponding to 1^{st}–order derivative is $H_1 = ik_x$. Repeating this procedure n times demonstrates the property $\frac{d^n f(x)}{dx^n} \rightarrow (ik_x)^n F(k_x)$.

□

As a consequence, 2^{nd}–order differentiation can be achieved by a metasurface that has a parabolic transfer function that modulates the spatial frequencies composing the input signal [1, 2]. If the metasurface can be treated as a simple two–ports optical system (i.e. no extra diffraction channels are opened other than the 0^{th}–order) then the system's transfer function coincides with the scattering matrix element representing transmission S_{21} (see Appendix A for a brief introduction to the scattering matrix formalism). Hence, from now on, $S_{21}(k_x)$ will be also referred to with the term transfer function. As explained in the next paragraph, we introduce the idea of using a Fano–resonant metasurface to design a specific angular transmission response and therefore $S_{21}(k_x)$.

2.2. FANO RESONANCE

In this work, we design and realize optical metasurfaces composed of dielectric nano-beams that are illuminated by light polarized along the beams' direction. We tailor the spatial dispersion of the metasurfaces by controlling the leaky modes guided along the surface [3–6]. Indeed, when the frequency and in-plane wave vector of incident light match one of these quasi-guided modes, an asymmetric Fano line-shape appears in the transmission spectrum [7–9], due to interference with the broad Fabry-Pérot resonance determined by the thickness and fill fraction of the structure.

Figure 2.3a shows the simulated transmission S_{21} spectra of an array of dielectric nano-beams (width w = 182 nm, height h = 123 nm, pitch p = 250 nm and refractive index n = 4 typical for Si) for incident angles ranging from 0 to 0.3 radians (~ 17°). Due to the Fano interference, the transmission swings from 0 to unity within a narrow bandwidth. The sharp response in frequency corresponds to strong non-locality: the spectrum is largely dependent on the incident angle and the transmission minimum shifts

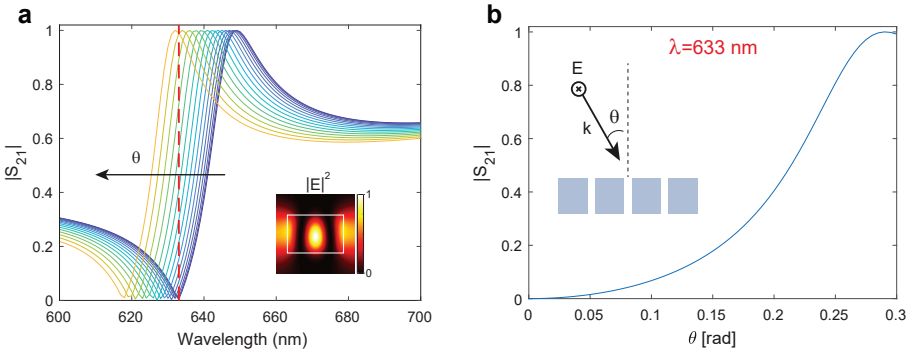

Figure 2.3: **a** Fano-resonant metasurface transmission spectra. Simulated transmission spectra of a metasurface consisting of an array of dielectric nanobeams (width $w = 182$ nm, height $h = 123$ nm, pitch $p = 250$ nm and refractive index $n = 4$) as the incident angle is changed from 0 (blue line) to 0.3 rad (yellow line) in 15 steps. The red dashed line indicates the wavelength of operation ($\lambda = 633$ nm). **b** Cross-cut through panel a showing the transmission at $\lambda = 633$ nm as the incidence angle θ is changed. Insets: electric field amplitude profile within a unit cell at the resonant wavelength; schematic of the proposed structure showing incoming light polarization.

from $\lambda = 633$ nm to $\lambda = 618$ nm over the simulated angular range. The strong amplitude variation in transmission, and the sensitivity to the incoming k-vector, are often undesirable features of resonant metasurfaces, yet here these features enable the use of the metasurface as a Fourier spatial filter, and tailor with large flexibility its angular transmission response and thus transfer function. In fact, by tuning the dispersion of the quasi-guided mode resonance, as well as the Fano line-shape asymmetry and linewidth, it is possible to design an optimized transfer function for a specific excitation wavelength (see Figure 2.3b), as described in the next paragraph.

2.3. DESIGN

The main idea behind our designs of metasurfaces for image processing is that their transfer function can be tuned by introducing a Fano resonance in transmission, and manipulating its dispersion asymmetry and linewidth. In order to prove this property, we use the general formula for a Fano lineshape [8, 10]

$$|S_{21}| = \frac{(\epsilon + q)^2}{\epsilon^2 + 1} m, \tag{2.9}$$

where S_{21} is the scattering matrix element representing transmission for a generic two-port optical system, $m = 1/(1+q^2)$ is a normalization factor, and $\epsilon(k_x) = 2(\omega - \omega_0(k_x))/\Gamma$ is a dimensionless parameter that traces the detuning of the operation frequency ω relative to the resonance at $\omega_0(k_x)$ (dispersing with wavevector k_x), normalized to the linewidth Γ of the resonance. One way to achieve a dispersive resonance frequency is by using one of the leaky-wave resonances of the metasurface. In this case, incident waves are coupled to surface waves propagating along the metasurface through the additional momentum

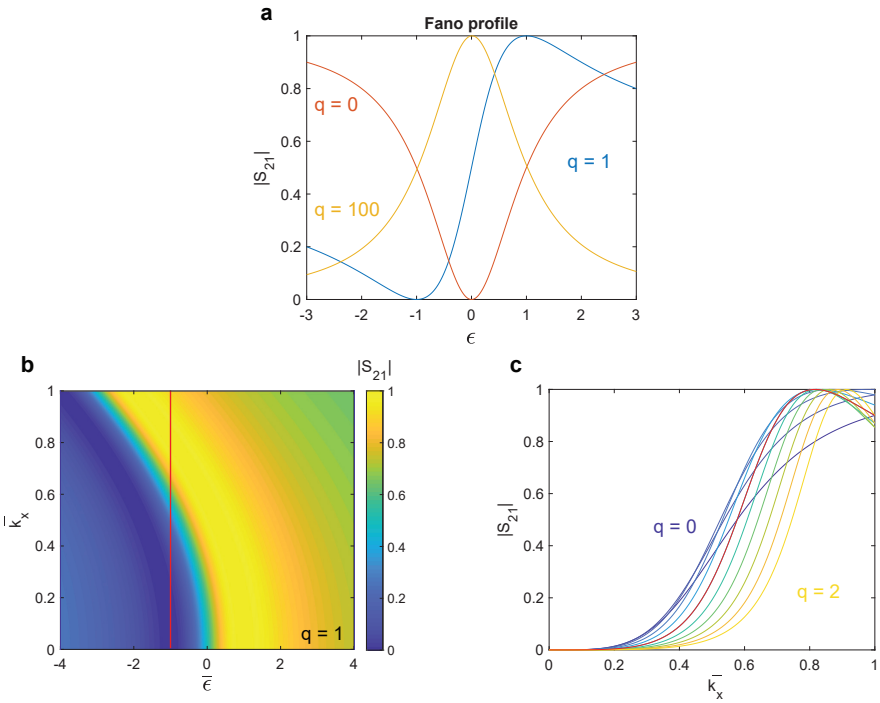

Figure 2.4: **a** Plot of $|S_{21}|$ (from Eq.(2.9)) for $q = 0$ (orange solid line), $q = 1$ (blue solid line), $q = 100$ (yellow solid line). **b** Plot of $|S_{21}|$ (from Eq.(2.9)) as function of $\bar{\epsilon}$ and $\bar{k_x}$ for a parabolic dependence of ω_0 on k_x and fixed values for the shape parameter $q = 1$ and for the linewidth $\Gamma = 1$. **c** Plot of $|S_{21}|$ (from Eq.(2.9)) as a function of $\bar{k_x}$ as q is changed from 0 (blue line) to 2 (yellow line) in steps of 0.2. The red solid line corresponds to the indicated cross-cut through b.

added to them by the metasurface and $\omega_0(k_x)$ generally follows the dispersion of these surface waves. The variable q is a phenomenological lineshape parameter that reflects the contribution of the discrete state in a Fano resonance relative to that of the continuum. Without specifying the nature of the resonance yet we show how it is possible to design the transfer function $|S_{21}(k_x)|$ by tuning the parameters in Eq.(2.9). Starting with q, Figure 2.4a shows how it controls the asymmetry of the Fano lineshape: for $q = 0$ the transmission has a symmetrical dip at the ϵ corresponding to the system resonance; for increasing values of q the lineshape evolves from a completely asymmetric one (data plotted for $q = 1$) to a standard Lorentzian peak (for $q \to \infty$, data not shown). In the most general case, $\omega_0(k_x)$ can be expressed as $\omega_0(k_x) = \omega_0(0) + \sum_n \alpha_n (\frac{ck_x}{\omega_0(0)})^n$ by applying the Taylor expansion at $k_x = 0$. Note that k_x is normalized versus the free-space wavenumber at $\omega_0(0)$ so that all α_n are expressed in the same frequency units. In reciprocal structures $\omega_0(-k_x) = \omega_0(k_x)$, indicating that all the odd-order terms are zero ($\alpha_1 = \alpha_3 = \cdots = 0$). Then, the dominant term in the expansion is the one with $n = 2$, and in Figure 2.4b we plot the transmission as a function of the normalized frequency $\bar{\epsilon} = {}^{2(\omega-\omega_0(0))}/_{\Gamma}$ and normalized wavenumber $\bar{k_x} = {}^{ck_x}/_{\omega_0(0)}$ for fixed values of q and Γ and

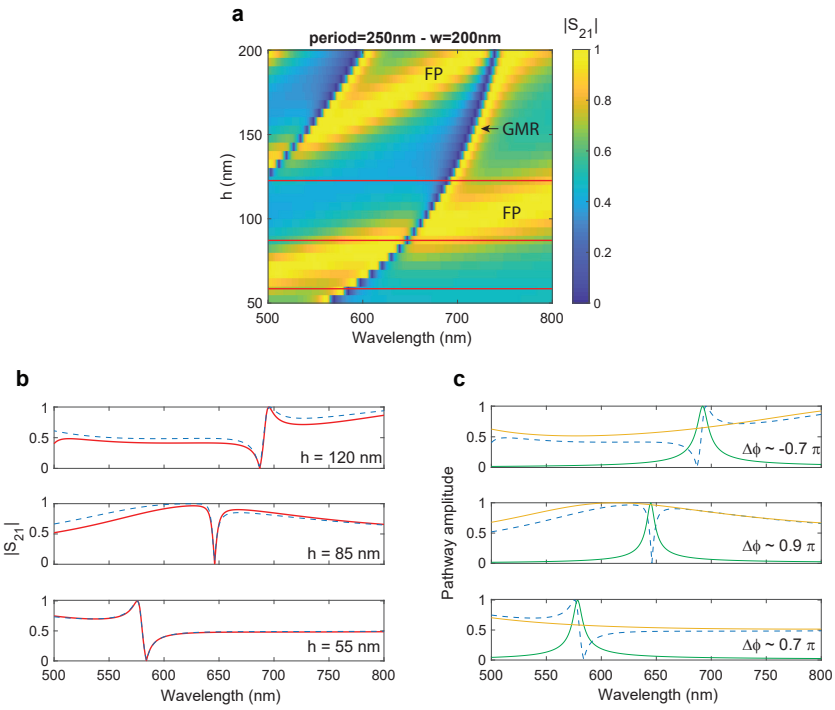

Figure 2.5: **a** Simulated transmission spectra of an array of nanobeams ($n = 4$, $w = 200$ nm, $p = 250$ nm) as the height h is swept from 50 nm to 200 nm. The electric field **E** is polarized along the nanobeams. The labels indicate the spectral position of the guided-mode-resonance (GMR) and of the maxima of the Fabry-Pérot background (FP). **b** Cross–cuts through panel a for $h = 55$ nm, $h = 85$ nm and $h = 120$ nm (red solid lines) and fitted spectra according to coupled-mode theory (blue dashed lines). **c** Amplitude of the direct (yellow) and resonant (green) pathways composing the fits (blue dashed lines).

assuming only the second-order dominant term in the Taylor expansion of $\omega_0(k_x)$ with $\alpha_2 = -3/2$. Taking a cross-cut of the data at the $\bar{\epsilon}$ of the minimum for $k_x = 0$ it is possible to study the behavior of $|S_{21}(k_x)|$ as a function of q. As shown in Figure 2.4c, tuning the asymmetry of the Fano lineshape strongly affects the concavity and shape of the transfer function $|S_{21}(k_x)|$. In particular for $q = 1$ a close-to-parabolic shape can be obtained, similar to what is desired for the optimized 2^{nd}–order differentiation. It is important that, in actual realizations, also q and Γ might disperse with k_x but for the sake of simplicity this is not taken into account here.

Next, we discuss how the structural parameters of the metasurface are connected to the variables just described. While there is no trivial way to design $\omega_0(k_x)$, it is straightforward to tune q. Figure 2.5a shows the simulated transmission spectra of an array of nanobeams (refractive index $n = 4$) with fixed width ($w = 200$ nm) and periodicity ($p = 250$ nm) as the height h is swept from 50 nm to 200 nm. It is easy to notice how the asymmetry of the Fano lineshape changes as h is increased (see Figure 2.5b). The Fano lineshapes for this type of metasurfaces are induced by the interference between sharp

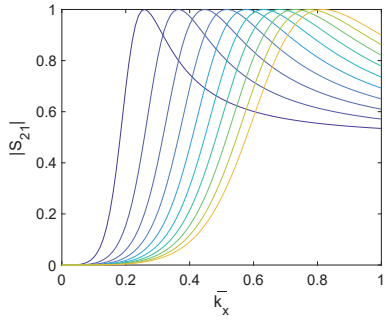

Figure 2.6: Plot of $|S_{21}|$ (from Eq.(2.9)) as function of $\bar{k_x}$ for a parabolic dependence of ω_0 on k_x with $\alpha_2 = -3/2$ and a fixed shape parameter $q = 1$ as Γ is increased from 0.1 (blue line) to 1 (yellow line) in steps of 0.1.

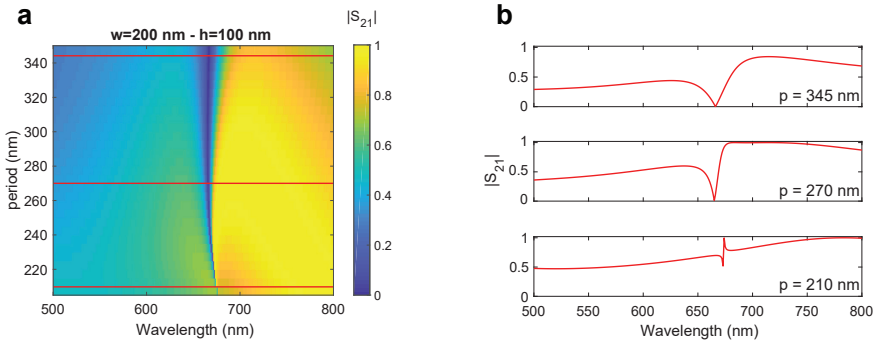

Figure 2.7: **a** Simulated transmission spectra of an array of nanobeams ($n = 4$, $w = 200$ nm, $h = 100$ nm) as the period p is swept from 205 nm to 350 nm. The electric field **E** is polarized along the nanobeams. **b** Cross-cuts through panel a for $p = 210$ nm, $p = 270$ nm and $p = 345$ nm (red solid lines).

quasi-guided modes that can be launched in-plane along the structure and a broader Fabry-Pérot (FP) background determined by the fill fraction F and the height h of the structure; these two different light pathways correspond to spectral features that are easily distinguishable in Figure 2.5a (see labels). Changing the height of the structure shifts the frequency response of both pathways and thereby controls the amplitude and phase at which they interfere to generate the asymmetric lineshape. This property is formalized in Coupled-Mode Theory (CMT) [11, 12] that provides an analytical form for the transmission of a system with a guided-mode resonance (see Appendix A)

$$S_{21} = t \pm \frac{-(r \pm t)\gamma}{i(\omega - \omega_0) + \gamma}, \tag{2.10}$$

where ω_0 is the resonance frequency, γ is the radiative leakage rate and r and t are the reflection and transmission Fresnel coefficient for a uniform slab of index $n_{\text{eff}} = [(1-F)n_0^2 + Fn^2]^{1/2}$ (with $n = 4$ and $n_0 = 1$) [13]. Thus, the first term in Eq.(2.10) represents the broad FP background while the second term represents the guided-mode-resonant

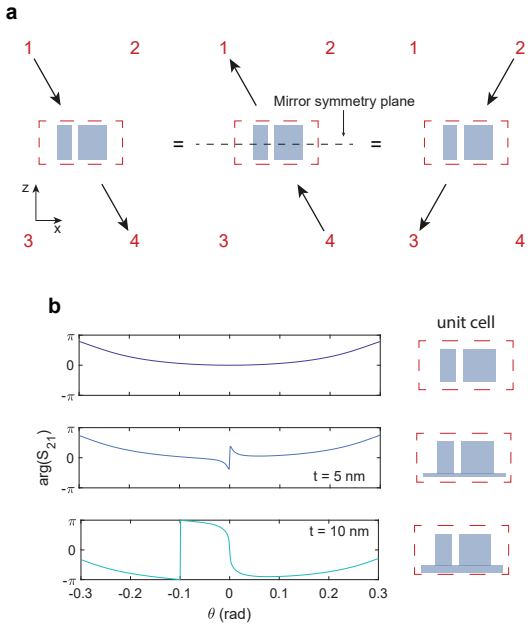

Figure 2.8: **a** The transmission response is still symmetric if only one of the symmetries is broken. **b** Simulated transmission phase of an array of nanobeams ($n = 4$, $w_1 = 40$ nm, $w_2 = 108$ nm, gap between the wires equal to 16 nm, $h = 100$ nm and $p = 250$) as the residual thickness t is increased from 0 to 10 nm to break the vertical symmetry. The electric field **E** is polarized along the nanobeams.

pathway. Since these two terms are complex valued it is important to study their phase difference $\Delta\phi = \arg(t) - \arg(\pm\frac{-(r\pm t)\gamma}{i(\omega-\omega_0)+\gamma})$ on resonance to understand how the two pathways combine and hence determine the final asymmetry of the Fano resonance. To do this, we fit the simulated transmission of Figure 2.5a for three different heights (see Figure 2.5b–c) using Eq.(2.10). Figure 2.5c shows the amplitude of the two pathways that are composing the fitted functions (dashed blue lines) as well as their phase difference $\Delta\phi$ at the resonance wavelength (inset) highlighting the importance of this phase lag and its influence on the final resonant lineshape. This analysis shows that thickness tuning provides a direct handle on the asymmetry parameter in $|S_{21}|$, which in turn gives control over the curvature of the transfer function around $k_x = 0$.

Next, we assess how to control the numerical aperture of operation. This is directly controllable by the linewidth parameter Γ in Eq.(2.9). Figure 2.6 shows $|S_{21}(k_x)|$ for fixed q and a parabolic $\omega_0(k_x)$ as Γ is increased. As the linewidth of the resonance is increased also the metasurface operational wavevector range is expanded. Hence, Γ allows direct tuning of the metasurface numerical aperture (NA). In simulation, it is possible to tune the linewidth by changing the array periodicity while keeping the nanobeam dimensions fixed, as shown in Figure 2.7a–b. However, an upper bound on periodicity is set by the onset of higher order diffraction channels at large pitches. These would complicate the design of the transfer function and lower the efficiency.

In the case of 1st–order differentiation, not only the amplitude of the transfer function $|S_{21}(k_x)|$, but also the phase $\arg(S_{21}(k_x))$ is important. In fact, such operation requires a response that has odd–symmetry around the sample normal $S_{21}(-k_x) = -S_{21}(k_x)$. In other words, the transmission phase for positive k_x values should be phase-shifted by π compared to that of negative k_x values. In order to achieve this asymmetric phase response, it is necessary to break the unit cell's mirror symmetry both along the propagation (i.e. z–axis) and transverse (i.e. x–axis) directions. Invoking Lorentz reciprocity, it is easy to show that breaking the mirror symmetry only along the x–axis is not sufficient (see Figure 2.8a) to generate a transmission response of odd symmetry. Indeed, the transmission at negative incidence angles (from port 1 to 4) S_{41} has to be equal to the transmission from port 4 to 1, i.e. S_{14}, by reciprocity (see Equation (A.9) of Appendix A). Yet the latter has in turn to be equal to S_{32} if the symmetry along the z–axis is not also broken. Thus, with asymmetry along x yet mirror symmetry in z, the transmission still remains a symmetric function of k_x. This fact can also be observed in simulation as shown in Figure 2.8b. Adding a residual layer of thickness t below the nanobeams breaks the symmetry along the z–axis, and thereby provides the odd–symmetry system response required for odd–order differentiation. Simulations show that the thickness t provides control over the phase asymmetry (see Figure 2.8b).

2.4. OPTIMIZED TRANSFER FUNCTIONS AND NUMERICAL TESTS

Using the insight gained from the previous paragraph it is possible to design metasurfaces with specific transfer functions optimized for 1st– and 2nd–order spatial differentiation.

Figure 2.9a shows the simulated transmission amplitude $|S_{21}|$ and phase $\arg(S_{21})$ as a function of the in-plane wave vector k_x, normalized by the free space wavevector k_0 at the design wavelength $\lambda = 633$ nm for a metasurface composed of dielectric nanobeams (width $w = 182$ nm, height $h = 123$ nm, pitch $p = 250$ nm and refractive index $n = 4$ typical for Si). In this design, optimized to perform 2nd–order differentiation, the angular response is close in amplitude to the ideal parabolic shape. The phase response shows a variation of approximately 0.9π, deviating at high angles from the ideal constant phase response, but still providing a close–to–ideal second derivative response.

Our metasurface design has two key features that distinguish it from earlier designs [14–16]. First of all, the metasurface operational numerical aperture is large (NA $\simeq 0.35$). This feature enables processing images with high spatial content and hence high resolution. Moreover, it allows for direct implementation into standard imaging systems with similar NA, for instance by placing the metasurface right in front of a charge-coupled device (CCD) detector array, without the need for additional imaging lenses. This is a major advance over previously explored spatial differentiation schemes that operate at an NA that is $\simeq$25 times smaller than what we demonstrate here. Second, the transmission in our design reaches unity at large wavevectors, enabling close-to-ideal image transformation efficiency, significantly larger than earlier attempts at realizing image processing metasurfaces.

Next, we use the optimized transfer function to numerically test how well the ideal 2nd–order differentiation is approximated by our realistic metasurface design. To this end, some simple input functions (see Figure 2.9b-e) are discretized into 1000 pixels and

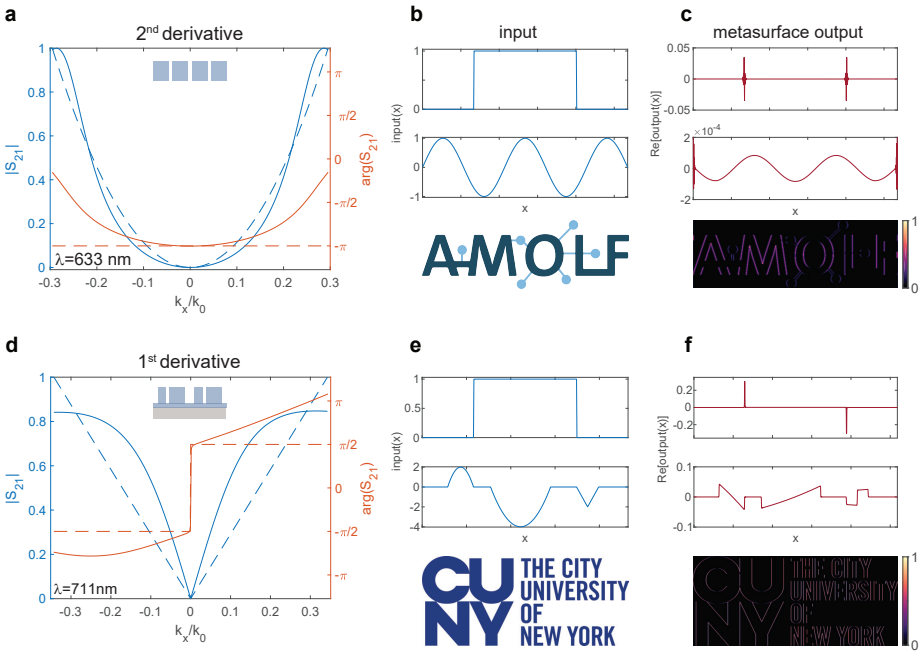

Figure 2.9: Simulated transfer functions of dielectric metasurfaces performing 1st– and 2nd–order spatial differentiation. **a** Transmission amplitude $|S_{21}|$ (solid blue line) and phase $\arg(S_{21}(k_x))$ (solid orange line) for the metasurface optimized for 2nd-derivative operation (sketched in the inset) at $\lambda = 633$ nm. The simulated transfer function is compared to the ideal case (dashed lines). The transmission reference plane is set such that the transmission phase at normal incidence equals $-\pi$. **b** Rectangular and sinusoidal input functions and 2D image that are used to numerically test the metasurface operation. The signal is discretized into 1000 pixels with individual pixel size set such that the Nyquist range matches the operational range in k-space of the metasurface. **c** Metasurface output for the input in b. For the 2D image, differentiation is performed line by line along the x-axis. **d-f** Same as a-c, but for 1st–derivative operation (metasurface geometry sketched in the inset) compared to the ideal case (dashed lines) at $\lambda = 711$ nm. The transmission reference plane is set such that the transmission phase at normal incidence is 0.

Fourier transformed. The pixel size Δ_x set such that the Nyquist frequency (i.e. the spatial sampling frequency) $\nu_n = 1/\Delta_x$ is equal to $k_{\max}/2\pi$ where $k_{\max}$ is the maximum k_x–vector that the metasurface can process. This choice ensures that the Nyquist range $[-\nu_n, \nu_n]$ matches the operational range in k-space of the metasurface and physically means that the test images are projected onto the metasurface under an NA that matches that of the metasurface. Once the input function is Fourier transformed, it is multiplied by the transfer function and finally, inverse Fourier transformed (recall Eq. (2.4)).

Figure 2.9c shows the calculated response for rectangular and sinusoidal input functions shown in Figure 2.9b. The metasurface output clearly shows the edges of the rectangular input profile and flips the sinusoidal input function as expected. It is also possible to process arbitrary 2D images by performing the 2nd derivative line by line. The edges of one of our institutions' logos are clearly visible in Figure 2.9c. Notice that dif-

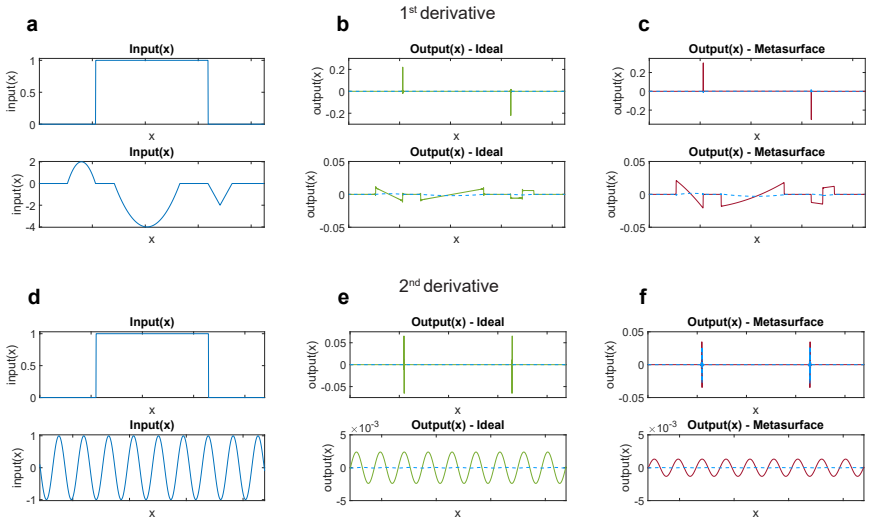

Figure 2.10: Metasurfaces performing 1st– and 2nd–order spatial differentiation. **a-d** Input functions used to numerically test the metasurface operation. The signal is discretized into 2048 pixels with individual pixel size set such that the Nyquist range matches the operational range in k-space of the metasurface. **b-e** Ideal output for the input in panels a-d. **c-f** Metasurface output for the input in panels a-d. The solid line represents the real part while the dashed line represents imaginary part of the output.

ferentiation is performed only along the x-axis for this 1D geometry, hence the edges along the same direction are not detected. To illustrate the flexibility of the metasurface image processing concept, Figure 2.9d shows the optimized transmission for a metasurface performing 1st–order differentiation, which corresponds to the transfer function $S_{21}(k_x) = ik_x$ in the Fourier domain. In order to achieve such an operation with odd symmetry in space, we designed an asymmetric metasurface composed of an array of Si nanobeams with a unit cell ($p = 300$ nm) consisting of nanobeams with two different widths ($w_1 = 48$ nm, $w_2 = 96$ nm, $h = 165$ nm and gap between the nanobeams 53 nm), placed on a thin silicon layer (thickness $t = 35$ nm) on a semi-infinite Al_2O_3 substrate. As explained earlier, by Lorentz reciprocity, it is easy to prove that the unit cell has to be asymmetric both along the direction of propagation and transversally. Furthermore, the asymmetry in the phase response of the transfer function can be tuned with t, enabling the required π phase jump at $k_x = 0$. In this case, the experimental optical constants (including losses) for the two materials have been used in the simulations [17, 18]. The simulated transfer function amplitude shows a linear behavior over a wavevector range up to $k_x/k_0 = 0.1$ (6°), above which it gradually bends away from the ideal case. For large angles, the transmission saturates below unity due to intrinsic absorption in Si. Figure 2.9e-f shows the calculated metasurface output for rectangular, parabolic and triangular input functions. The input slope changes and a nearly linear derivative for the parabola are clearly resolved. Furthermore, processing the logo results in clear detection of the edges in the x-direction consistently with 1st–derivative operation.

In order to further corroborate the performance of the designs, we compare the metasur-

face response to its ideal counterpart in Figure 2.10. It is easy to notice that the metasurfaces' output is very close to the ideal one both in real and imaginary part. The transfer functions used for the metasurface outputs are the same as in Figure 2.9a-d. Regarding the ideal differentiation, $S_{21} = ik_x$ and $S_{21} = -k_x^2$ were used as transfer functions for 1st– and 2nd–order derivative respectively.

To conclude, the results shown in this section demonstrate the possibility of designing metasurfaces featuring transfer functions that allow even– and odd–symmetric operations. These optimized designs are composed of nanostructures that can be realistically fabricated and experimentally tested, as shown in the next section.

2.5. FABRICATION

In order to demonstrate experimentally the concept of performing all–optically mathematical operations via metasurfaces, two different samples ought to be fabricated: the metasurface itself but also the image that is projected onto it. Both sample fabrication procedures involve electron beam lithography (EBL). This technique consists in scanning a focused electron beam on a surface coated with a layer of e-beam resist, a particular material that undergoes a change in solubility once exposed. Next, immersing the sample in a selective solvent will dissolve the exposed areas thus creating a mask for a successive etching that will eventually define the structure.

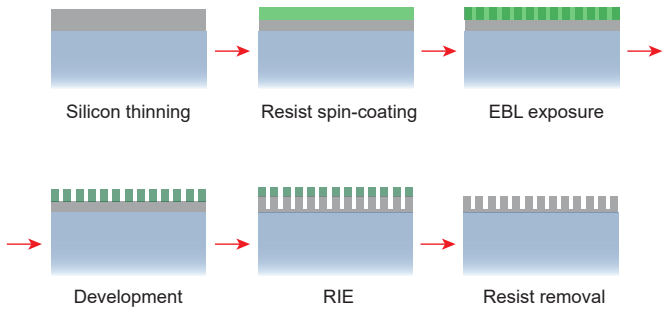

Figure 2.11: Fabrication steps needed for the metasurface sample.

Starting with the metasurface fabrication, we opted to fabricate the optimized geometry for 2nd–order differentiation as this symmetric structure is easier to obtain compared to the fully asymmetric one optimized for 1st–order differentiation.

The platform used for this sample is Silicon on sapphire (Al_2O_3). Indeed, high purity c-Si can be hetero-epitaxially grown on synthetic sapphire wafers and this CMOS technology is now well developed and commercially available. Using the experimental indices for the two materials [17, 18], the optimized dimensions for this design are w = 206 nm, h = 142 nm, and p = 300 nm with a thin residual Si layer (thickness t = 20 nm) that is intentionally left between the pillars. This layer is essential to achieve optimum transmission for large wavevectors, as discussed later. In the following, the detailed fabrication procedure is explained step by step.

- c-Si on Al_2O_3 substrates were purchased from MTI corp. The Si(100) layer is 500 nm–thick, polished (surface roughness < 2.5 nm) and undoped. The sapphire (orientation: R–plane) substrate is 0.46 mm–thick and double–side polished (surface roughness < 0.3 nm on the front side and optical grade polish on the back).

- The substrate was cleaned in base piranha and the c-Si was etched to the final metasurface thickness via Reactive Ion Etching (RIE) using Oxford Instrument's PlasmaPro 100 Cobra ICP and a three–step process employing Cl_2, HBr and O_2. The first steps is used to remove the native oxide on the Si layer:

Cl_2 gas flow	50 [sccm]
pressure	7 [mTorr]
Set temperature	60 [°C]
RIE forward power	30 [W]
ICP power	750 [W]
time	11 [s]

Next, the system is pumped out for 2 minutes in order to completely remove any residual Cl_2. The third step etches the Si layer:

HBr gas flow	48 [sccm]
O_2 gas flow	2 [sccm]
pressure	7 [mTorr]
Set temperature	60 [°C]
RIE forward power	30 [W]
ICP power	750 [W]
time	89 [s]

The recipe is run first on a dummy wafer to condition the chamber and then on the actual sample. The etch rate of the entire process is $h_{\text{etched}}(t) = 45 \pm 18 + (3.7 \pm 0.24)t$ where h_{etched} is the etched thickness in [nm] and t is the Si–step etch time in [s] (the Cl_2 etch step time is kept constant and partially etches also Si). The final c-Si thickness is checked with Filmetrics F20, an optical characterization tool that fits the Fabry–Pérot sample spectrum to obtain the thickness.
This fabrication step is rather sensitive since the actual etch rate depends on the chamber conditions and on other poorly controllable parameters. Moreover, since the etch time is very long a small fluctuation on the etch rate can cause a relevant change in the final thickness.

- The substrate was cleaned again in base piranha and a 200 nm-thick layer of CSAR 62 (AR-P 6200, 9% in anisole) positive-tone resist (ALLRESIST GmbH) was spin-coated at 4000 rpm and baked for 2 minutes at 150°C.

- Lines were fabricated in the CSAR layer by exposure using a Raith Voyager lithography system (50 kV, dose 145–150 $\mu C/cm^2$) and development in Pentyl–acetate (60 s) and o–Xylene (10 s). One important detail concerning this step is that the nano–beams have to be aligned along the optical axis of sapphire during e-beam exposure. This is due to the fact that sapphire is a birefringent material and therefore has a refractive index that depends on the polarization impinging light. If the nanobeam arrays are aligned to the optical axis, light polarized along the wires length experiences only one refractive index.

- The pattern was then transferred into the c-Si by a three-step RIE process employing Cl_2, HBr and O_2. The latter is almost identical to that described previously except for the ratio between the fluence of O_2 and HBr gases. This has an influence on the slanting of the final structure sidewall and an optimum slanting of only 20 nm was achieved with 48.7 sccm for HBr and 1.4 sccm for O_2.

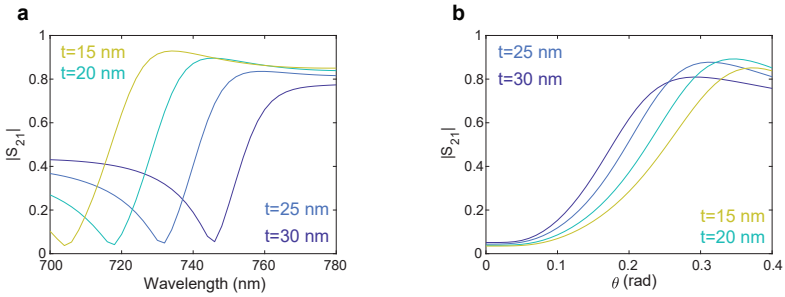

Figure 2.12: **a** Metasurface transmission spectrum for different residual thicknesses t. **b** Metasurface angular transmission $|S_{21}|$ at the wavelength of the minimum for different values of t

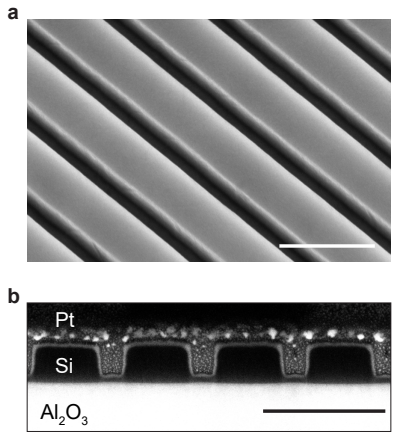

Figure 2.13: Experimental Si metasurface performing 2$^{\text{nd}}$–order spatial differentiation. **a** Tilted SEM image of the Si metasurface performing the 2$^{\text{nd}}$–derivative operation. **b** SEM image of a FIB cross section of the same metasurface showing the Si nanobeams (capped by Pt for imaging purposes) on an Al_2O_3 substrate. The scale bar is 400 nm for both panels.

Again, the etch time is an important parameter as it defines the residual thickness left in between the nanobeams. This, in turn, has an impact on the transmission spectra and the metasurface angular response, as shown in Figure 2.12. In fact, both the GMR and the Fabry–Pérot background are influenced by a change in the residual thickness t.

- The sample was finally cleaned in anisole at 65°C followed by an acid piranha cleaning.

Figure 2.13 shows the result of the fabrication procedure. The sample is uniform over large areas (500 μm) with very low sidewall roughness. The FIB cross-section in Figure 2.13b highlights the low sidewall slanting and the thin (thickness $t \simeq 22$ nm) Si residual layer.

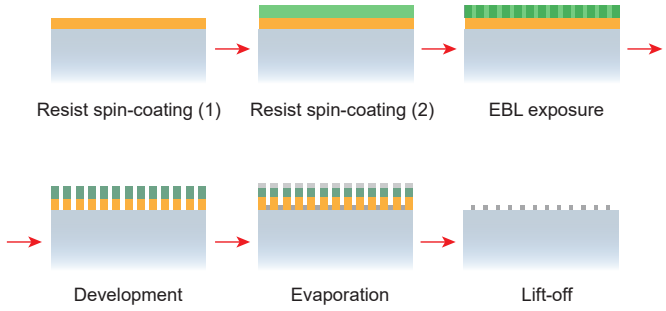

Figure 2.14: Fabrication steps needed for the images sample.

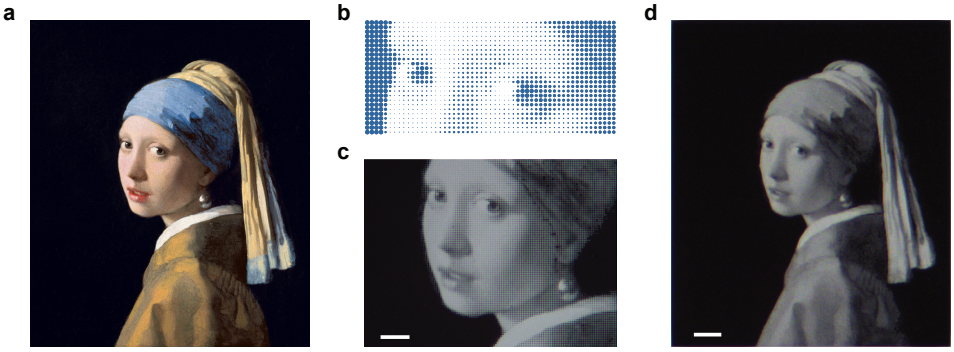

Figure 2.15: **a** *Meisje met de parel*, Johannes Vermeer circa 1665, oil on canvas, Mauritshuis, The Hague, Netherlands. **b** An array of suitably sized dots can imitate a gray-scale gradient. **c-d** Optical microscopy images of the final sample (scalebar 20 μm).

The fabrication procedure just described is an example of a top–down process in which a nanostructure is carved into a certain material. On the other hand, in order to fabricate the image samples, a bottom–up process is used, as schematically shown in Figure 2.14. The following steps were performed to fabricate the samples:

- Glass slides (24×24 mm) were cleaned in base piranha.
- A bilayer of MMA (MMA(8.5)MAA EL9, 150 nm) and PMMA (PMMA 950k A8, 95 nm) was spin-coated and baked at 150°C and 180°C for 2 minutes respectively. The thickness of the layers has to be chosen carefully, very thick layers would lift off easily in anisole but do not allow high resolution due to beam broadening during e-beam exposure and excessive MMA undercutting during development.
- The images were fabricated in the resist layer by exposure using Raith Voyager lithography system (50 kV, dose 550 $\mu C/cm^2$) and development in MIBK:IPA (1:3 for 90 s).

- A 40 nm thick Cr layer was evaporated using an in-house built thermal evaporator.
- The residual resist was lifted-off in anisole at 65°C facilitating the process with an ultra–sonicator.

Following this procedure, two-tone and gray–tone images were fabricated. To obtain the gradient effect in the gray–tone image, the famous painting *Meisje met de parel* (J. Vermeer, circa 1665) has been discretized into an array of suitably sized Cr disks. The final result looks homogeneous if low magnification ($< 60x$) is used in a standard optical microscope (see Figure 2.15).

2.6. OPTICAL CHARACTERIZATION

The last experimental effort consists in characterizing optically the fabricated samples. First, the metasurface transfer function has to be measured. Second, the image processing capabilities are tested by projecting the image sample onto the metasurface. These two different measurements are performed with two different setups that will be described in the following, along with the corresponding results.

2.6.1. INTEGRATING SPHERE

To experimentally determine the transfer function of the metasurface we measure angle–resolved transmission spectra. The data was collected with a Spectra Pro 2300i spectrometer equipped with a Pixis 400 CCD. The sample was mounted on a rotating stage and illuminated with collimated white light from a SuperK EXTREME/FIANIUM supercontinuum laser. The transmitted light was collected by an integrating sphere and sent to the spectrometer through a multimode fiber (Figure 2.16a). Light was polarized along the nanobeams' direction.

Figure 2.16b shows the measured transmittance ($T = |S_{21}|^2$) spectra as the incident angle is changed from 0 to 25°. In agreement with the simulated data in Figure 2.3, the Fano resonance shifts to shorter wavelengths as the angle is increased. The transmittance minimum is observed at $\lambda = 726$ nm for normal incidence and amounts to 2.2%, the residue attributed to minor fabrication imperfections. Figure 2.16c shows the transmittance as a function of the in-plane wavevector at $\lambda = 726$ nm, derived from the data in Figure 2.16b. The corresponding transmission amplitude ($|S_{21}|$) derived from the data is also plotted, along with the ideal parabolic amplitude response.

The overall trend with increasing transmittance as a function of angle is well reproduced experimentally, with a significant residual transmittance at normal incidence and a maximum amplitude at the largest angle of 0.84, which is mostly determined by the absorption in Si. Employing alternative high-index materials could further enhance the transmission for large angles.

2.6.2. DUIMELIJN FOURIER MICROSCOPE

In order to assess the processing capabilities of the metasurfaces, an image is projected onto the sample and the outcome is inspected on a CCD camera using the optical setup

Duimelijntje is a fairy tale by the danish writer Hans Christian Andersen (published in 1836) and also the name given to the setup.

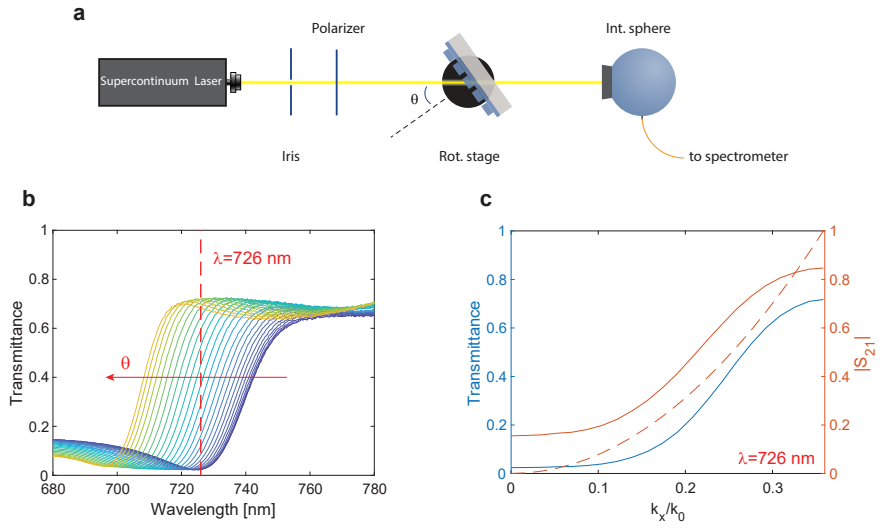

Figure 2.16: Experimental metasurface transmission. **a** Schematic of the setup used to measure angle-resolved transmission spectra. **b** Measured transmission spectra of the metasurface in Figure 2.13 as the angle of incidence is increased from 0 (blue line) to 25° (yellow line) in 25 steps. **c** Measured transmittance $|S_{21}|^2$ (blue line) and corresponding calculated transmission amplitude $|S_{21}|$ (orange solid line) as function of incident in-plane wave vector k_x/k_0 at $\lambda = 726$ nm. The dashed orange line shows the ideal parabolic transfer function for $|S_{21}|$.

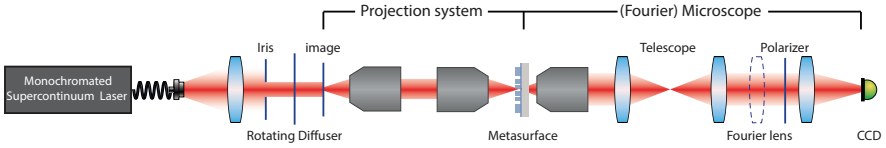

Figure 2.17: Projection system coupled to a standard microscope with Fourier imaging capabilities. The dashed contour represents the removable Bertrand lens.

in Figure 2.17. The illumination is provided by a SuperK EXTREME/FIANIUM supercontinuum white-light laser that is monochromated (1 nm bandwidth) by an Acousto-Optic Tunable Filter (AOTF) and subsequently coupled to a single-mode fiber. The output of the fiber is collimated by a condenser lens and passed through a spinning diffuser plate to evenly illuminate the image which is composed of Cr patterns on glass. The diffuser also serves to remove speckle artefacts in imaging that otherwise occur due to the large spatial coherence of the source. The image is projected at unity magnification onto the metasurface by two Olympus MPlanFL N 20x-0.45NA objectives. The second half of the setup is a standard microscope with Fourier imaging capabilities, already reported in Ref.[19]: the image is collected by either of two objectives (Nikon Plan Fluor 20× – 0.5 NA and Nikon S Plan Fluor ELWD 60× – 0.7 NA) and projected onto a Photometrics CoolSNAP EZ silicon CCD camera by a 20 cm focal distance tube lens. In between objective and tube lens, a 1:1 telescope provides an intermediate real space plane, while flipping in the Fourier (or Bertrand) lens allows projection of the back focal plane of the objective

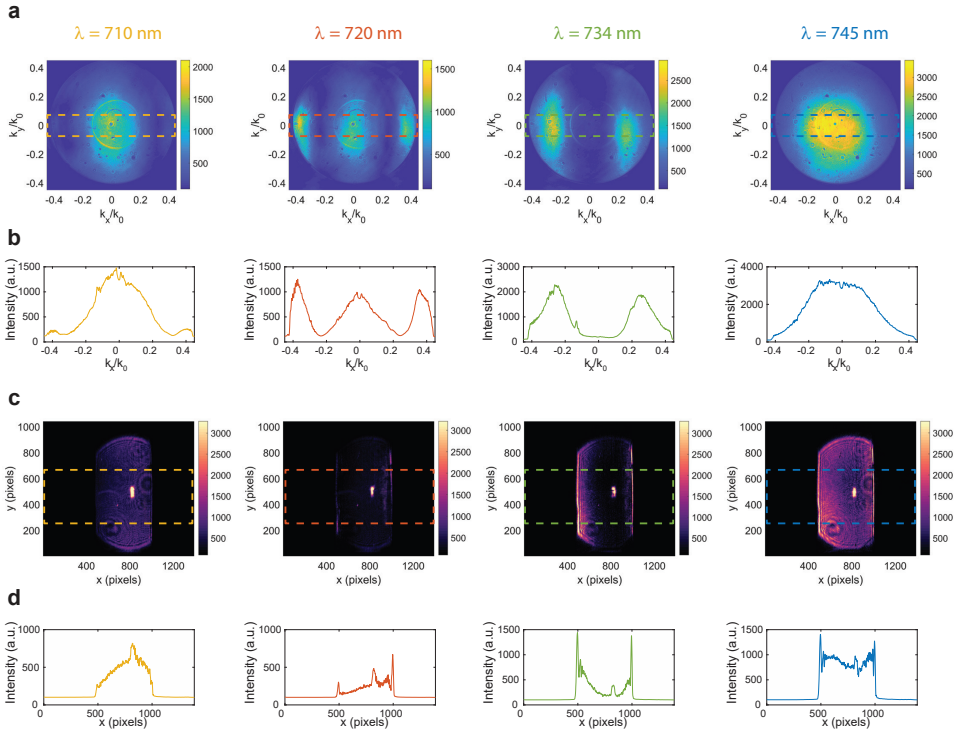

Figure 2.18: **a** Fourier space intensity map of light transmitted through the metasurface as the excitation wavelength is changed. **b** Average along the *y*–axis within the dashed box in a. **c** Image of the metasurface output as the excitation wavelength is changed. The input image is a slit. **d** Average along the *y*–axis within the dashed box in c.

directly onto the CCD [20] (Fourier imaging mode, unit magnification from back focal plane to objective).

This setup also allows transfer function amplitude measurements if the image and the first objective (from left) are removed and the Bertrand lens is flipped in. Indeed, using this configuration, light transmitted through the metasurface under a certain span of angles (dependent on the objectives' NA) is imaged in k-space and therefore the amplitude of the metasurface transfer function can also be obtained. However, compared to the simpler transmission setup described above, normalization of the intensity is more difficult and less reliable since it requires realignment and repositioning of the objectives. For this reason, while this technique is very insightful and gives information also for $k_y \neq 0$, it is still preferable to use the integrating sphere and a rotating stage to measure quantitatively the transfer function.

Figure 2.18a shows such not normalized transfer function amplitudes as the excitation wavelength is scanned across the resonance. The dark blue regions in these colormaps signal the spatial components that the metasurface is rejecting, either by absorption or

by reflection. As the wavelength is increased, the minima in k–space are moving closer to normal incidence ($\mathbf{k} = 0$): only on resonance it is possible to couple to the leaky mode from normal incidence, while for an off-resonant wavelength also an off-normal incident excitation is required, as expected from momentum matching. Furthermore, the transfer function is completely transforming in a narrow bandwidth going from a low–pass spatial filter ($\lambda = 710$ nm) to a high–pass spatial filter on resonance. At $\lambda = 745$ nm the metasurface is not imparting any modulation in k–space and the Gaussian profile of light out–coupling from the fiber and scattered evenly from the diffuser is retrieved.

These measurements clearly show the 1D nature of the metasurface operation. In fact, on resonance low k_x spatial components are suppressed also for a wide range of k_y. Hence, the 2$^{\text{nd}}$–order differentiation is experimentally performed in a line-by-line fashion, in agreement with the numerical calculation shown in Figure 2.9 of Chapter 2.

Flipping out the Bertrand lens and inserting the first objective and an image, it is possible to study the metasurface image processing corresponding to the transfer functions just discussed (see Figure 2.18c). In this case the image is a simple adjustable slit. At $\lambda = 710$ nm the metasurface is acting as a low–pass filter so the image of the slit is blurred and the edges are smoothed. On resonance the edges are clearly detected while off-resonance, for $\lambda = 745$ nm, the image of the slit is recovered. The bright spot in Figure 2.18c is an artefact due to spurious reflection at the interface between air and the sapphire substrate.

Finally, we experimentally investigate the 2$^{\text{nd}}$–derivative operation of the Si metasurface when more complex images are projected onto the sample. We first project the image of one of our institutions' logos onto the metasurface using off-resonant illumination ($\lambda = 750$ nm) and then image the metasurface output onto the CCD (Figure 2.19b); the contrast of the input object is clearly maintained. On the other hand, for resonant illumination at $\lambda = 726$ nm (Figure 2.19c) the edges are clearly resolved in the transformed image. As expected, no edge contrast is observed for features along the x-direction since the derivative operation is performed along the same direction.

To study the edge profile in a quantitative manner, Figure 2.19d (red curve) shows a line profile taken along the horizontal direction in the processed image (red dashed line in Figure 2.19c). These data are compared to the calculated output profile assuming an ideal parabolic transfer function (blue curve in Figure 2.19d). Overall the experimental and ideal response show very similar trends: the double-peaked structure expected for 2$^{\text{nd}}$–order differentiation is clearly resolved in all of the six edges shown in Figure 2.19d. The discrepancies between experimental and ideal response are also probably due to a minor misalignment of the sample inducing small asymmetries in the transfer function.

Finally, we demonstrate the use of a Si metasurface for the processing of a gray–tone image of the *Meisje met de parel* described in the previous section. An off-resonant transmission image through the metasurface is shown in Figure 2.19f; the fine features and the contrast in the original object are clearly reproduced in the image. In contrast, the image processed at the resonant wavelength $\lambda = 726$ nm clearly shows the vertical edges along the face contour. The contours are fading away as they become gradually aligned with the x-axis, as expected. This clearly demonstrates that the metasurface image processing concept can be applied to more complex images containing gradients in transmission.

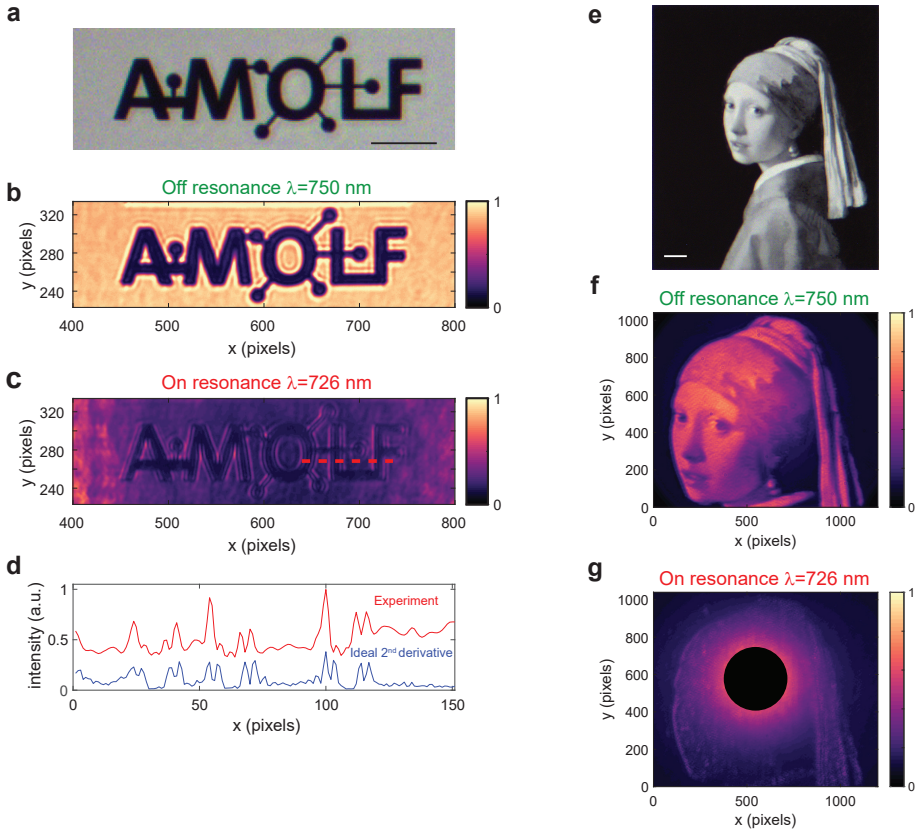

Figure 2.19: Experimental 2nd–order image differentiation. **a** Optical microscopy image of the input object; the scale bar is 20μm **b-c** Optical microscopy image of the metasurface output for resonant (λ = 726 nm) and off-resonant (λ = 750 nm) illumination. **d** Cross-cut through b (red line) averaged over 8 pixels along y, compared to ideal differentiation performed on the off-resonant image (blue line). **e** Optical microscopy image of the *Meisje met de parel* (J. Vermeer, circa 1665). The image is composed of micron-sized dots of Cr on glass. **f-g** Metasurface output for resonant and off-resonant excitation. The black spot in g covers an artefact due to spurious reflection at the interface between air and the sapphire substrate.

2.7. 2D OPERATIONS AND UNPOLARIZED ILLUMINATION

The metasurface designs presented above are limited to 1D operation and work for light of a specific polarization. While this is an insightful proof–of–concept, designs that can perform 2D mathematical operations on impinging images independently of the polarization are essential for practical implementations. It is possible to achieve this by exploiting highly rotationally symmetric lattices: the designs are based on a triangular lattice of air holes carved into a suspended silicon membrane, which sustains a Fano resonance stemming from the coupling of a leaky-wave mode to a longitudinal Fabry-Pérot resonance, similar to the design concept explained above.

Extending the formalism used so far, consider a linearly polarized beam impinging on our metasurface, corresponding to an arbitrary 2D image, with a transverse field profile

$$\mathbf{E}^{\text{in}}_{x,y}(x,y) = \begin{pmatrix} E^{\text{in}}_x(x,y) \\ E^{\text{in}}_y(x,y) \end{pmatrix} \tag{2.11}$$

where the subscript x and y indicate the x- and y-polarized field components. Upon interaction with the metasurface, the input beam is filtered in momentum space (k-space) by the 2×2 transmission tensor S of the metasurface (i.e. transfer function)

$$\mathsf{S}_{21} = \begin{pmatrix} S_{ss}(k_x,k_y) & S_{sp}(k_x,k_y) \\ S_{ps}(k_x,k_y) & S_{pp}(k_x,k_y) \end{pmatrix} \tag{2.12}$$

where S_{uv} is the transmission coefficient from an input v-polarized wave to an output u-polarized one with transverse wavevector $\mathbf{k}_{/\!/} = k_x\hat{\mathbf{x}} + k_y\hat{\mathbf{y}}$.

The output signal is calculated as follows. The input signal is Fourier-transformed $\mathscr{F}[\mathbf{E}^{\text{in}}_{x,y}(x,y)]$ and converted into the sp-polarization basis via multiplication with the matrix

$$\mathsf{R} = \begin{pmatrix} \sin\phi & \cos\phi \\ -\cos\phi & \sin\phi \end{pmatrix} \tag{2.13}$$

where ϕ is the azimuthal angle between $\mathbf{k}_{/\!/}$ and the x-axis. This spectrum is filtered by the metasurface transfer function S and projected back onto the xy-polarization basis by multiplying it with R^{-1}. Finally, an inverse Fourier transform is performed to derive the spatial profile of the output field. These steps are captured in the following equation for the transmitted image $\mathbf{E}^{\text{out}}_{x,y}(x,y)$

$$\begin{pmatrix} E^{\text{out}}_x(x,y) \\ E^{\text{out}}_y(x,y) \end{pmatrix} = \mathscr{F}^{-1}\left[\mathsf{R}^{-1}\begin{pmatrix} S_{ss}(k_x,k_y) & S_{sp}(k_x,k_y) \\ S_{ps}(k_x,k_y) & S_{pp}(k_x,k_y) \end{pmatrix}\mathsf{R}\left(\mathscr{F}\left[\begin{pmatrix} E^{\text{in}}_x(x,y) \\ E^{\text{in}}_y(x,y) \end{pmatrix}\right]\right)\right] \tag{2.14}$$

Within this formalism, it is possible to calculate the response for unpolarized light assuming that the input field is constituted by both x- and y-components with the same intensity and random phases. Then, the average intensity of detected light is found by adding the intensities of the two orthogonal polarization components.

Ideally, the metasurface should have identical response to both polarizations, and have no polarization mixing in its response function. Thus the transfer function in Eq.(2.12) should be of the form $\mathsf{S}_{21} = S(k_x,k_y)\mathbb{I}_2$, where $S(k_x,k_y)$ is an arbitrary scalar function and $\mathbb{I}_2$ is the 2×2 identity matrix. Next, if the response is also azimuthally symmetric,

$S(k_x, k_y) = S(k_{\parallel})$, with $k_{\parallel} = (k_x^2 + k_y^2)^{1/2} = k_0 \sin\theta$ and θ is the incidence angle with respect to the normal direction to the metasurface.

Focusing on the case of differentiation, azimuthal symmetry is only possible for even–order operations, in which case $S_n(k_{\parallel}) = A_n(ik_{\parallel})^n$,where n is the differentiation order and A_n is a constant. For example, in the case of second-order differentiation, the response corresponding to the Laplace operator $\nabla^2 = \frac{\partial^2}{\partial x^2} + \frac{\partial^2}{\partial y^2}$ is[2]

$$\mathsf{S}_2(k_x, k_y) = \begin{pmatrix} A_2(k_x^2 + k_y^2) & 0 \\ 0 & A_2(k_x^2 + k_y^2) \end{pmatrix} = A_2(k_{\parallel})^2 \mathbb{I}_2 \tag{2.15}$$

Interestingly, azimuthal symmetry is not possible for odd-order differentiation. For this type of operations, $S(k_x, k_y)$ can be defined along a radial direction as $S_n(k_x, k_y) = A_n(\phi)(ik_{\parallel})^n$, where $A_n(\phi)$ is a function of the azimuthal angle. As an example, the first-order differentiation is described through

$$\mathsf{S}_1(k_x, k_y) = A_1(\phi)(ik_{\parallel})\mathbb{I}_2 \tag{2.16}$$

and involves a π phase jump with respect to $\theta = 0$ (normal incidence). As shown earlier, implementing such an operation requires metasurfaces breaking symmetries in both transverse and longitudinal directions.

Following the design principles explained in Section 2.3, it is possible to engineer the metasurfaces' response in transmission. Starting with the case of 2$^{\text{nd}}$-order differentiation, the metasurface consists of a triangular array of air holes (lattice constant a and radius r) carved in a thin Si membrane of thickness t (see Figure 2.20a). The high rotational symmetry of the lattice implies polarization insensitivity at normal incidence,[3] and a quasi-isotropic response in ϕ over the entire transverse momentum space.

The optimal metasurface parameters for second-order spatial differentiation at λ = 717 nm are a = 250 nm, r = 120 nm, and t = 125 nm. Figure 2.20b-c, shows the transmission amplitude for the co-polarized components of the transmission matrix. Cross-polarized transmission amplitudes are negligible (data shown in the Supporting Information of Ref. [22]). The design and simulations consider realistic material loss [23], which limits the maximum achievable transmission to ~ 0.7. Both amplitude and phase responses are symmetric in all transverse directions, as required for ideal even-order differential operation. Furthermore, the metasurface supports an angular bandwidth of 8° for both s- and p-polarized illuminations, hence, allowing efficient 2D edge detection with NA$\simeq$ 0.14. It is worth comparing this design to the photonic crystal slab Laplace operator proposed by Guo et al. [14, 15]. While their design achieves a more isotropic response, the NA of operation is almost one order of magnitude smaller than what is presented here. This has an impact on the resolution and on the applicability of the structure to standard imaging systems that have typically larger NA. On the other hand, a non-perfectly isotropic response does not hinder edge–detection. Indeed, in order to as-

[2] The one-dimensional proof in Section 2.1 can be readily generalized to two dimensions. Similarly, partial differentiation in real space $\frac{\partial f(x,y)}{\partial x}$ corresponds to $ik_x F(k_x, k_y)$ in k-space. Other differential operators can be constructed in the same way (e.g. $\left(\frac{\partial^2}{\partial x^2} + \frac{\partial^2}{\partial y^2}\right) f(x,y) \rightarrow -(k_x^2 + k_y^2)F(k_x, k_y)$) [21].

[3] Any in-plane polarization vector can be written as a linear combination of two basis vectors that span the entire plane and for which the response is the same by symmetry (the same consideration applies in Chapter 5).

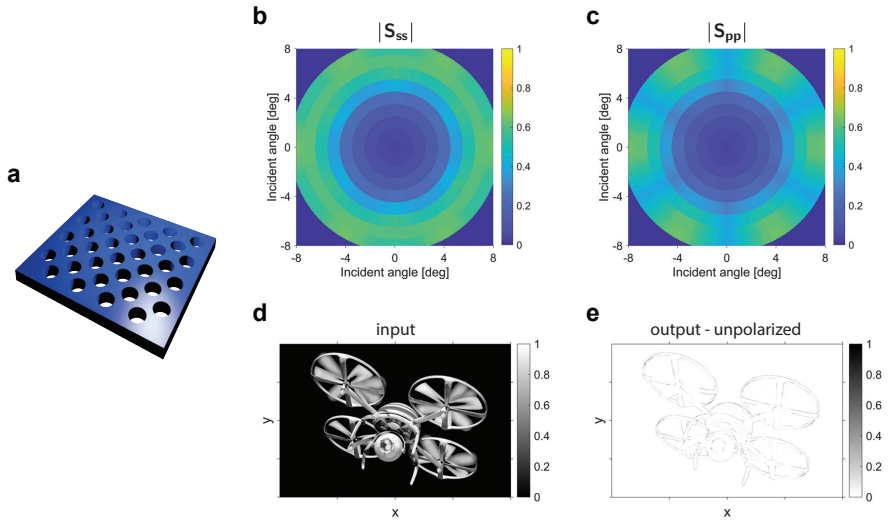

Figure 2.20: **a** 3D rendering of the proposed metasurface performing 2nd-order differentiation: a triangular array of air holes (lattice constant a and radius r) carved in a thin Si membrane of thickness t. **b-c** Transmission amplitude of co-polarized fields for the optimal design including Si losses. **d** 2D input image used to test the metasurface's edge detection functionality. **e** Metasurface output for the unpolarized input image in panel d.

sess the functionality of the metasurface, the 2D input image in Figure 2.20d is projected onto the metasurface and the output is calculated through Eq.(2.14). The metasurface detects edges in all transverse directions with high efficiency for unpolarized illumination, as shown in Figure 2.20e. Overall, the metasurface response is very close to the the ideal output from a second order (Laplacian) operation (data shown in Ref. [22]).

In order to implement odd-order differentiation, the transmission phase needs to be an odd function of the incidence angle θ, which requires breaking both transverse and longitudinal symmetries in the metasurface. To this end, our unit cell is modified as shown Figure 2.21a, adding a thin SiO_2 substrate to break longitudinal symmetry (the symmetry parallel to the z-axis) and three small holes symmetrically distributed around the main hole to break transverse symmetry (the symmetry on the xy-plane). The transmission amplitude and phase for co-polarized fields is shown in Figure 2.21b-c. The metasurface exhibits an odd-order response along any radial direction, but it lacks rotational symmetry as in even-order differentiation. The metasurface achieves a near-π phase jump between the negative and positive transverse propagation momentum, which enables first-order differential operation at $\lambda = 628$ nm. Cross-polarized transmission is again negligible (data shown in the Supporting Information of Ref. [22]) and the metasurface performs differentiation with a NA$\simeq 0.21$ and $\simeq 0.14$ for s- and p-polarizations, respectively. The metasurface design parameters are $a = 300$ nm, $r = 130$ nm, $r_1 = 77$ nm, $t_{sub} = 50$ nm, $t_{etch} = 90$ nm, and the material is assumed lossless in this calculation, considering only the real part of the Si dispersive refractive index.

Again, it is important to explore the effect of the first-order differentiator metasurface

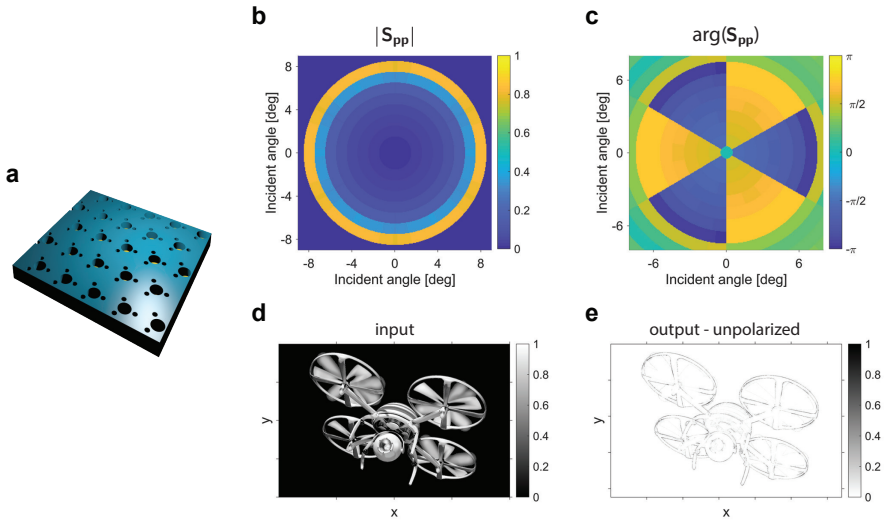

Figure 2.21: **a** 3D rendering of the proposed metasurface performing 1st-order differentiation. Extra air holes are added to the thin Si membrane design performing the Laplacian operator along with a SiO_2 thin layer. **b-c** Transmission amplitude (b) and phase (c) for co-polarized fields for the optimal design. **d** 2D input image used to test the metasurface's edge detection functionality. **e** Metasurface output for the unpolarized input image in panel d.

on the 2D input image in Figure 2.21d for different polarizations. The metasurface output demonstrates clear edge detection in all directions, highlighting all boundaries of the object for unpolarized illumination, even with a small difference of NA between s- and p-polarizations. Differences on 2D edge detection between the first- and the second-order differentiators are compared and provided in Ref. [22], showing that the first-order differentiator gives one peak per edge while the second-order counterpart results in a doubly–peaked structure as the one in Figure 2.19.

Even in the presence of some nonidealities, such as non perfectly isotropic response and polarization-dependent NA, the proposed designs can be realistically fabricated and reliably perform isotropic 2D optical image processing regardless of the illumination's polarization.

2.8. CONCLUSION

To conclude, this chapter introduces how dielectric metasurfaces sustaining Fano resonances with suitably engineered dispersion can perform mathematical operations on arbitrary 2D input signals, with immediate applications in image processing and edge detection.

First, the Fourier optics concepts needed throughout the chapter are briefly reviewed and explained. Next, the idea of using a metasurface sustaining a Fano resonance is elaborated along with the rationale used to design its angle-dependent transmission by tuning a few structural parameters. Moreover, the necessity of breaking the structure's

symmetry to engineer odd-order differentiation is elucidated. Using these insights, the ideal amplitude and phase transfer functions can be approximated over a relatively wide k-space range spanning a numerical aperture up to 0.35 and that transmission over 0.8 can be achieved for large angles. The optimized designs are numerically tested on input images and functions, demonstrating strong consistency with 1^{st}- and 2^{nd}-order differentiation.

The optimal design for 2^{nd}-order differentiation is realized and the fabrication steps are discussed in detail. The finalized sample is characterized and its transfer function is measured. Finally, the metasurface image processing capabilities are experimentally demonstrated. We show clear edge detection at the resonant illumination $\lambda = 726$ nm as a result of the second-order spatial differentiation, both on high contrast and gray-scale projected images.

The last section extends these concepts to 2D operations and unpolarized illumination, enabling reliable detection of edges regardless of their orientation. Furthermore, it is worth mentioning that image processing metasurfaces were designed also in the microwave wavelength range using similar concepts yet exploiting different resonances [24].

Altogether, the results shown in this chapter can lead to a wide range of applications and can readily be implemented by directly placing the metasurface onto a standard CCD or CMOS detector chip, opening new opportunities in hybrid optical and electronic computing that operates at low cost, low power, and small dimensions.

REFERENCES

[1] B. E. A. Saleh and M. C. Teich, *Fundamentals of Photonics*, Wiley Series in Pure and Applied Optics (Wiley, 2007).

[2] J. W. Goodman, *Introduction to Fourier Optics*, 4th ed. (W. H. Freeman, 2017).

[3] S. Fan and J. D. Joannopoulos, *Analysis of guided resonances in photonic crystal slabs,* Physical Review B **65**, 235112 (2002).

[4] G. Pitruzzello and T. F. Krauss, *Photonic crystal resonances for sensing and imaging,* Journal of Optics **20**, 073004 (2018).

[5] S. S. Wang and R. Magnusson, *Theory and applications of guided-mode resonance filters,* Applied Optics **32**, 2606 (1993).

[6] S. S. Wang, M. G. Moharam, R. Magnusson, and J. S. Bagby, *Guided-mode resonances in planar dielectric-layer diffraction gratings,* Journal of the Optical Society of America A **7**, 1470 (1990).

[7] B. Luk'yanchuk, N. I. Zheludev, S. A. Maier, N. J. Halas, P. Nordlander, H. Giessen, and C. T. Chong, *The Fano resonance in plasmonic nanostructures and metamaterials,* Nature Materials **9**, 707 (2010).

[8] A. E. Miroshnichenko, S. Flach, and Y. S. Kivshar, *Fano resonances in nanoscale structures,* Reviews of Modern Physics **82**, 2257 (2010).

[9] L. Andreani and M. Agio, *Photonic bands and gap maps in a photonic crystal slab,* IEEE Journal of Quantum Electronics **38**, 891 (2002).

[10] U. Fano, *Sullo spettro di assorbimento dei gas nobili presso il limite dello spettro d'arco,* Il Nuovo Cimento **12**, 154 (1935).

[11] S. Fan, W. Suh, and J. D. Joannopoulos, *Temporal coupled-mode theory for the fano resonance in optical resonators,* Journal of the Optical Society of America. A **20**, 569 (2003).

[12] H. A. Haus, *Waves and fields in optoelectronics* (Prentice-Hall, Englewood Cliffs, N.J, 1984) p. 402.

[13] D. L. Brundrett, E. N. Glytsis, and T. K. Gaylord, *Homogeneous layer models for high-spatial-frequency dielectric surface-relief gratings: conical diffraction and antireflection designs,* Applied Optics **33**, 2695 (1994).

[14] C. Guo, M. Xiao, M. Minkov, Y. Shi, and S. Fan, *Isotropic wavevector domain image filters by a photonic crystal slab device,* Journal of the Optical Society of America A **35**, 1685 (2018).

[15] C. Guo, M. Xiao, M. Minkov, Y. Shi, and S. Fan, *Photonic crystal slab Laplace operator for image differentiation,* Optica **5**, 251 (2018).

[16] T. Zhu, Y. Zhou, Y. Lou, H. Ye, M. Qiu, Z. Ruan, and S. Fan, *Plasmonic computing of spatial differentiation,* Nature Communications **8**, 15391 (2017).

[17] M. A. Green, *Self-consistent optical parameters of intrinsic silicon at 300K including temperature coefficients,* Solar Energy Materials and Solar Cells **92**, 1305 (2008).

[18] I. H. Malitson and M. J. Dodge, *Refractive Index and Birefringence of Synthetic Sapphire,* in *Program of the 1972 Annual Meeting of the Optical Society of America*, Vol. 62 (1972) p. 1336.

[19] I. Sersic, C. Tuambilangana, and A. Femius Koenderink, *Fourier microscopy of single plasmonic scatterers,* New Journal of Physics **13**, 083019 (2011).

[20] J. A. Kurvits, M. Jiang, and R. Zia, *Comparative analysis of imaging configurations and objectives for Fourier microscopy,* Journal of the Optical Society of America A **32**, 2082 (2015).

[21] R. N. Bracewell, *Relatives of the fourier transform,* in *The Fourier transform and its applications* (McGraw-Hill New York, 1986) pp. 329–335.

[22] H. Kwon, A. Cordaro, D. Sounas, A. Polman, and A. Alù, *Dual-polarization analog 2D image processing with nonlocal metasurfaces,* ACS Photonics **7**, 1799 (2020).

[23] E. D. Palik, *Handbook of Optical Constants of Solids* (Academic Press, Boston, 1998).

[24] H. Kwon, D. Sounas, A. Cordaro, A. Polman, and A. Alù, *Nonlocal Metasurfaces for Optical Signal Processing,* Physical Review Letters **121**, 173004 (2018).

3

SWITCHABLE DIFFERENTIATION

This chapter extends the concept of all-optical processing via metasurfaces to the world of devices to achieve real-time control of the mathematical operation imparted on an input projected image. To do so, a metasurface sustaining a Fano resonance similar to those described Chapter 2 is combined with an electrically gated WS_2 monolayer.

The first section provides a brief introduction to excitonic resonances in quasi–2D transition metal dichalcogenides materials. The strong effect caused by carrier injection on the optical properties of the layer can be leveraged to actively tune the metasurface transfer function. Next, an optimized design for switchable edge detection is presented and numerically tested demonstrating reliable on-demand high-pass filtering. In Section 3.3, nanofabrication of the designed structure is presented step-by-step. Finally, the fabricated sample is tested both optically and electrically showing small yet promising reflectance modulation as a function of the external bias applied, showing the potential of switchable all-optical edge detection using a hybrid metasurface–2D-TMD platform.

THE possibility of shaping the wavefront of optical fields in k-space via thin metasurfaces opens new avenues for analog signal processing, as discussed in depth within Chapter 2.

Despite the tremendous recent advances and growing attention to this research field, the functionality of metasurfaces designed for analog computing remains static. Nonetheless, in many emerging applications (e.g. artificial intelligence, machine learning, computer vision, etc.), tunable or switchable devices performing mathematical operations in an analog fashion on impinging signals are highly desirable.

Actively controlling a metasurface's functionality essentially requires the possibility of distorting its geometry and/or manipulating the refractive index of one of its constituting materials [1–6]. Among a plethora of interesting solutions, Transition Metal Dichalcogenide (TMD or TMDC) monolayers are acquiring a central role in the emerging field of tunable metamaterials [7, 8]. Indeed, these materials can achieve large changes in their refractive index in the visible spectral range [9, 10], high switching speed, and are compatible with Complementary Metal-Oxide-Semiconductor (CMOS) circuits.

The work presented in this Chapter analyzes whether the tunability of monolayer TMDs can be combined with metasurfaces featuring a designer response in k-space to realize a device whose image processing capabilities can be controlled electrically. Specifically, the excitonic optical response of WS_2 is used to modify the transfer function (i.e. angle-dependent reflection) of a high-index grating sustaining a quasi-guided mode along its surface. In turn, the possibility to electrically suppress the excitonic oscillator strength is leveraged to actively modulate the reflection.

3.1. EXCITONIC EFFECTS IN 2-DIMENSIONAL TMDCS

Excitons are excited states of a crystal consisting of an electron and associated hole attracted to each other by Coulomb forces. It is possible to distinguish between two basic types of excitons: *Frenkel* excitons (or small–radius excitons) that are tightly bound within the same or nearest–neighbor unit cell and *Wannier–Mott* excitons (or large–radius excitons) that extend over many lattice constants. In the latter case, the exciton behaves like a quasi–particle that can freely move inside the crystal. In the following, only Wannier–Mott excitons are discussed as these are dominant for most semiconductors and few-layers TMDs.

The exciton motion can be conveniently decomposed into a center–of–mass (CM) motion and a relative motion of the electron and hole about the CM. The exciton CM can be thought of as free particle of mass $M = m_e + m_h$ (where m_e and m_h are the electron and hole effective masses respectively) and wavevector K, thus having a kinetic energy

$$E_{ke} = \frac{\hbar^2 K^2}{2M}. \tag{3.1}$$

The relative motion, on the other hand, is governed by the Coulomb potential energy

$$U(r) = -\frac{e^2}{4\pi\epsilon_0 \epsilon\, r}, \tag{3.2}$$

where r is the electron–hole distance and ϵ is the crystal dielectric constant and, in a first approximation, is analogous to that of an electron and a proton in the Bohr model of the

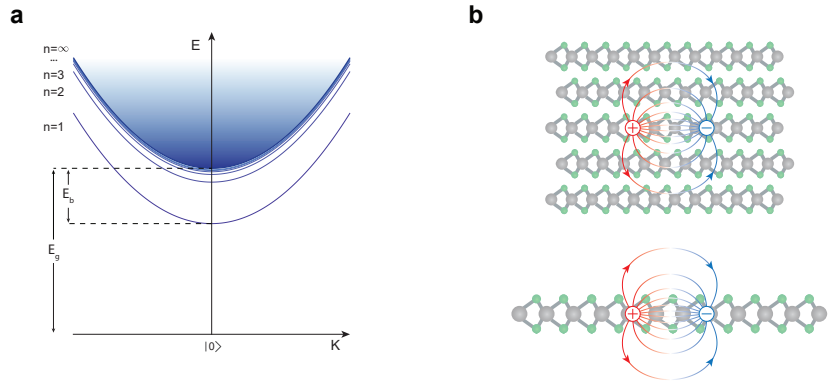

Figure 3.1: **a** Wannier–Mott exciton dispersion relation. The bound stated are indicated by blue solid lines while the shaded light-blue area corresponds to the continuum states. The electronic ground state (with no excitons and fully occupied valence band) is chosen as zero energy. **b** Schematic representation of excitons in bulk and monolayer TMDCs.

hydrogen atom. Similarly, there are quantized bound states labeled with the principal quantum number n and continuum states in which the excitons are ionized into free electrons and free holes. Hence, the total exciton energy is

$$E_{ex} = E_g + \frac{\hbar^2 K^2}{2M} - \frac{E_b}{n^2}. \tag{3.3}$$

where E_g is the bandgap and E_b is the exciton binding energy corresponding to the ground state $n = 1$ (see Fig. 3.1a). The high dielectric constant of typical semiconductors implies a low binding energy (e.g. 4.2 meV for GaAs and 14.7 meV for Si). In fact, the exciton can be stable and exist only if the attractive Coulomb in Eq.(3.2) is strong enough to prevent the exciton from ionization due to collisions with phonons, namely E_b has to be greater than $k_b T$ (where k_b is the Boltzmann constant and T is the temperature). Hence, excitons in most semiconductors are present only at cryogenic temperatures as $k_b T \sim 25$ meV at room temperature.

In this context, layered materials called Transition Metal Dichalcogenides (TMDs or TMDCs) have recently attracted great attention [11, 12], given their unique excitonic properties. These are of the chemical form MX_2 where M is a transition metal (e.g. Mo, W, etc.) and X is a chalcogen (e.g. Se, S, etc.). The typical structure of each layer consists of a triangular lattice of transition metal atoms sandwiched between two triangular lattices of chalcogen atoms. Strong covalent bonds hold each layer together while weak van der Waals forces govern inter-layer bonding. This latter weak interaction allows the isolation of single monolayers via simple micromechanical cleavage [13, 14]. Interestingly, the electronic and optical properties of these quasi-two-dimensional TMDs differ dramatically from those of their bulk counterparts; for example, MoS_2 and WS_2 are indirect–gap semiconductors in their bulk state but transition to direct–gap semiconductors in the monolayer limit [15, 16]. Furthermore, excitons in monolayer TMDs are strongly confined and experience reduced screening due to the change in the dielectric environment.

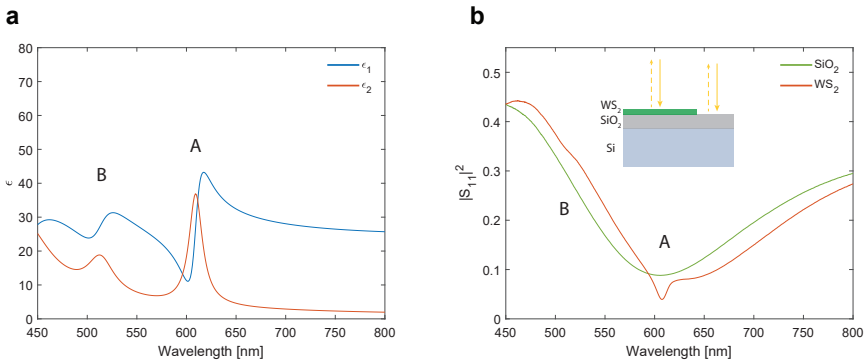

Figure 3.2: **a** Dielectric function ϵ of an MBE–grown WS_2 monolayer experimentally obtained via spectroscopic ellipsometry. **b** Measured reflectance spectra of an MBE–grown WS_2 monolayer on a SiO_2/Si substrate (SiO_2 thickness ~ 310 nm) and of the bare SiO_2/Si substrate.

Intuitively, in the monolayer limit, most of the electric field lines connecting electron and hole lie in a medium with a lower dielectric constant resulting in a higher Coulomb attraction (see Fig. 3.1b). For these reasons, typical binding energies are in the range of 0.5 eV (0.32 eV for WS_2 [17]) and excitons are stable also at room temperature.

The presence of stable excitons dominates the optical properties of monolayer TMDs. Figure 3.2a shows the dielectric function ϵ of a WS_2 monolayer measured via spectroscopic ellipsometry. The peaks in the imaginary part of the dielectric function ϵ_2, and the corresponding (via Kramers–Kronig relations) anomalous dispersion in the real part ϵ_1, indicate light's resonant coupling to the exciton ground state ($n = 1$)[1] and can be modeled by a set of Lorentzian oscillators [21, 22]. Specifically, it is possible to distinguish two different exciton peaks, labeled A and B in Fig. 3.2a, corresponding to two different direct–gap transitions as the valence band is split at the K point of the Brillouin zone due to spin-orbit coupling [15, 16, 23].

The exciton resonance effects in the dielectric function readily translate into the Fresnel coefficients of the monolayer and thus on its reflectance. As shown in Fig. 3.2b, the Fabry-Pérot reflectance[2] spectrum of a thin (~ 310 nm) silica layer on a Si substrate changes as a WS_2 monolayer is added on top, with two features appearing at the wavelengths corresponding to the A and B exciton resonances.

An alternative but equally insightful way of understanding how light interacts with excitons is to model them as a collection of oscillating dipoles that can re-radiate part of the absorbed light [24, 25].

The description so far concerns the interaction of excitons with light. Nonetheless, excitons in TMDs can also be manipulated from an electronic perspective via gating. To do so, the monolayer is integrated in a standard MOS (Metal-Oxide-Semiconductor) capacitor [28, 29], as schematically illustrated in Fig. 3.3a. Figure 3.3b shows the calculated

[1] A detailed and rigorous quantum derivation of ϵ_2 starting from the exciton energies in Eq.(3.3) and corresponding wavefunctions employing Fermi's Golden Rule can be found in Refs. [18–20].

[2] Following the s-matrix formalism, here the reflectance is labeled $|S_{11}|^2$ while S_{11} will be referred to as reflection (see Appendix A).

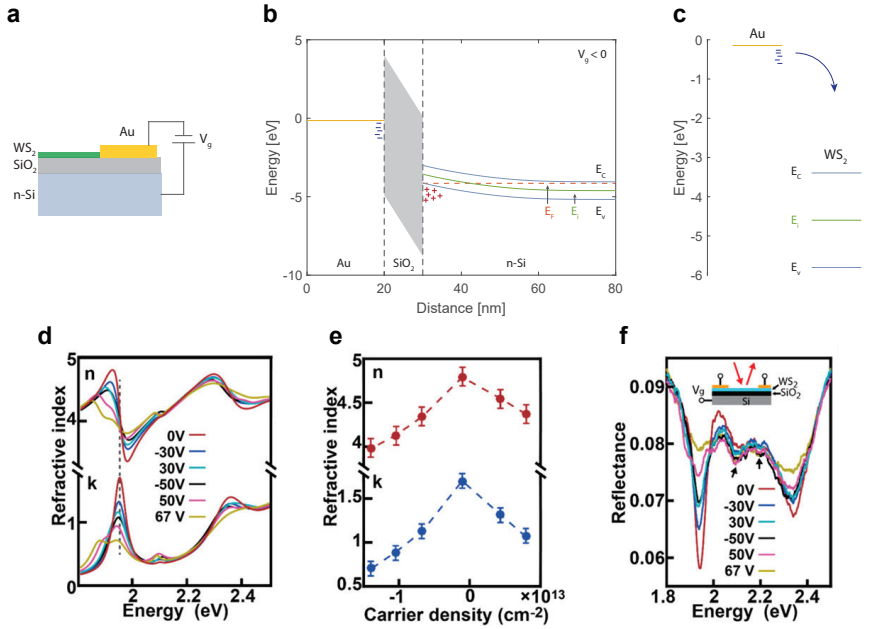

Figure 3.3: **a** Schematic of the device. The carrier density in WS_2 is tuned by applying a voltage V_g between the Au electrode and the n-type Si substrate. **b** Calculated [26] energy band diagram of an MOS capacitor made of Au (work–function 5.1 eV), SiO_2 (20 nm), and n-type Si (dopant concentration $\sim 10^{18}$ cm^{-3}). For the sake of simplicity, this calculation does not take into account the WS_2 monolayer. **c** Calculated Fermi level of Au from panel b and energy bands of WS_2 [14]. **d** Fitted refractive index (real part n and imaginary part k) for different gating voltages. **e** Peak value of the real part (at 1.92 eV) and the imaginary part (at 1.95 eV) of the refractive index as a function of carrier density. **f** Reflectance spectra of monolayer WS_2 at different gating voltages. The inset is a schematic illustration of the sample structure and the measurement configuration. Panels d-f are reproduced from Ref. [27].

band diagram [26] for such a capacitor consisting of Au, SiO_2 and n-doped Si when a negative gate bias $V_g = -4$ V is applied. Close to the SiO_2 surface, the Fermi level E_f on the Si side is below the intrinsic value E_i and close to the valence band implying a great buildup of holes (inversion regime). This, in turn, induces an electron accumulation on the Au side at the interface with SiO_2, like in a standard parallel-plate capacitor. Next, it is possible to compare the Au Fermi level at this bias condition to the energy bands of WS_2 [14]. The Schottky barrier height (the energy required for injection from the metal into the monolayer TMD) at zero bias for this specific materials combination is less than 1 eV. Thus, at the calculated bias, electrons can transfer to WS_2 (see Fig. 3.3c). This illustrative and simplified picture neglects defect states at the interface between TMDs and metal [30].

Excitons in monolayer TMDs are sensitive to the presence of injected carriers mostly due to Coulomb scattering and screening effects [27, 31]. Specifically, screening dampens the electric fields between electrons and holes due to the presence of mobile charge

carriers and results in a small change (~ 30 meV in WS_2 [27]) in the binding energy. On the other hand, the interaction of excitons with injected carriers via Coulomb scattering leads to the conversion of neutral A excitons to negatively ($A + e^- \rightarrow A_-$) or positively ($A + h^+ \rightarrow A_+$) charged trions that have a different binding energy. Furthermore, these scattering events decrease the lifetime of the exciton inducing a broadening of the resonance linewidth. These effects have a direct impact on the optical properties of the layer. Figure 3.3d-e (from Ref. [27]) highlights the dependence of the refractive index's real and imaginary parts on the applied bias voltage and hence on the injected carrier concentration. Looking at the imaginary part, the spectral width of the exciton resonance broadens and a shoulder related to trions appears at lower energies as the gate voltage increases. This change in the refractive index has an immediate impact on the measured reflectance of the layer (see Fig. 3.3f from Ref. [27]) and the dip related to the A exciton mostly disappears. Such large changes in the material's optical properties as a function of external signals are unprecedented, and therefore form a unique platform for actively-tunable metasurfaces.

In this section, the concept of an exciton and its importance in monolayer TMDs have been elucidated. Excitonic resonances have a big impact on the optical properties and, at the same time, can be manipulated electronically in a CMOS compatible configuration via an applied bias. Hence, gating is ultimately an efficient tuning knob of the optical properties in monolayer TMDs.

3.2. DESIGN

In this chapter, the possibility of combining a gated WS_2 monolayer with a high-index grating is explored (see Fig. 3.4a). Indeed, such a combination may benefit from the tunability of monolayer TMDs under an applied bias but also from the design flexibility, given by a high-index metasurface, in tailoring the transfer function. Hence, such a meta-device would act as a switchable Fourier spatial filter. As schematically depicted in Fig. 3.4a, a TiO_x grating is applied to the MOS configuration described in the previous section. An aluminum oxide layer is used to encapsulate the WS_2 monolayer as well as an etch–stop layer.

In order to simulate the device via FDTD, the refractive indices of TiO_x, AlO_x (as deposited in our lab) and WS_2 are experimentally measured using spectroscopic ellipsometry while those of Si and SiO_2 are taken from literature [32, 33]. Concerning WS_2, the behavior for different gating conditions is included in its optical properties. To do so, the refractive index is measured under no bias via ellipsometry by fitting the dielectric function with a set of Lorentzian oscillators (solid lines in Fig. 3.4b). Next, to give an estimate of optical properties under bias, the Lorentzian oscillator concerning the A-exciton is removed and the dielectric function is plotted again without re-fitting the data. The resulting refractive index is also plotted in Fig. 3.4b (dashed lines) and corresponds to the complete quenching of the excitonic response in the material. This approximation can be relaxed by multiplying the A-exciton Lorentzian by a factor that can be estimated *a posteriori* experimentally.

Using these refractive indices, it is possible to design the device's optical response in its ON (i.e. no gate voltage applied) and OFF (i.e. no A-exciton) states. Starting from the OFF state, the metasurface is engineered to sustain a Fano resonance [34–36] in reflection given by the interference of a broad Fabry-Pérot background, determined by the thicknesses of the layer stack and grating fill factor, and sharp quasi-guided modes (or Guided Mode Resonances - GMRs) that can be launched along the surface [37–40]. Figure 3.4c shows the simulated reflection S_{11} spectrum of an array of titania nanobeams (width w = 240 nm, height h = 96 nm, pitch p = 470 nm, AlO_x layer thickness t_{AlOx} = 11 nm, SiO_2 layer thickness t_{SiO2} = 299 nm) when illuminated by light polarized along the nanobeams' direction. Due to the Fano interference, the reflection swings from close to zero ($\lambda \sim 620$ nm) to ~ 0.8 across a narrow spectral range.

When the A-exciton is included (ON state), another Fano asymmetric lineshape appears around $\lambda \sim 610$ nm due to the interference of the excitonic resonance with the just described Fabry-Pérot background and GMR. It is worth remarking that, while the latter two resonances are of "geometrical nature"(i.e. exist and are related to the way the materials are nanostructured), the excitonic resonance is characteristic of the material. By carefully designing the metasurface, it is possible to balance out these three contributions to obtain a shifted minimum ($\lambda \sim 626$ nm) in the ON state, as shown in Fig. 3.4c.

The wavelength of the minima for the ON and OFF state, $\lambda \sim 626$ nm and $\lambda \sim 620$ nm respectively, define the two possible wavelengths of operation for the device. Next, the related transfer functions $S_{11}(k_x)$ are calculated by simulating the reflection as a function of the angle of incidence. As described in Section 2.3, the shape of the transfer function can be tuned by designing the dispersion of the quasi-guided mode resonance, as well as the Fano line-shape asymmetry and linewidth.

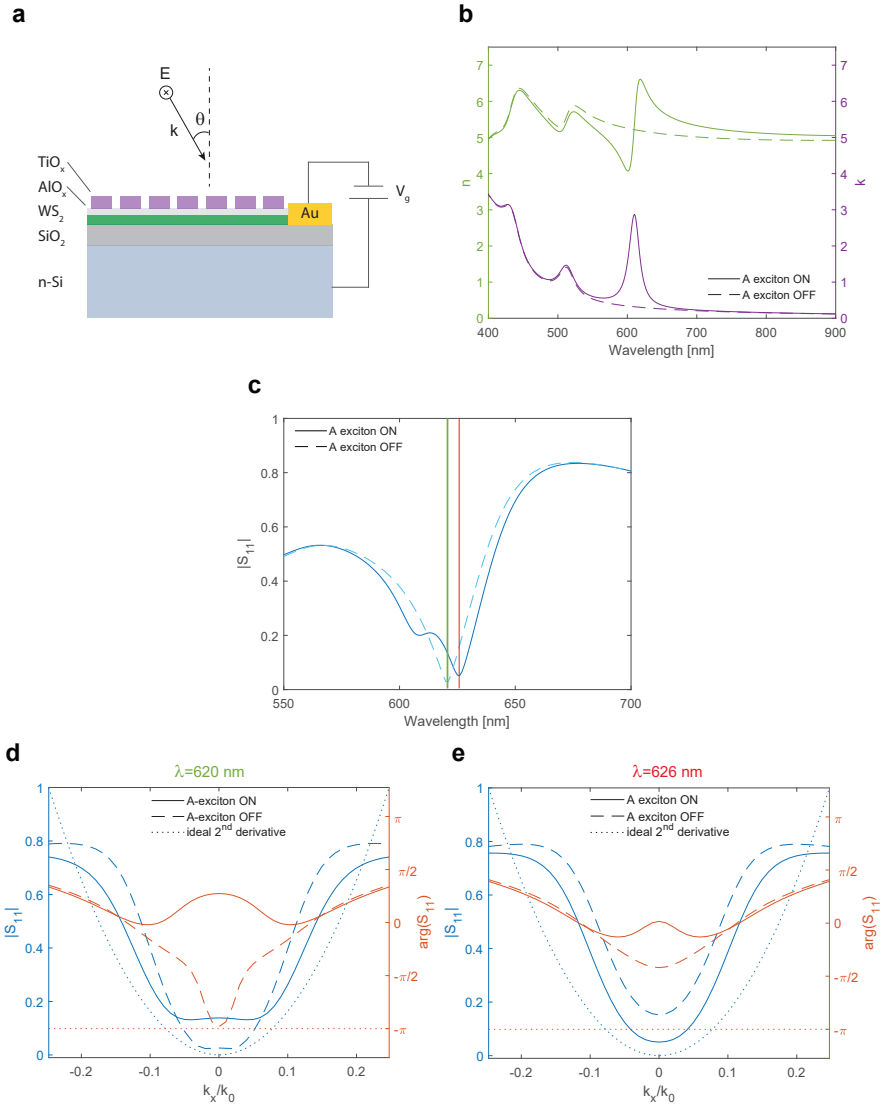

Figure 3.4: **a** Schematic of the meta-device combining a gated WS_2 monolayer in a MOS configuration with a TiO_x metasurface. **b** Refractive index (real part n and imaginary part k) of a CVD–grown WS_2 monolayer experimentally obtained via spectroscopic ellipsometry. The solid lines represent the situation where no bias is applied (A-exciton ON) while the dashed lines correspond to complete annihilation of the A-exciton. **c** Simulated reflection spectrum of the meta-device in panel a (width $w = 240$ nm, height $h = 96$ nm, pitch $p = 470$ nm, AlO_x layer thickness $t_{AlOx} = 11$ nm, SiO_2 layer thickness $t_{SiO2} = 299$ nm) for the OFF state (dashed line) and ON state (solid line). The red ($\lambda = 626$ nm) and green ($\lambda = 620$ nm) vertical solid lines indicate the two possible wavelengths of operation. **d** Simulated transfer functions of the device in panel a. Reflection amplitude $|S_{11}|$ (blue lines) and phase $\arg(S_{11}(k_x))$ (orange lines) for the ON (solid lines) and OFF (dashed lines) states at $\lambda = 620$ nm. The simulated transfer function is compared to the ideal 2^{nd}–order differentiation case (dotted lines). **e** Same as panel d, but at the illumination wavelength $\lambda = 626$ nm.

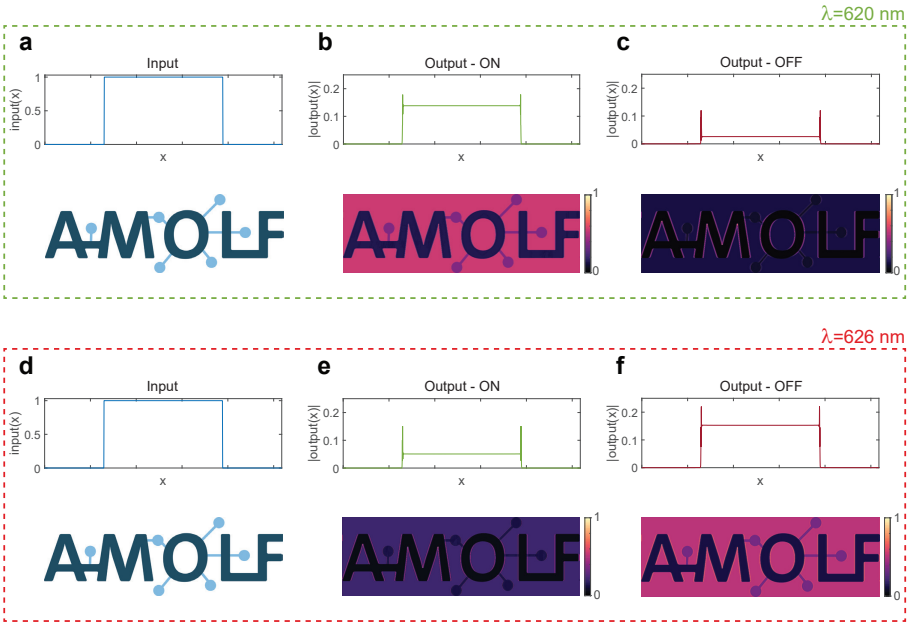

Figure 3.5: **a, d** Rectangular input functions and 2D image that are used to numerically test the metasurface operation. **b-c** Output for the input in panel a when the device is its ON (panel b) or OFF (panel c) state for $\lambda = 620$ nm. For the 2D image, differentiation is performed line by line along the x-axis. **d-f** Same as a-c, but for the illumination wavelength $\lambda = 626$ nm.

Figure 3.4d shows the simulated reflection amplitude $|S_{11}|$ and phase $\arg(S_{11})$ as a function of the in-plane wave vector k_x, normalized by the free space wavevector k_0 at the wavelength $\lambda = 620$ nm for the ON and OFF state. In the latter case (dashed lines in Fig. 3.4d), the metasurface strongly reflects light impinging at high angles of incidence while reflection at normal incidence is almost completely suppressed and amounts to ~ 0.02. Hence, the device acts as a high–pass Fourier spatial filter if an image is projected onto it. Furthermore, the angular response is close in amplitude to the ideal parabolic shape corresponding to 2^{nd}–order differentiation. The phase, however, shows a variation of more than π across the simulated angular range.

On the other hand, when the excitonic resonance is present (solid lines in Fig. 3.4d), $|S_{11}|(k_x)$ is flat around normal incidence and its value is higher compared to its OFF state counterpart in the same angular range. This difference implies that low spatial frequencies are no longer completely rejected, yet reflected with lower efficiency. Moreover, it is worth noticing that the NA of the device broadens slightly. It is interesting to point out that the phase response changes by more than π between ON and OFF states at low k_x values. This modulation in phase lag could be used in other nanophotonic applications even though the amplitude is relatively low.

The situation just described is reversed when the illumination wavelength is $\lambda =$

626 nm. As shown in Fig. 3.4e, low-frequency spatial components are more effectively canceled if the device is in its ON state. Also, the shape of the transfer function remains parabolic for both bias conditions.

Overall, the device is essentially designed as a high-pass filter that is perturbed by the absence ($\lambda = 626$ nm) or presence ($\lambda = 620$ nm) of the A-exciton resonance.

Finally, the transfer functions are numerically tested to assess the device's image processing capabilities in its ON and OFF state for both wavelengths of operation. To this end, the rectangular pulse input function in Fig. 3.5a is discretized into 2048 pixels[3], its Fourier transform is multiplied by the transfer function and eventually inverse Fourier transformed. In addition, it is possible to test arbitrary 2D images performing the same procedure line by line.

Figure 3.5b-c shows the calculated response at $\lambda = 620$ nm. In the ON state, the rectangular pulse amplitude is reduced and its edges are slightly enhanced. Indeed, while high spatial frequencies are more efficiently reflected, low frequencies are still present and contribute to the spatial content. Similarly, for our institution logo, the background is reduced but not completely canceled. In the OFF state, conversely, slowly varying features (corresponding to low spatial k-vector components) are almost completely suppressed while edges (composed of high-frequency spatial components) are enhanced both for the logo and the rectangular pulse. Given the 1D nature of the metasurface, differentiation is performed only along the x-axis, hence the edges along the same direction are not detected.

As anticipated, at $\lambda = 626$ nm the image processing behavior of the device is opposite and edge detection is more efficient when the exciton is present. Nonetheless, the residual reflection at normal incidence in the ON state is marginally higher compared to the OFF state at $\lambda = 620$. Hence, edge filtering is less ideal and the logo background in Fig. 3.5e is more visible compared to Fig. 3.5c.

To conclude, this section demonstrates a design of a meta-device capable of performing switchable optical signal processing by combining a gated TMD monolayer with a high–index grating sustaining a Fano resonance. The metasurface design shown is composed of nanostructures that can be realistically fabricated and experimentally tested, as shown in the next sections.

[3] See Section 2.4 on how to choose the pixel size such that the Nyquist range matches the operational NA of the metasurface.

3.3. FABRICATION

In this section, we outline the steps needed to fabricate the switchable image processing device described above. Figure 3.4 shows a brief graphical summary of the procedure. The term chip will be used to refer to the entire sample as it contains several individual devices.

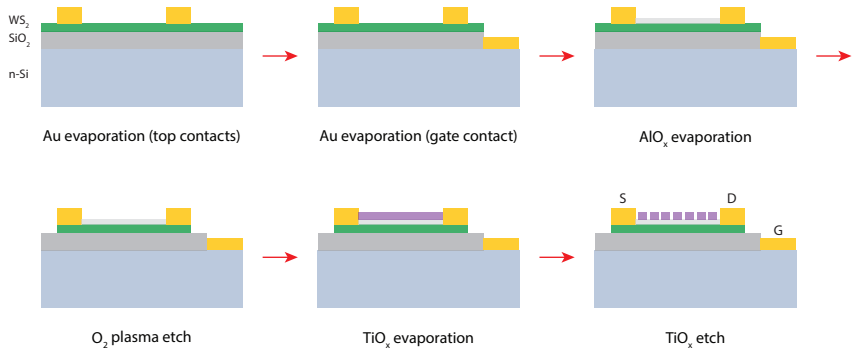

Figure 3.6: Schematics of steps needed for the entire metadevice nanofabrication. The letters S, D and G stands for *source*, *drain*, and *gate* electrode.

The final chip configuration chosen differs slightly from that shown in the schematics of Fig. 3.4a. Specifically, a second set of top contacts is added to the WS_2 layer resulting, essentially, in a MOSFET-like device. Employing this nomenclature, current measurements between source and drain allow for a quick check of the connection between the metal leads and the TMD monolayer.

The entire nanofabrication procedure consists of 4 consecutively aligned Electron-Beam Lithography (EBL) steps. The first one concerns the contacts to the monolayer:

- CVD-grown WS_2 on SiO_2/Si substrates were acquired from 2Dsemiconductors. As reported by the manufacturer, large centimeter-scale monolayers are first grown onto sapphire and then transferred onto SiO_2/Si substrates. The Si bottom layer is doped (concentration $\sim 5 \cdot 10^{18}$ cm^{-3}, n-type) and the SiO_2 layer thickness is $t_{SiO2} = 299$ nm, as measured via spectroscopic ellipsometry.
- The sample is rinsed for 5 minutes in acetone and for another 5 minutes in IPA to remove dirt and any organic residue.
- A bilayer of MMA (MMA(8.5)MAA EL9, 450 nm) and PMMA (PMMA 950k A8 diluted 1:1 in anisole, 245 nm) was spin-coated and baked at 150°C for 2 minutes (each layer). Au colloids (50 nm diameter) in aqueous solution are deposited using a pipette at the corners of the sample and dried on the hotplate at 90°C. The Au colloids are used for e-beam column alignment and focusing. Electra 92 conductive coating for e-beam resists is spun to facilitate dissipation of charge build-up as the substrate is partially insulating.

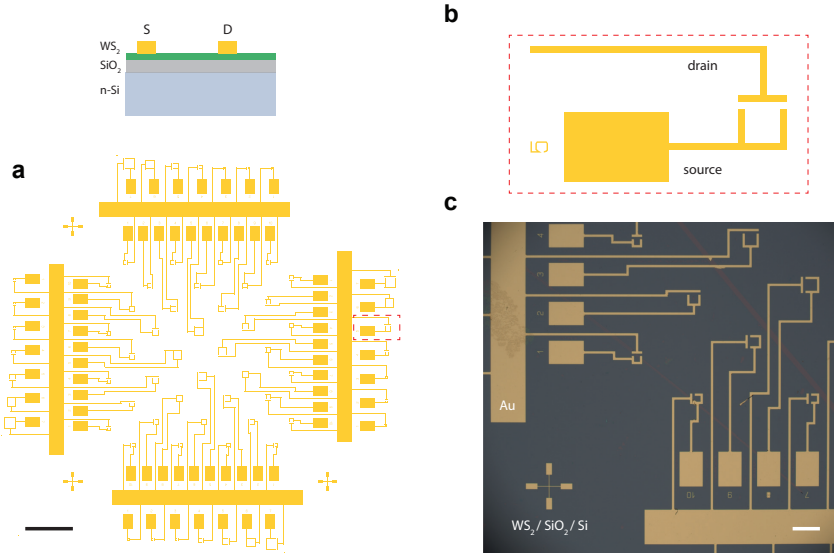

Figure 3.7: **a** Top view of the chip's contacts design (scale-bar 1 mm). **b** Single device layout zoomed in from panel a. **c** Optical microscopy image of a bottom left section of the chip after the first lift-off. The scale-bar is 200 μm.

- The contacts design in Fig. 3.7a is patterned in the resist layer by e-beam exposure using a Raith Voyager lithography system (50 kV, dose 650 $\mu C/cm^2$, current ~ 9.6 nA, step-size 50 nm) and development in MIBK:IPA (1:3 for 90 s). In this chip configuration, all the drain contacts are connected to 4 common pads while each device has its source lead connected to individual pads. Each quadrant contains 17 devices of different sizes ranging from 10×10 μm^2 to 200×200 μm^2. An example of a single device layout is depicted in Fig. 3.7b. Three sets of differently sized markers were exposed and used to align the consequent EBL steps.

- A 2 nm–thick Cr layer followed by a 100 nm–thick Au layer were evaporated using an in-house built thermal evaporator.

- The residual resist was lifted-off in acetone at 50°C. Ultra–sonication is avoided as it can peel off the WS_2 monolayer. Figure 3.7c shows the sample at this stage.

Second, the gate contact was fabricated:

- A 2 mm wide strip of polyester cleanroom tape (i.e. "blue tape") was applied on the sample next to the Au wiring. A thick PMMA (PMMA 950k A8 undiluted, 2.3 μm) layer was spin-coated and, before baking (150°C, 2 min), the blue tape was removed. This results in a strip where $WS_2/SiO_2/Si$ is exposed while the rest of the sample is protected by PMMA.

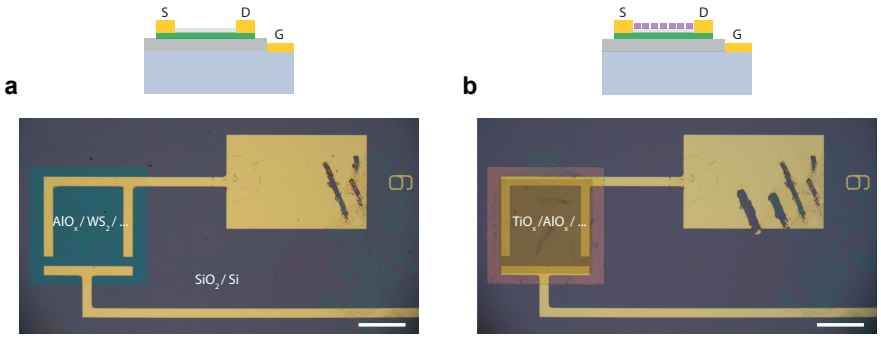

Figure 3.8: **a** Optical microscopy image of a single device after the AlO_x deposition and O_2 plasma etch. **b** Optical microscopy image of the same device after the TiO_x patterning. The scalebar is 100 μm for both panels.

- The exposed strip was scratched with a diamond pen. This is enough to partially remove SiO_2 and expose Si. To avoid native oxide regrowth, the sample was quickly transferred to the evaporator chamber which was consequently pumped down.
- Cr and Au were evaporated and lifted off with the same procedure described in the first EBL step.

Next, each device is capped with a thin AlO_x blanket. This layer serves as a hard mask to separate each device by etching away the WS_2 connecting them in an O_2 plasma. Furthermore, it acts as an etch stop layer in the final patterning step.

- A bilayer of MMA (MMA(8.5)MAA EL9, 567 nm) and PMMA (PMMA 950k A8 undiluted, 2.3 μm) was spin-coated and baked at 150°C for 2 minutes (each layer). Au colloids and Electra 92 are also deposited as in the first EBL step.
- Square voids aligned to the devices are fabricated in the resist layer by e-beam exposure using the Voyager lithography system (50 kV, dose 650 $\mu C/cm^2$, current ~ 10 nA, step-size 50 nm) and development in MIBK:IPA (1:3 for 90 s).
- A 11 nm–thick AlO_x layer was evaporated using an e-beam evaporator from a crucible filled with Al_2O_3 precursor.
- The residual resist was lifted-off in acetone at 50°C leaving isolated square AlO_x pads on the individual devices.
- Exposed WS_2 is etched using a 20 s O_2 plasma.

A representative device at this fabrication stage is shown in Fig. 3.8a. Next, the last EBL step is repeated with the only difference that TiO_x is evaporated instead of AlO_x. AlO_x and TiO_x thicknesses (11 nm and 96 nm respectively) and refractive indices were measured via ellipsometry. Finally, TiO_x is patterned by means of EBL and Reactive Ion Etching (RIE).

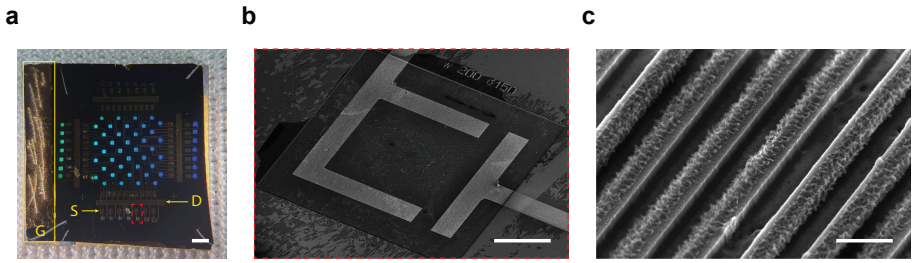

Figure 3.9: **a** Photograph of the entire chip (scalebar 1 mm). The letters S, D, and G indicate the position of the source, drain, and gate electrodes. **b** Tilted scanning electron microscopy (SEM) image of the patterned device highlighted in panel a (scalebar 50 μm). **c** Zoomed–in SEM image of the same device as in panel b (scalebar 500 nm).

- A 414 nm-thick layer of CSAR 62 (AR-P 6200, 13% in anisole) positive-tone resist (ALLRESIST GmbH) was spin-coated and baked for 2 minutes at 150°C. Again, Electra 92 conductive coating was spun as well.
- Lines were fabricated in the CSAR layer by exposure using the Voyager lithography system (50 kV, dose 145–150 $\mu C/cm^2$, current ~ 0.137 nA, step-size 4 nm) and development in Pentyl–acetate (60 s) and o–Xylene (5 s).
- The TiO_x layer is patterned by a RIE process employing CH_3, and O_2. The calculated etch rate is 8.3 nm/min for TiO_x and 23 nm/min for the CSAR resist mask. Furthermore, AlO_x is found to be resistant to the etch, as checked on a window with completely cleared resist. The detailed etch recipe parameters are:

CH_3 gas flow	50 [sccm]
O_2 gas flow	1 [sccm]
pressure	37.5 [mTorr]
Set temperature	21 [°C]
RIE forward power	200 [W]
ICP power	0 [W]
time	12 [min]

- The sample was left overnight in anisole at 60°C to remove the residual CSAR mask.

An overview of the entire chip after the described fabrication procedure is shown in Fig. 3.9a. A close inspection via SEM reveals good nano-beams uniformity over large areas with very low sidewall roughness. However, residual CSAR is left after the anisole bath (see Fig. 3.9c). Another more aggressive O_2 plasma clean to remove the resist was avoided as it was found detrimental to the excitonic properties of WS_2.

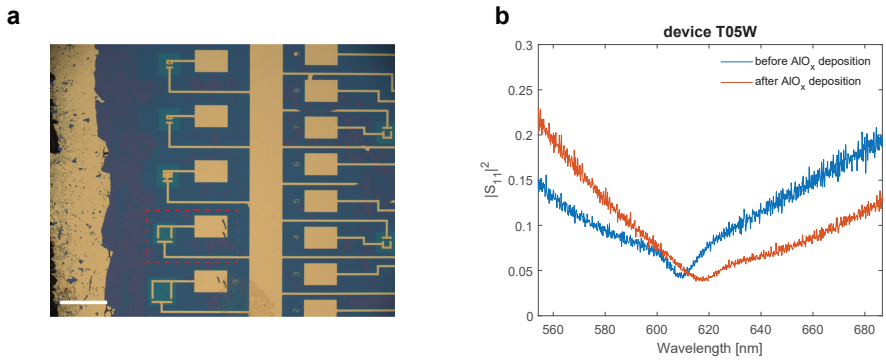

Figure 3.10: **a** Optical microscopy image of a portion of the chip's west quadrant after AlO_x liftoff (scalebar 200 μm). Device T05W is highlighted in the red dashed box. **b** Measured reflectance spectra of device T05W before and after AlO_x deposition and liftoff.

3.4. OPTOELECTRONIC CHARACTERIZATION

In order to optically and electrically characterize the fabricated sample, WITec's confocal microscope Alpha300 is coupled to a Keithley 2612 dual-channel source measure unit (SMU). On the optics side, light from a white LED is sent to the sample through a 50/50 beamsplitter and focused with a Zeiss EC Epiplan 20X (0.4 NA) objective. Reflected light can be sent to a CCD for standard imaging or, via fiber-coupling, to two different spectrometers. Spectrometer 1 is a WITec UHTS 300 equipped with an Andor iDus DV401A BV camera while Spectrometer 2 is an Acton SP-300i featuring an Andor iDus DV420A OE camera. On the electrical side, Keithley's SMU is controlled via Python and connected to the sample with two SUSS MicroTec PH 100 probe heads that can be easily moved around the chip to test the devices.

Using this setup, the reflectance of the individual devices in the chip is monitored at each fabrication step. The first notable change occurs as AlO_x pads are deposited to cap the devices (see Fig. 3.10a). Figure 3.10b shows the reflectance spectrum of device T05W[4] before and after the mentioned fabrication step. Regarding the experimental parameters, the aperture diaphragm (A-stop) is minimized to ensure the smallest illumination cone, no polarizer is inserted, the exposure time is 0.65 s × 20 accumulations and a 600 $^{\text{lines}}/_{\text{mm}}$ grating is used. It is easy to notice that the evaporation of alumina on the WS_2 monolayer causes a broadening of the excitonic resonance. This is presumably due to the creation of defect states at the interface between the two layers and could be potentially avoided by transferring a h-BN monolayer onto the sample before AlO_x deposition. Indeed, h-BN encapsulation was found to be beneficial to reduce the exciton linewidth [41].

After the O_2 plasma following the second EBL step, the devices are fully separated and ready to be individually tested electrically. Reflectance spectra are acquired as a

[4] Concerning the device labeling, the letter T indicates the devices in the outer side of each quadrant (i.e. test area) while the letter W refers to the West quadrant of the chip.

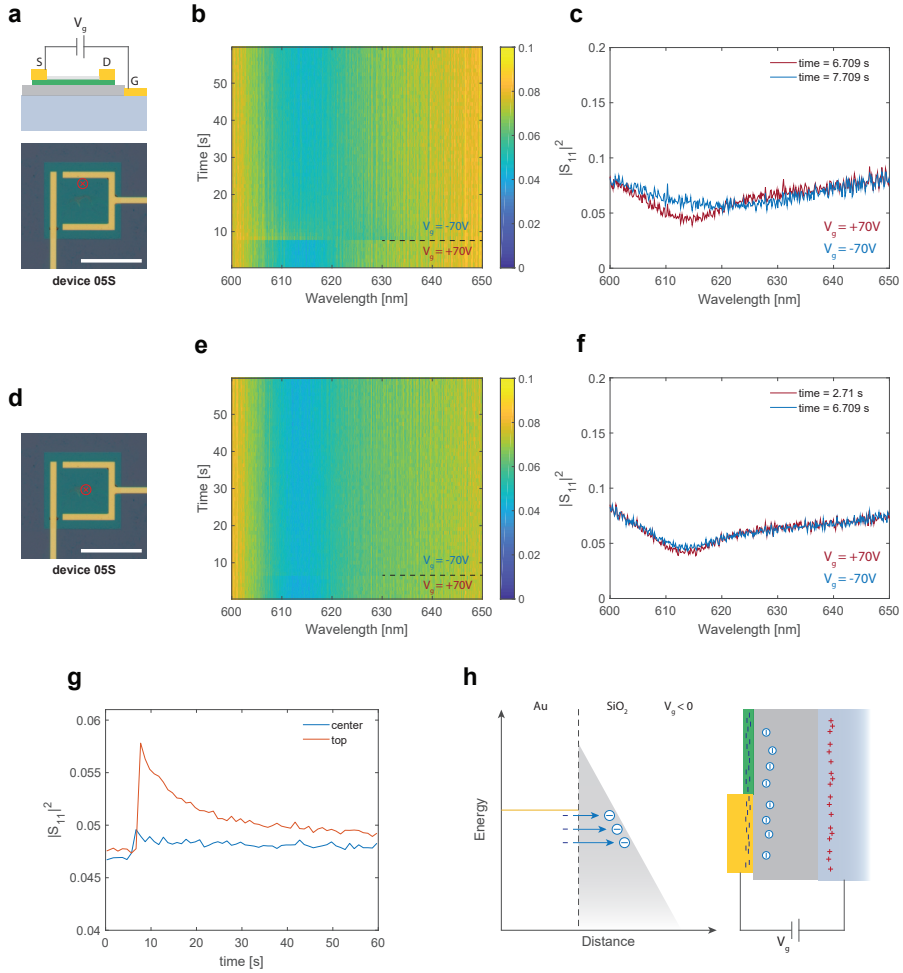

Figure 3.11: **a** Optical microscopy image of device 05S. The collection spot is indicated by the red cross. The schematic indicates the bias configuration. **b** Measured reflectance (color) spectra as function of time as the bias voltage is switched from $V_g = +70$ V to $V_g = -70$ V. The black dashed lines marks the time at which the bias is reversed. **c** Cross-cuts of panel b at two different times corresponding to different bias conditions. **d-f** Same as panels a-c but for a collection spot in the center of the device. **g** Measured reflectance as a function of time (vertical cross-cuts of panels b and e) averaged in the range 614 nm $< \lambda <$ 620 nm for the two different collection spots indicated in panels a-d. **h** Energy band diagram and schematic visualization of trap assisted tunneling injection. The scalebar is 200 μm for panels a and d.

function of time, gate bias, and acquisition location (see Fig. 3.11). Specifically, 60 spectra are acquired (1 spectrum per second, exposure time 0.2 s) and, within the time series, the bias voltage is reversed. The spectra are collected in the colormap in Fig. 3.11b for the collection spot indicated in panel a of the same figure. First, a positive bias does not have a tangible effect on the exciton resonance hinting at the possibility that the monolayer is still in its intrinsic state. In fact, hole injection is less efficient and WS_2 is slightly intrinsically n-doped from substrate [30]. Conversely, when the voltage is switched to $V_g = -70$ V, electrons are injected into WS_2 and the exciton is suppressed. Figure. 3.11c highlights two spectra taken right before and after bias inversion. Interestingly, a transient behavior is observed on a long timescale characterized by the reappearance of the exciton-related dip in reflectance. A similar phenomenon occurs if light is acquired from a central spot far from the Au leads (Fig. 3.11d). However, the modulation in reflection is much smaller in this case, as clear from Fig. 3.11f.

The dependence on time and space of the excitonic resonance is summarized in Fig. 3.11g, showing reflectance (averaged in the range 614 nm $< \lambda <$ 620 nm) as a function of time for the acquisition spots in panels a and d. First, the modulation amplitude in reflectance is $\sim$ 1% close to the contacts while is $<$ 0.5% at the center of the device. This could be caused by poor electron mobility in the monolayer which is presumably worsened by defects created during AlO_x deposition. Thus, electron doping might decrease with distance from the electrodes due to high sheet resistance.

Second, both signals show a decay as a function of time even if the voltage is kept constant. We attribute this to parasitic dielectric charging. Indeed, when a high electric field is applied ($\sim 2.3 \cdot 10^8$ V/m in the present case) charges from the metal electrode can be injected into the oxide layer [42]. The principal injection mechanism is Trap Assisted Tunneling (TAT) [43] where electrons can occupy defect states of various nature in the oxide layer via tunneling and remain trapped, as schematically depicted in Fig. 3.11h. Moreover, this migration implies a charge density decrease at the electrode [44] and hence effectively reduces doping in the WS_2 monolayer. This, in turn, results in less efficient exciton suppression. The dynamics of this phenomenon is essentially that of a charging parasitic capacitor, therefore the reflectance signal in Fig. 3.11g decays exponentially. It is worth mentioning that dielectric charging could be reduced by lowering the gate voltage. However, at $V_g > -50$ V no reflectance modulation was detectable suggesting that charge injection from Au to WS_2 might not be very efficient and the energy levels in Fig. 3.3c are probably complicated by Fermi level pinning [30].

Finally, the completed devices are characterized once more after the TiO_x patterning step. Again, reflectance spectra are acquired sequentially in time (40 spectra, cycle time 1.28 s, exposure time 1.25 s) and, during the time series, the bias polarity is switched. Moreover, light is polarized along the nanobeams' length. Reflectance spectra collected right before and after the bias switch are reported in Fig. 3.12b-c for the collection spot indicated in Fig. 3.12a. In agreement with the simulated data, the Fano resonance is redshifted compared to the exciton, and the reflectance swings from close to zero to $\sim$ 0.8, higher than the simulated counterpart.

The broadening described earlier results in a much less visible excitonic resonance compared to what is expected. Nonetheless, an asymmetric lineshape related to the exciton is clearly visible in Fig. 3.12c. Similar to what is shown in Fig. 3.4c, exciton suppres-

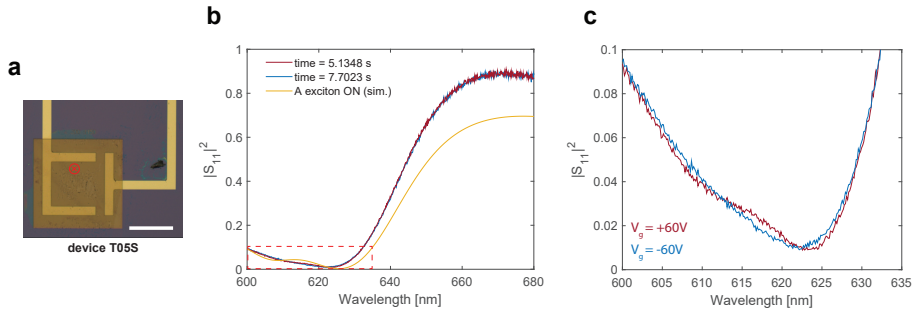

Figure 3.12: **a** Optical microscopy image (scalebar 100 μm) of device T05S after TiO_x patterning. The collection spot is indicated by the red cross. **b** Measured reflectance spectra as the bias voltage is switched from $V_g = +60$ V to $V_g = -60$ V. Simulated reflectance spectrum for the as–designed metasurface in its ON state. **c** Zoomed-in reflectance spectra showing the data in the red dashed box in panel b.

sion by electron injection generates a slight blue–shift in the Fano resonance and hence on its minimum. Once more, the experimental data demonstrates a smaller reflectance modulation but in the same direction as what is expected from simulation.

3.5. CONCLUSION AND OUTLOOK

In conclusion, this chapter presents a first proof-of-concept on how a gated TMD monolayer can be used to alter the transfer function of a high index metasurface to realize a switchable Fourier spatial filter.

First, a brief introduction on the physics of excitons in 2D TMDs is provided along with its consequences on the optical properties of the material. Application of a gate bias in a MOS-like configuration has a strong impact on the excitonic resonance and thus on the material's optical response. These concepts are used to design a metasurface that imparts a mathematical operation if an image is projected onto it. Specifically, the designed device acts as a high-pass filter that can be perturbed by the presence (or absence) of excitons in a WS_2 monolayer. The optimum design achieves a numerical aperture of 0.2 and a transmission amplitude close to 0.8 at the maximum k-vector processed. Next, the device's image processing capabilities are tested numerically on several test input images, demonstrating reliable edge filtering that can be turned on and off at $\lambda = 626$ nm and $\lambda = 620$ nm.

Aiming at the optimized design shown, a chip containing several devices is realized and the fabrication steps are discussed in detail. Each device is characterized optically and electrically by measuring reflectance spectra under a gate bias. The data demonstrate reflectance modulation triggered by external bias following the same trends predicted by simulations. It is worth highlighting that integration of such delicate atomically thin materials in a standard CMOS compatible fabrication flow is a daunting task,

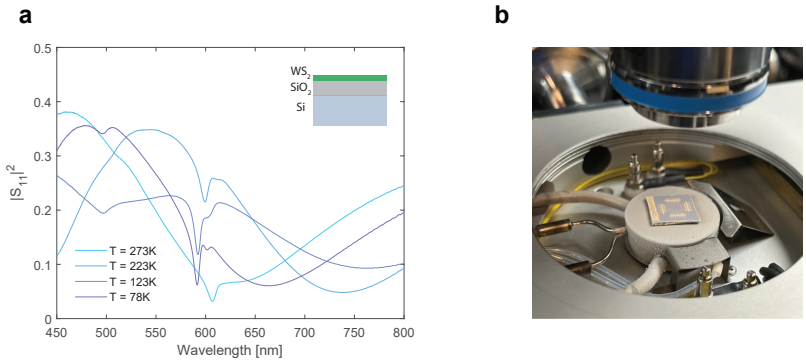

Figure 3.13: **a** Measured reflectance spectra of an MBE–grown WS_2 monolayer on a SiO_2/Si substrate (SiO_2 thickness ~ 310 nm) as a function of temperature. **b** Image of the fabricated sample in the cryostage.

yet it proved to be possible with many reproducibly functioning devices. Nonidealities are addressed along with possible causes and solutions. Among these, exciton linewidth broadening strongly reduces the reflectance modulation. To tackle this issue, an effort on low-temperature measurements has recently started. Indeed, as shown in Fig. 3.13a, the exciton resonance linewidth drastically decreases as temperature goes down. At T = 78 K the linewidth is ~ 5 nm, and the potential modulation in reflectance can be as high as 10% (absolute) in amplitude if the exciton is completely suppressed. As recently demonstrated in literature, this value can further increase with higher-quality exfoliated materials and even lower temperatures to further suppress phonon interactions [24, 25].

As an outlook, future experiments will aim at adding a cryostage to the Fourier microscope described in Section 2.6.2, also including the possibility of electrical control. This will enable measurements of the device's transfer function, along with its image processing capabilities. Finally, on the nano-fabrication side, h-BN encapsulation will be introduced into the fabrication flow to mitigate the exciton broadening and the Au/WS_2 interface quality will be investigated and further optimized.

Despite the analyzed experimental nonidealities, the results shown here open up new avenues for all-optical processing metasurfaces featuring functionalities that can be switched or even tuned in real-time.

REFERENCES

[1] P. Berto, L. Philippet, J. Osmond, C. F. Liu, A. Afridi, M. Montagut Marques, B. Molero Agudo, G. Tessier, and R. Quidant, *Tunable and free-form planar optics,* Nature Photonics **13**, 649 (2019).

[2] E. Arbabi, A. Arbabi, S. M. Kamali, Y. Horie, M. Faraji-Dana, and A. Faraon, *MEMS-tunable dielectric metasurface lens,* Nature Communications **9**, 812 (2018).

[3] A. L. Holsteen, A. F. Cihan, and M. L. Brongersma, *Temporal color mixing and dynamic beam shaping with silicon metasurfaces,* Science **365**, 257 (2019).

[4] N. A. Butakov, M. W. Knight, T. Lewi, P. P. Iyer, D. Higgs, H. T. Chorsi, J. Trastoy, J. Del Valle Granda, I. Valmianski, C. Urban, Y. Kalcheim, P. Y. Wang, P. W. C. Hon, I. K. Schuller, and J. A. Schuller, *Broadband electrically tunable dielectric resonators using metal–insulator transitions,* ACS Photonics **5**, 4056 (2018).

[5] N. A. Butakov, I. Valmianski, T. Lewi, C. Urban, Z. Ren, A. A. Mikhailovsky, S. D. Wilson, I. K. Schuller, and J. A. Schuller, *Switchable plasmonic–dielectric resonators with metal–insulator transitions,* ACS Photonics **5**, 371 (2018).

[6] X. Duan, S. Kamin, and N. Liu, *Dynamic plasmonic colour display,* Nature Communications **8**, 14606 (2017).

[7] J. van de Groep, J.-H. Song, U. Celano, Q. Li, P. G. Kik, and M. L. Brongersma, *Exciton resonance tuning of an atomically thin lens,* Nature Photonics **14**, 426 (2020).

[8] S. Biswas, M. Y. Grajower, K. Watanabe, T. Taniguchi, and H. A. Atwater, *Broadband electro-optic polarization conversion with atomically thin black phosphorus,* Science **374**, 448 (2021).

[9] M. Li, S. Biswas, C. U. Hail, and H. A. Atwater, *Refractive index modulation in monolayer molybdenum diselenide,* Nano Letters **21**, 7602 (2021).

[10] Z. Yu, A. Raman, and S. Fan, *Fundamental limit of nanophotonic light trapping in solar cells,* Proceedings of the National Academy of Sciences **107**, 17491 (2010).

[11] T. Mueller and E. Malic, *Exciton physics and device application of two-dimensional transition metal dichalcogenide semiconductors,* npj 2D Materials and Applications **2**, 29 (2018).

[12] S. Manzeli, D. Ovchinnikov, D. Pasquier, O. V. Yazyev, and A. Kis, *2D transition metal dichalcogenides,* Nature Reviews Materials **2**, 17033 (2017).

[13] K. S. Novoselov, D. Jiang, F. Schedin, T. J. Booth, V. V. Khotkevich, S. V. Morozov, and A. K. Geim, *Two-dimensional atomic crystals,* Proceedings of the National Academy of Sciences **102**, 10451 (2005).

[14] L. Britnell, R. M. Ribeiro, A. Eckmann, R. Jalil, B. D. Belle, A. Mishchenko, Y.-J. Kim, R. V. Gorbachev, T. Georgiou, S. V. Morozov, a. N. Grigorenko, a. K. Geim, C. Casiraghi, a. H. C. Neto, and K. S. Novoselov, *Strong Light-Matter Interactions in Heterostructures of Atomically Thin Films,* Science **340**, 1311 (2013).

[15] K. F. Mak, C. Lee, J. Hone, J. Shan, and T. F. Heinz, *Atomically thin MoS_2: A new direct-gap semiconductor,* Phys. Rev. Lett. **105**, 136805 (2010).

[16] W. Zhao, Z. Ghorannevis, L. Chu, M. Toh, C. Kloc, P.-H. Tan, and G. Eda, *Evolution of electronic structure in atomically thin sheets of WS_2 and WSe_2,* ACS Nano **7**, 791 (2013).

[17] A. Chernikov, T. C. Berkelbach, H. M. Hill, A. Rigosi, Y. Li, O. B. Aslan, D. R. Reichman, M. S. Hybertsen, and T. F. Heinz, *Exciton Binding Energy and Nonhydrogenic Rydberg Series in Monolayer WS_2,* Physical Review Letters **113**, 076802 (2014).

[18] G. Grosso and G. Parravicini, *Solid State Physics* (Elsevier Science, 2013).

[19] L. Claudio Andreani, *Optical transitions, excitons, and polaritons in bulk and low-dimensional semiconductor structures,* in *Confined Electrons and Photons: New Physics and Applications*, edited by E. Burstein and C. Weisbuch (Springer US, Boston, MA, 1995) pp. 57–112.

[20] P. Y. Yu and M. Cardona, *Optical properties i,* in *Fundamentals of Semiconductors: Physics and Materials Properties* (Springer Berlin Heidelberg, Berlin, Heidelberg, 2010) pp. 243–344.

[21] Y. Li, A. Chernikov, X. Zhang, A. Rigosi, H. M. Hill, A. M. van der Zande, D. A. Chenet, E.-M. Shih, J. Hone, and T. F. Heinz, *Measurement of the optical dielectric function of monolayer transition-metal dichalcogenides:MoS_2, $MoSe_2$, WS_2, and WSe_2,* Phys. Rev. B **90**, 205422 (2014).

[22] G. Moody, C. Kavir Dass, K. Hao, C.-H. Chen, L.-J. Li, A. Singh, K. Tran, G. Clark, X. Xu, G. Berghäuser, E. Malic, A. Knorr, and X. Li, *Intrinsic homogeneous linewidth and broadening mechanisms of excitons in monolayer transition metal dichalcogenides,* Nature Communications **6**, 8315 (2015).

[23] A. Ramasubramaniam, *Large excitonic effects in monolayers of molybdenum and tungsten dichalcogenides,* Phys. Rev. B **86**, 115409 (2012).

[24] G. Scuri, Y. Zhou, A. A. High, D. S. Wild, C. Shu, K. De Greve, L. A. Jauregui, T. Taniguchi, K. Watanabe, P. Kim, M. D. Lukin, and H. Park, *Large excitonic reflectivity of monolayer $MoSe_2$ encapsulated in hexagonal boron nitride,* Phys. Rev. Lett. **120**, 037402 (2018).

[25] P. Back, S. Zeytinoglu, A. Ijaz, M. Kroner, and A. Imamoğlu, *Realization of an electrically tunable narrow-bandwidth atomically thin mirror using monolayer $MoSe_2$,* Phys. Rev. Lett. **120**, 037401 (2018).

[26] R. G. Southwick, A. Sup, A. Jain, and W. B. Knowlton, *An interactive simulation tool for complex multilayer dielectric devices,* IEEE Transactions on Device and Materials Reliability **11**, 236 (2011).

[27] Y. Yu, Y. Yu, L. Huang, H. Peng, L. Xiong, and L. Cao, *Giant gating tunability of optical refractive index in transition metal dichalcogenide monolayers,* Nano Letters **17**, 3613 (2017).

[28] S. Sze and K. Ng, *Metal-insulator-semiconductor capacitors,* in *Physics of Semiconductor Devices* (John Wiley & Sons, Ltd, 2006) pp. 197–240.

[29] B. Sapoval, C. Hermann, and A. King, *Physics of Semiconductors* (Springer-Verlag, 1995).

[30] Y. Wang and M. Chhowalla, *Making clean electrical contacts on 2D transition metal dichalcogenides,* Nature Reviews Physics **4**, 101 (2022).

[31] M. Li, S. Biswas, C. U. Hail, and H. A. Atwater, *Refractive index modulation in monolayer molybdenum diselenide,* Nano Letters **21**, 7602 (2021).

[32] M. A. Green, *Self-consistent optical parameters of intrinsic silicon at 300K including temperature coefficients,* Solar Energy Materials and Solar Cells **92**, 1305 (2008).

[33] I. H. Malitson, *Interspecimen comparison of the refractive index of fused silica,* J. Opt. Soc. Am. **55**, 1205 (1965).

[34] B. Luk'yanchuk, N. I. Zheludev, S. A. Maier, N. J. Halas, P. Nordlander, H. Giessen, and C. T. Chong, *The Fano resonance in plasmonic nanostructures and metamaterials,* Nature Materials **9**, 707 (2010).

[35] A. E. Miroshnichenko, S. Flach, and Y. S. Kivshar, *Fano resonances in nanoscale structures,* Reviews of Modern Physics **82**, 2257 (2010).

[36] L. Andreani and M. Agio, *Photonic bands and gap maps in a photonic crystal slab,* IEEE Journal of Quantum Electronics **38**, 891 (2002).

[37] S. Fan and J. D. Joannopoulos, *Analysis of guided resonances in photonic crystal slabs,* Physical Review B **65**, 235112 (2002).

[38] G. Pitruzzello and T. F. Krauss, *Photonic crystal resonances for sensing and imaging,* Journal of Optics **20**, 073004 (2018).

[39] S. S. Wang and R. Magnusson, *Theory and applications of guided-mode resonance filters,* Applied Optics **32**, 2606 (1993).

[40] S. S. Wang, M. G. Moharam, R. Magnusson, and J. S. Bagby, *Guided-mode resonances in planar dielectric-layer diffraction gratings,* Journal of the Optical Society of America A **7**, 1470 (1990).

[41] F. Cadiz, E. Courtade, C. Robert, G. Wang, Y. Shen, H. Cai, T. Taniguchi, K. Watanabe, H. Carrere, D. Lagarde, M. Manca, T. Amand, P. Renucci, S. Tongay, X. Marie, and B. Urbaszek, *Excitonic linewidth approaching the homogeneous limit in MoS_2-based van der waals heterostructures,* Phys. Rev. X **7**, 021026 (2017).

[42] A.-C. Amiaud, A. Leuliet, B. Loiseaux, J.-P. Ganne, and J. Nagle, *Modeling of dielectric charging in capacitive structures,* Journal of Applied Physics **118**, 174103 (2015).

[43] R. Ramprasad, *Phenomenological theory to model leakage currents in metal–insulator–metal capacitor systems,* physica status solidi (b) **239**, 59 (2003).

[44] J. Wibbeler, G. Pfeifer, and M. Hietschold, *Parasitic charging of dielectric surfaces in capacitive microelectromechanical systems (MEMS),* Sensors and Actuators A: Physical **71**, 74 (1998).

4

INTEGRAL EQUATIONS

As standard microelectronic technology approaches fundamental limitations in speed and power consumption, novel computing strategies are strongly needed. Analog optical computing enables processing large amounts of data at a negligible energy cost and high speeds. Based on these principles, ultra-thin optical metasurfaces have been explored to process large images in real-time, in particular for edge detection.

Within this chapter, an ultra-thin Si metasurface-based platform for analog computing that is able to solve Fredholm integral equations of the second kind using free-space visible radiation is presented. A Si-based metagrating was inverse-designed to implement the scattering matrix synthesizing a prescribed Kernel corresponding to the mathematical problem of interest. Next, a semi-transparent mirror was incorporated into the sample to provide adequate feedback and thus perform the required Neumann series solving the corresponding equation in the analog domain at the speed of light. Visible wavelength operation enables a highly compact, ultra-thin device that can be interrogated from free space, implying high processing speeds and the possibility of on-chip integration.

4.1. THEORY AND DESIGN

THE idea of using light to outsource specific computing tasks comes with several advantages. First, there is a clear enhancement in processing speeds as the computation is performed at the speed of light traveling through metamaterials with typical sizes smaller than or comparable to the wavelength of operation. Also, processing signals in the optical domain enables massive parallelization and may potentially avoid unnecessary analog-to-digital conversion. As shown in the previous chapters, several image processing tasks can be performed before the image is discretized into pixels, relying on the possibility of engineering the angular response of metasurfaces and hence impart instantaneously a mathematical operation to the spatial content of an input signal. Finally, analog computing meta-devices can be passive, implying an extremely low energy usage.

A key question is whether it is possible to go beyond simple image processing tasks and focus on a more complex mathematical problem, such as solving a linear integral equation. The latter is an equation containing the unknown function within an integral and can be categorized in two ways:

- If the limits of integration $[a, b]$ are fixed, the equation is labeled as *Fredholm* equation, otherwise it is a *Volterra* equation. The following is an example of a Volterra equation:

$$g(u) = f(u) + \int_a^u K(u, v)g(v)\mathrm{d}v \tag{4.1}$$

- If the unknown function appears only under the integral sign, the equation is labeled as *first kind*. If it appears both inside and outside the integral, it is labeled *second kind*. As an example, this is a Fredholm equation of the first kind:

$$f(u) = \int_a^b K(u, v)g(v)\mathrm{d}v \tag{4.2}$$

In the examples presented, $g(u)$ is the unknown function that the equation has to be solved for, while the known function of two variables $K(u, v)$ is called *kernel*. The extra function $f(u)$ is also assumed to be known. If $f(u) = 0$, the equation is said to be homogeneous.

Integral equations are present in several scientific fields, for example, scattering (e.g. quantum theory of scattering by a potential [1]) and transport phenomena. Moreover, it is more convenient to recast some specific problems described by differential equations with boundary conditions into integral equations [2]. Furthermore, as it will be clear later, the platform presented here allows mapping of discretized arbitrary linear operators and inversion of those. Hence, it is applicable to any generic linear inverse problem.

The concept of a wave-based integral equation solver has been recently demonstrated in the microwave regime for symmetric and non-symmetric kernels and in a multi-frequency parallel fashion [3, 4], but relying on guided waves in bulky metamaterial setups. An important next challenge is to demonstrate if such a complex mathematical operation can be carried out in the optical spectral range, ideally within an ultrathin form factor that can be interrogated through free-space radiation. This will enable the fabrication of far more compact on-chip devices operated at wavelengths that

are widely used for communication technology. This dramatic size reduction further implies a drastic increase in processing speeds as light has to travel much shorter distances. Here, we demonstrate a Si metasurface-based optical platform that combines a tailored scattering matrix design and a feedback system to enable the solution of Fredholm integral equations of the second kind from the far-field

$$g(u) = I_{\text{in}}(u) + \int_a^b K(u,v)g(v)\mathrm{d}v \tag{4.3}$$

where $g(u)$ is the unknown solution of Eq.(4.3), $K(u,v)$ is the kernel of the integral operator, and $I_{\text{in}}(u)$ is an arbitrary input function. Mathematically, this form of equation may be analytically solvable if it is in separable form or for some special kernels, and an inversion formula may exist (e.g., a Fourier transform). However, when certain convergence conditions for the kernels are satisfied a general technique to solve Eq.(4.3) is to exploit the Neumann successive approximation method: we assume an initial guess $g_0(u) = I_{\text{in}}(u)$ and successive approximations can be obtained by evaluating $g_{i+1}(u) = I_{\text{in}}(u) + \int_a^b K(u,v)g_i(v)\mathrm{d}v$, whereupon eventually $g_n(u)$ converges to the solution $g(u)$ as $n \to \infty$ [2]. Here, we show how to physically implement this iterative procedure in an analog fashion employing a Si metasurface coupled to a feedback system.

First, Eq.(4.3) is discretized by sampling its independent variables, u and v, over N points in the interval $[a,b]$ to form two vectors with such variables $\mathbf{u}$ and $\mathbf{v}$. The application of the integral operator $\int_a^b K(u,v)[]\mathrm{d}v$ on the function $g(u)$ is then analogous to the multiplication (or application) of a matrix operator $\mathsf{K} = K(\mathbf{u},\mathbf{v})\frac{a-b}{N}$ on a vector $\mathbf{g} = g(\mathbf{u})$. Thus, Eq.(4.3) may be numerically approximated by the $N \times N$ matrix equation

$$\mathbf{g} = \mathbf{I}_{\text{in}} + \mathsf{K}\mathbf{g} \tag{4.4}$$

Second, the solution $\mathbf{g}$ is represented as a Neumann series

$$\mathbf{g} = \sum_i (\mathsf{K})^i \mathbf{I}_{\text{in}} + = (\mathbb{I}_N - \mathsf{K})^{-1} \tag{4.5}$$

where $\mathbb{I}_N$ is the $N \times N$ identity matrix. The convergence of the Neumann series demonstrates that the inverse operator $(\mathbb{I}_N - \mathsf{K})$ exists. Next, it is possible to think of the N mathematical sampling points as N discrete physical modes, and thus $\mathbf{g}$ is a vector representing the complex amplitude of these modes on a given plane with a chosen direction. The integral operator can then be represented by a scattering matrix that performs matrix multiplication between these sets of modes.

If we consider a periodic metagrating, the input/output modes can be mapped into the N discrete diffraction channels determined by the periodicity and the wavelength, while the discretized integral operator K can be mapped onto the metasurface scattering matrix S that governs the coupling between these channels.

Following the schematics in Fig. 4.1, the discretized input $\mathbf{I}_{\text{in}}$ is a vector of length N containing the complex amplitudes of the plane waves addressing the system via its available diffraction channels, acting as seed guess $\mathbf{g_0} = \mathbf{I}_{\text{in}}$. The vector is multiplied by the metasurface scattering matrix upon its first reflection, resulting in a more refined

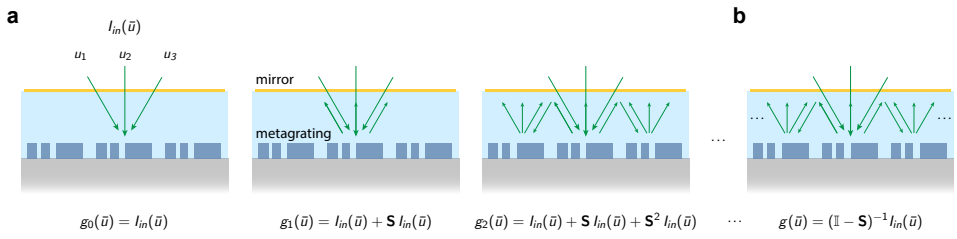

Figure 4.1: An input vector $\mathbf{I}_{\text{in}}$ is fed to the system in the form of N plane waves with different complex amplitudes incident along N diffraction channels. The signal interacts repeatedly with a metagrating bouncing back from a partially reflecting mirror, each time multiplied by the metagrating scattering matrix and therefore building up the terms of a Neumann series of subsequent matrix multiplications required for solving the integral equation. For the sake of simplicity, the formulas underneath the panels do not take into account the semi-transparent mirror scattering matrix at this stage.

guess $\mathbf{g_1}$ to the solution of the integral equation associated with K. The signal is then reflected by a semitransparent mirror and fed back to the grating for the next iteration. Intuitively, the system performs an analog Neumann series operation at the speed of light by iteratively applying the S matrix on the seed vector through multiple reflections, in the same way the mathematical integral operator is applied repeatedly on the initial guess function.

The entire computing metastructure is therefore composed of two elements: (1) a metagrating with a period that determines the number of input-output modes (grating orders), and unit cell with tailored geometry defining the scattering matrix of interest, (2) a semi-transparent mirror enabling feedback and in-coupling combined with a spacer layer.

4.1.1. KERNEL DESIGN

At the foundations of the analogy between the integral equation solving and the behavior of an optimized periodic metagrating coupled to a feedback lies the requirement of designing the S-matrix of a periodic structure by setting its periodicity (i.e., the number of input/output modes and hence the dimension of the S-matrix) and optimizing its unit cell (i.e., optimize the coupling of light into the defined diffraction modes in amplitude and phase).

First, we set the periodicities p and w of the grating (Fig. 4.2a) to have three diffraction orders in reflection at the target wavelength $\lambda_0 = 706$ nm. We choose this wavelength because it is still within the visible spectral range while Si losses are less severe, light sources in this spectral range are readily accessible, and the corresponding submicron unit cell footprint enables compact circuit design and integration. Specifically, we choose $w = 825$ nm while the orthogonal periodicity $w = 400$ nm is set to be subwavelength. This enhances the degrees of freedom for the unit cell design without opening additional diffraction channels. Hence, the system is addressed by six ports corresponding to six different diffraction channels (Fig. 4.2b) at angles $\theta_0 = \sin^{-1}\left(\lambda_0/p\; n_{\text{sup}}\right)$, $\theta_T = \sin^{-1}\left(\lambda_0/p\; n_{\text{sub}}\right)$ where n_{sup}, n_{sub} are the superstrate (SiO_2) and substrate (Al_2O_3) refractive indices respectively.

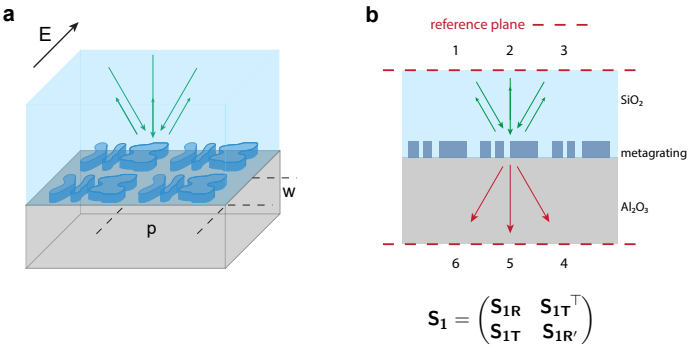

Figure 4.2: **a** Schematic illustration of a 2D metagrating (periodicities p and w) with a suitably engineered unit cell geometry. The black arrow indicates the polarization (TE) of the incoming E field. **b** Schematics of the input and output ports including the related reference planes for the metagrating and corresponding S-matrix.

The plane waves probing the system via these diffraction channels are TE polarized and the linear relationship between these incident, transmitted, and reflected waves defines the scattering matrix of the system. The s-parameters defining this matrix are complex numbers normalized such that $|S_{ij}|^2$ is the transmittance to port i when port j is illuminated (taking into account refractive indices and angles)

$$\mathsf{S}_1 = \begin{pmatrix} \mathsf{S}_{1R} & \mathsf{S}_{1T}{}^{\top} \\ \mathsf{S}_{1T} & \mathsf{S}_{1R'} \end{pmatrix} = \begin{pmatrix} r_{11} & r_{12} & r_{13} & t_{14} & t_{15} & t_{16} \\ r_{21} & r_{22} & r_{23} & t_{24} & t_{25} & t_{26} \\ r_{31} & r_{32} & r_{33} & t_{34} & t_{35} & t_{36} \\ t_{41} & t_{42} & t_{43} & r_{44} & r_{45} & r_{46} \\ t_{51} & t_{52} & t_{53} & r_{54} & r_{55} & r_{56} \\ t_{61} & t_{62} & t_{63} & r_{64} & r_{65} & r_{66} \end{pmatrix} \tag{4.6}$$

where S_{1R} and S_{1T} are the reflection and transmission sub-blocks. Since the Neumann series is performed in reflection, only the reflection sub-block S_{1R} needs to be designed: it contains the complex reflection coefficients connecting the diffraction channels in the spacer layer above the metagrating. It is important to stress that the choice of working with the reflective part of the s-matrix allows for a configuration that is easier to fabricate experimentally but limits the generality of the kernels that can be implemented to symmetric ones. However, these concepts may be extended to more general kernels by optimizing the transmissive block of the s-matrix and with an appropriate feedback system.

To prove the generality of our approach, we began our problem by choosing a random passive and reciprocal (i.e., symmetric) matrix with $N = 3$

$$\mathsf{S}_{1R} = \begin{pmatrix} 0.239 + 0.052i & -0.233 - 0.083i & 0.246 + 0.329i \\ -0.233 - 0.083i & -0.381 - 0.514i & 0.339 - 0.262i \\ 0.246 + 0.329i & 0.339 - 0.262i & -0.314 + 0.156i \end{pmatrix}. \tag{4.7}$$

Inverse design techniques [5–10] were utilized in order to create a design that satisfies the 9 constraints contained within S_{1R}. Specifically, the grating unit cell topology is

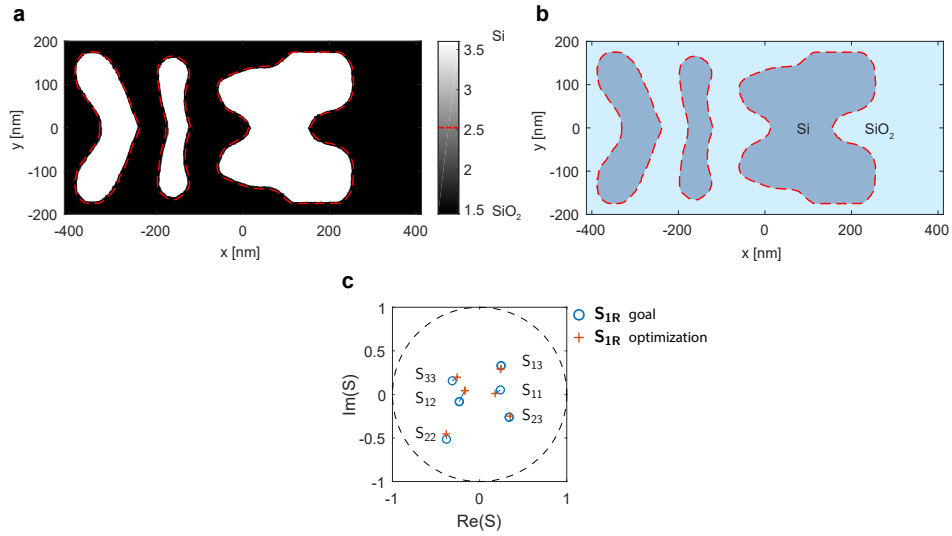

Figure 4.3: **a** Optimized unit cell refractive index distribution (gray-scale). Black indicates the refractive index of SiO_2 while white indicates that of Si. The colormap is continuous even if it appears binarized. The red dashed line indicated the contour used to generate the final unit cell. **b** Binarized metagrating unit-cell made of silicon (blue) and SiO_2 (light blue). **c** Simulation results for the S_{1R} matrix elements of the inverse-designed metagrating (orange crosses) and the corresponding desired matrix elements (blue circles).

optimized employing COMSOL Multiphysics's optimization module while the height h of the etched silicon unit cell is set to 150 nm. The figure-of-merit to be minimized during the optimization is the sum of the squared "distances" on the complex plane between the complex-valued matrix elements of the S matrix of a designed geometry and the prescribed ones in Eq.(4.7), $\text{FOM} = \sum_{i,j} \left| S_{1R\,ij} - S_{1R-\text{opt}\,ij} \right|^2$. Also, polarization conversion is minimized as it would open extra channels effectively changing the dimension of S_1. During the optimization, the unit cell permittivity distribution (Fig. 4.3a) is periodically blurred to avoid small features that are hard to fabricate and a soft step function is applied to drive the optimum toward a more binary configuration. Also, the mesh size was reduced along the iterations to increase the accuracy of the simulation. Once the desired figure of merit is reached for an experimentally feasible unit cell, the permittivity distribution is fully binarized: all the domains with a refractive index below and above the threshold $(n_{Si}+n_{SiO_2})/2 \simeq 2.6$ are converted to SiO_2 and Si respectively, therefore obtaining the final unit cell design (Fig. 4.3b). Furthermore, by changing the latter threshold, it is possible to generate expanded and eroded designs that are used to study the design tolerance to fabrication imperfections.

As shown in (Fig. 4.3d), the optimized metagrating approximates very well the desired S matrix, achieving a figure of merit as low as 0.058. This demonstrates that it is possible to inverse-design metagratings with a prescribed S–matrix, showing the feasibility of this optical computing concept for the solution of integral equations with a wide range of kernels.

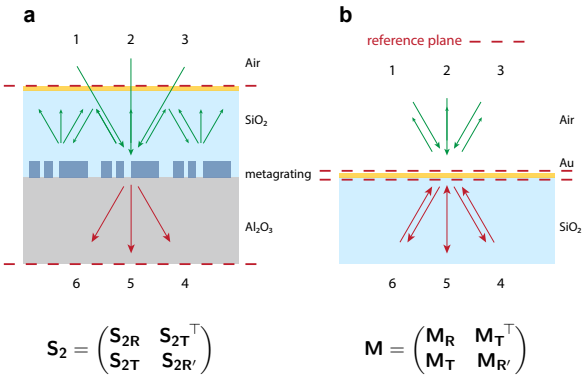

Figure 4.4: Schematics of the input and output ports including the related reference planes for **a** entire metastructure and **b** semi-transparent mirror. The corresponding S-matrix is underneath each panel.

4.1.2. MATRIX INVERSION

What is discussed so far concerns only the design of the metagrating scattering matrix mapping the discretized integral Kernel operator K in Eq.(4.4). Next, to find the solution of the integral equation it is crucial to have a feedback system that repeatedly returns the signal reflected from the metagrating back to it, so that the Neumann series is constructed. To this end, the SiO_2 spacer is covered with a 15 nm thick Au layer to form a semitransparent mirror [11]. The distance between the metagrating and mirror is 487 nm $\simeq \lambda_0/n_{SiO_2}$ to avoid near-field coupling, which may introduce additional modes into the system. The S matrix characterizing the mirror is

$$\mathsf{M} = \begin{pmatrix} \mathsf{M}_\mathsf{R} & \mathsf{M}_\mathsf{T}^\top \\ \mathsf{M}_\mathsf{T} & \mathsf{M}_{\mathsf{R}'} \end{pmatrix} \tag{4.8}$$

where $\mathsf{M}_{\mathsf{R}'}$ is the sub-block representing reflection from the SiO_2 side and M_T is its transmission counterpart. Including the mirror, the scattering matrix of the entire metastructure (grating, SiO_2 spacer, and mirror) becomes

$$\mathsf{S}_2 = \begin{pmatrix} \mathsf{S}_{2\mathsf{R}} & \mathsf{S}_{2\mathsf{T}}^\top \\ \mathsf{S}_{2\mathsf{T}} & \mathsf{S}_{2\mathsf{R}'} \end{pmatrix}. \tag{4.9}$$

The Neumann series, and thus the solution of Eq.(4.4), is embedded in S_2. The transmission of the entire stack, as measured in our experiment, is composed of a sum of terms each corresponding to an increasing number of interactions with the metagrating (see figs. 4.5a, 4.1) [12]:

$$\mathsf{S}_{2\mathsf{T}} = \mathsf{S}_{1\mathsf{T}}\mathsf{M}_\mathsf{T} + \mathsf{S}_{1\mathsf{T}}\mathsf{M}_{\mathsf{R}'}\mathsf{S}_{1\mathsf{R}}\mathsf{M}_\mathsf{T} + \mathsf{S}_{1\mathsf{T}}\left(\mathsf{M}_{\mathsf{R}'}\mathsf{S}_{1\mathsf{R}}\right)^2\mathsf{M}_\mathsf{T} + \cdots = \mathsf{S}_{1\mathsf{T}}\left(\mathbb{I}_3 - \mathsf{M}_{\mathsf{R}'}\mathsf{S}_{1\mathsf{R}}\right)^{-1}\mathsf{M}_\mathsf{T}. \tag{4.10}$$

The transmission sub-block $\mathsf{S}_{2\mathsf{T}}$ is composed of the inverse operator $\left(\mathbb{I}_3 - \mathsf{M}_{\mathsf{R}'}\mathsf{S}_{1\mathsf{R}}\right)^{-1}$ solving Eq.(4.4) multiplied by the mirror transmission M_T and by the metasurface transmission $\mathsf{S}_{1\mathsf{T}}$. In other words, light is coupled into the system passing through the mirror first, and then the solution is outcoupled via the metasurface. Hence, to extract the solution computed by the metastructure, i.e. the linear combination of complex amplitudes

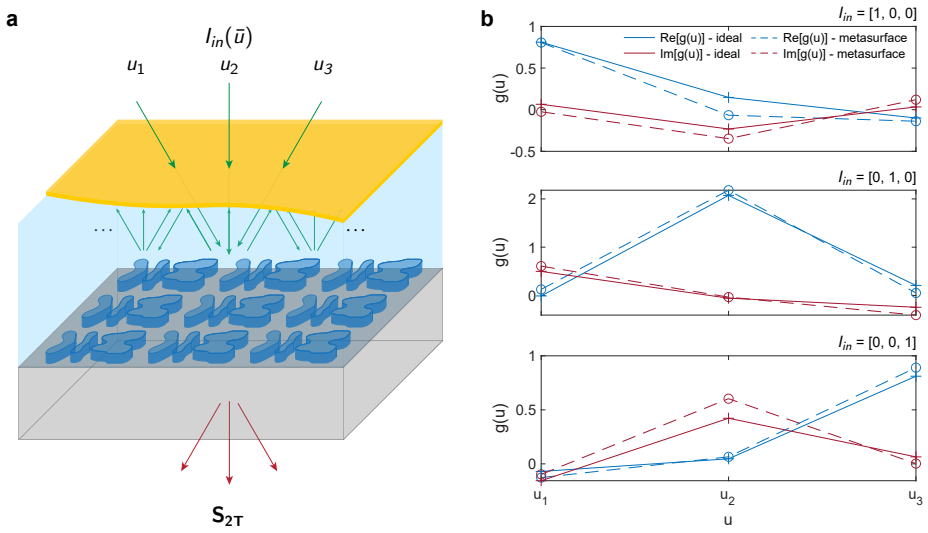

Figure 4.5: **a** The solution of Eq.(4.4) is built up inside the spacer layer in the form of a collection of complex wave amplitudes, one for each discrete diffraction channel. The solution is outcoupled and read out in transmission.**b** Analog solution (real and imaginary parts) of the integral equation (dashed line) obtained from the simulation results for the metastructure transmission, compared with the ideal theoretical solution $\mathbf{g} = (\mathbb{I}_N - \mathsf{K})^{-1}$ (solid lines), for the three orthogonal input vectors $(1,0,0)^\mathsf{T}$, $(0,1,0)^\mathsf{T}$, $(0,0,1)^\mathsf{T}$. The wavelength of operation in this simulation is $\lambda_0 = 706$ nm.

of the diffracted modes inside the spacer layer that converges after multiple passes, $\mathsf{M_T}$ and $\mathsf{S_{1T}}$ must be de-embedded from $\mathsf{S_{2T}}$.

Figure 4.5b compares the solution $\mathsf{M_T}^{-1}\mathsf{S_{2T}}\mathsf{S_{1T}}^{-1}$ provided by the simulated metastructure transmission to the ideal solution of Eq.(4.4) with $\mathsf{K} = \mathsf{M_{R'}}\mathsf{S_{1R}}$ and $\mathbf{I}_{\text{in}}$ equal to the vectors belonging to the canonical basis generating the space of all possible input vectors (i.e., $(1,0,0)^\mathsf{T}$, $(0,1,0)^\mathsf{T}$, $(0,0,1)^\mathsf{T}$). Any input vector can be expressed as a linear combination of these, and given the linearity of the metasurface, agreement in the response for these basic excitations ensures that the structure can solve the integral equation problem for arbitrary inputs. The metasurface-based analog solution and the ideal solution show good agreement for all the inputs, both in terms of the real and imaginary part. Minor discrepancies are ascribed to the small difference between the desired S matrix and the optimized one (see Fig. 4.3c) and this result demonstrates that it is possible to design the desired kernel K and invert $(\mathbb{I}_3 - \mathsf{K})$ in a fully analog fashion.

4.2. EXPERIMENT

In this section, the experimental implementation of the all-optical integral equation solving metasurface is described in detail.

4.2.1. FABRICATION

The following fabrication steps were performed to obtain the optimized geometry analyzed in the previous section (see Fig. 4.6):

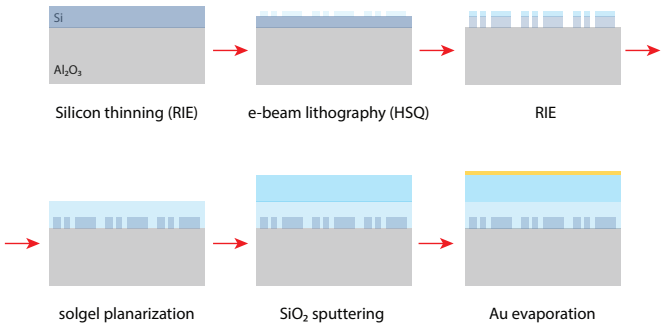

Figure 4.6: Schematics of the fabrication steps needed for the entire metastructure.

- c-Si on Al_2O_3 substrates were acquired from MTI corp. The c-Si (orientation: (100)) layer is 500 nm–thick, polished (surface roughness $R_q < 2.5$ nm) and undoped. The sapphire (orientation: *R*–plane) substrate is 0.46 mm–thick and double–side polished (surface roughness < 0.3 nm on the front side and optical grade polish on the back). The substrate was cleaned in base piranha, and the c-Si was etched to the final metasurface thickness ($h = 150$ nm) via reactive ion etching (RIE) employing CHF_3, SF_6, and O_2. The c-Si film thickness was checked with Filmetrics F20.

- After an O_2 plasma surface treatment a 50 nm thick layer of HSQ (hydrogen silsesquioxane) negative-tone resist was spin-coated and baked for 2 min at 180°C.

- The metasurface was patterned in the HSQ layer by exposure using a Raith Voyager e-beam lithography system (50 kV, dose 2300 $\mu C/cm^2$) and development in TMAH (Tetramethylammonium hydroxide) for 60 s at 50°C. As explained in Section 2.5 the pattern has to be aligned along the optical axis of sapphire during e-beam exposure.

- The pattern was then transferred into the c-Si by a two–step RIE (Reactive Ion Etching) process employing Cl_2, HBr, and O_2 (the etch rate and the parameters used are the same as in Section 2.5). Next, the sample was cleaned in acid piranha for 10 minutes.

- After another O_2 plasma surface treatment, a $\simeq$ 100 nm thick layer of SiO_2 solgel (Nanoglass E1200 3:1 in 1-Butanol) [13] was spin-coated and baked for 3 min at

45°C and 2 min at 200°C. This step is repeated three times to reach a thickness of ≃ 375 nm. The latter is obtained by combining an optical thickness measurement (using Filmetrics F20) and a profilometer (KLA – Tencor P7) height scan across the edge of the patterned area (see Fig. 4.7a). Indeed, the degree of planarization obtained with this technique is not global but rather local. As schematically shown in Fig. 4.7b, the solgel thickness h_1 is constant on the bare Al_2O_3 substrate but increases across the edge of the patterned area by Δh. Hence, it possible to measure h_1 optically with the F20 tool and to extract Δh from the height profile in Fig. 4.7c.

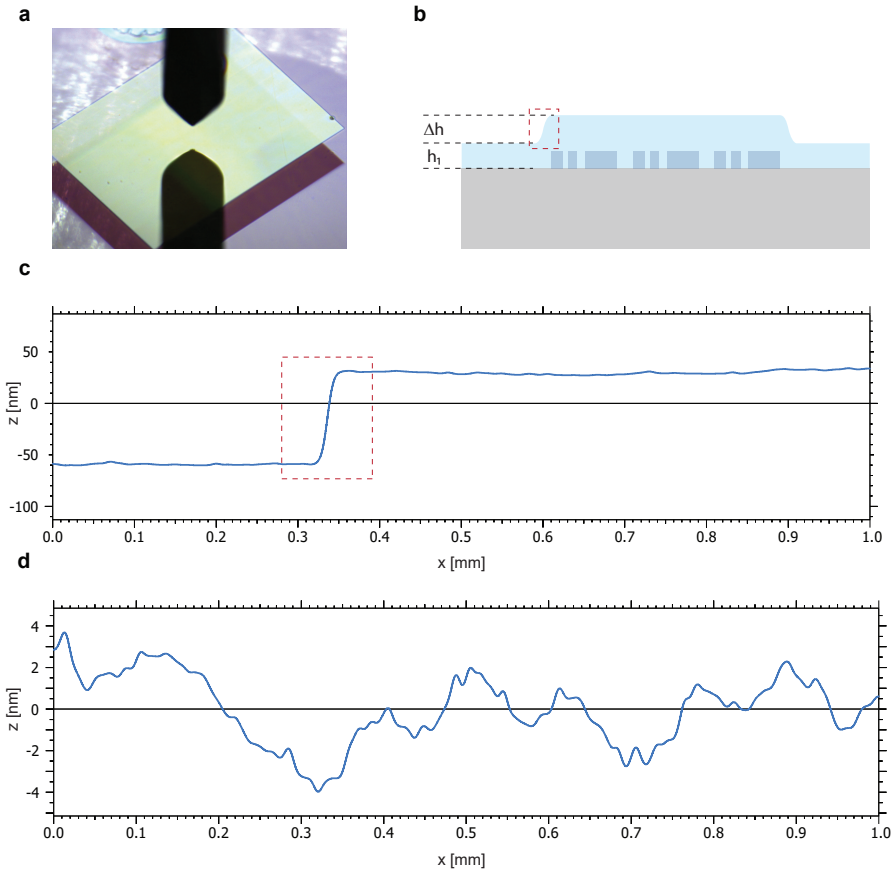

Figure 4.7: **a** Optical image of patterned metagrating area (2 × 1.5 mm) after solgel planarization. **b** Solgel thickness variation due to local planarization. **c-d** Profilometer height profile scans across the edge of the patterned area (c) and on top of it (d).

- The sample was annealed at 800°C for 10 min. The temperature is ramped up from room temperature to 800°C in 8 min and, after 10 min, ramped down again to room temperature in 5 min. This step serves the purpose of increasing the refrac-

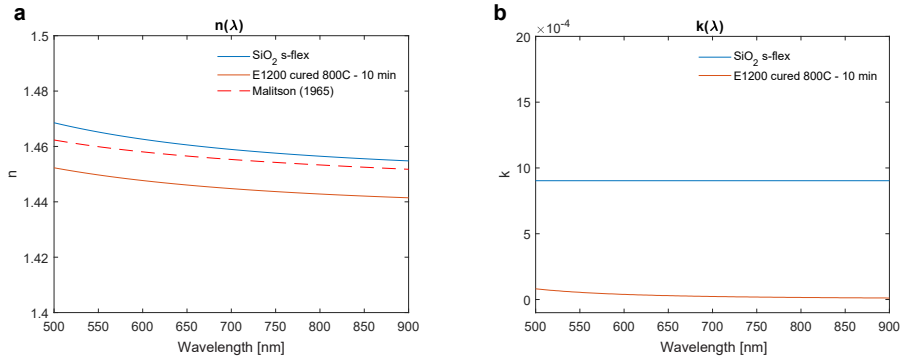

Figure 4.8: Real (a) and imaginary part of the refractive indices of annealed solgel, sputtered SiO_2, and literature values from Ref. [14]

tive index of solgel to values closer to the literature ones used in simulation [14]. Figure 4.8 shows the experimental refractive index values measured via spectroscopic ellipsometry. The SiO_2 thickness is then checked again with Filmetrics F20 and profilometer (KLA – Tencor P7).

- The SiO_2 thickness needed to reach 638 nm is sputtered with Polyteknik Flextura M506 S using a Si source. A clean Si reference sample is also added to the run to check the sputtered SiO_2 thickness and refractive index (see Fig. 4.8). The surface roughness of the final spacer layer on top of the metagrating is evaluated via profilometer height scans (see Fig. 4.7c) and is in the range $0.7 < R_q < 1.6$ nm.

- A 3-aminopropyl trimethoxysilane (APTMS) adhesion monolayer is chemically deposited on the sample [15].

- A 15 nm thick Au layer is evaporated with Polyteknik Flextura M508 E e-beam evaporator. A clean quartz reference sample is also added to the run to check the evaporated Au thickness via transmittance measurements.

4.2.2. CHARACTERIZATION

In this section the sample fabricated following the procedure just described is characterized structurally and optically. As shown in Fig. 4.9, the fabricated structures after the Si reactive ion etching step are uniform and smooth over a large area. Next, it is important to compare the optimized unit cell to the experimental one. Figure 4.10a shows that the etched unit cell follows very closely the optimized contour (red dashed lines in Fig. 4.10a and Fig. 4.3a-b). To corroborate this feature, the transmittance of normal incident light to the 0^{th} diffraction order was measured and compared to its simulated counterpart. In the simulation, the optimized structure described above was used. The transmittance spectrum was acquired over a broad wavelength range ($\lambda_0 = 500-800$ nm) to obtain maximum sensitivity in the comparison between experiment and simulation. Figure 4.10b demonstrates strong agreement between simulated and measured optical

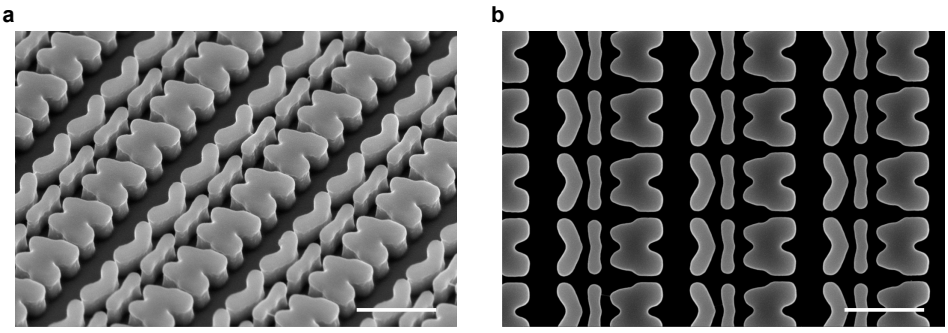

Figure 4.9: **a** Tilted scanning electron microscopy (SEM) image of the patterned Si metagrating. **b** Top-view SEM image of the same patterned area. The scalebar is 500 nm for both panels.

spectra, further confirming the suitability of the combined EBL+RIE process to fabricate precisely tailored metagratings for analog optical computing in the visible spectral range.

Next, the cross-section in Fig. 4.10c shows how the SiO_2 spacer conformally embeds the metagrating with no detectable air inclusions, creating a smooth planar top surface. The final thickness of the layer with the embedded metagrating amounts to 638 nm. Again, the transmittance is measured at this step, once more experimentally reproducing the key features present in the simulated ideal spectrum (see Fig. 4.10d). The small discrepancies between experiment and simulation in Fig. 4.10b-d can be attributed to minor fabrication imperfections, such as a slight difference in the SiO_2 refractive index between experiment and simulation, and non-perfectly straight Si etching. The data in Fig. 4.10b-d was collected using the integrating sphere setup described in Section 2.6.1. The sample was illuminated with collimated, TE-polarized, white light from a SuperK EXTREME/FIANIUM supercontinuum laser. The 0^{th} order transmitted light was collected by an integrating sphere and sent to the spectrometer through a multimode fiber. Finally, the Au film evaporation concludes the fabrication, providing the metastructure with a semi-transparent mirror, and hence the required feedback system.

The analog solution of Eq.(4.5) is built up inside the spacer layer in the form of a collection of complex wave amplitudes. These values are hard to retrieve in a far-field experiment, hence we compare the spectroscopic power measurements to simulations of the optimized structure in order to verify the correct operation of our metasurface. Figure 4.11 shows the measured transmittance spectra of the fully fabricated metastructure relating to each S-parameter belonging to S_{2T} or, equivalently, the fraction of transmitted light going into each diffraction channel when the metastructure is illuminated through each input channel above the mirror. Specifically, each sub-panel shows the amplitudes squared of the elements belonging to each column of S_{2T}. Note that the input and output angles are changing with the wavelength of illumination according to the grating equation. In order to collect this data, the setup in in Fig. 4.12 was used. The illumination is provided by the same SuperK EXTREME/FIANIUM supercontinuum white-light laser that is monochromated (2 nm bandwidth) by a Laser Line Tunable Filter (LLTF) from Photon Etc. The setup consists of two concentric rotating stages. The

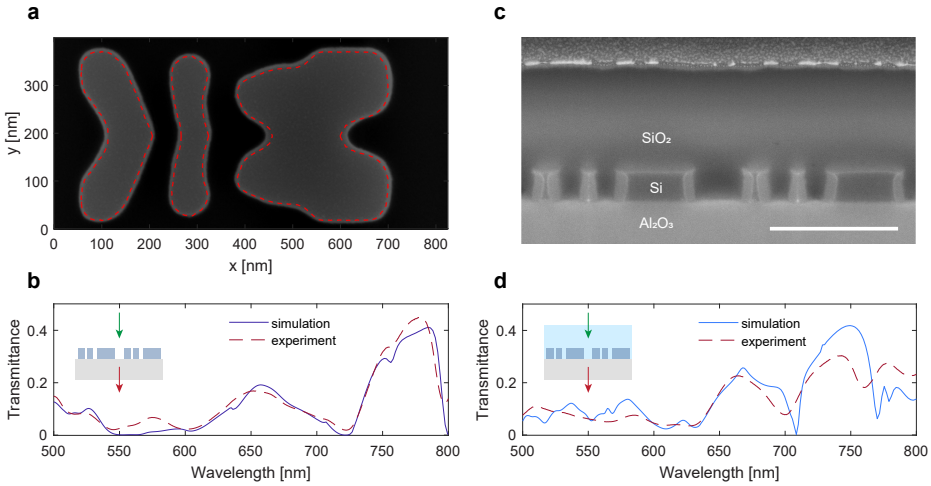

Figure 4.10: **a** Zoomed-in top-view SEM image of a single unit cell compared with the desired optimized contour (red dashed line). **b** Experimental (dashed red) and simulated (dark blue) transmittance spectra of the metagrating after the Si etch step (i.e. without silica spacer and top mirror). The sample was illuminated under normal incidence and the transmitted 0^{th}-order diffraction intensity is collected (inset) as a function of incident wavelength. **c** SEM image of a focused-ion-beam-milled cross-section of the same metagrating embedded in a SiO_2 spacer. **d** Experimental (dashed red) and simulated (blue) transmittance spectra of the metagrating after the SiO_2 planarization step, the scale bar is 500 nm. The input polarization is TE for panels b-d.

sample is mounted on the inner rotating stage (Rot. stage 1 in Fig. 4.12) while an optical power meter (Power meter PM100USB with Photodiode Power Sensor S121C from Thorlabs) is mounted on the outer rotating stage (Rot. stage 2). This configuration allows independent control of θ_0 and θ_T. Light is polarized before impinging on the sample. Each sub-panel in Fig. 4.11 also shows the simulated spectra of the designed ideal metastructure in Fig. 4.5a that gives the solutions shown in Fig. 4.5b. The agreement over a broad wavelength range between simulation and experiment is clear: for each matrix element, the spectral features present in the simulation are reproduced experimentally. Other small discrepancies between experiment and simulation are attributed to minor fabrication imperfections, as described above, that do not hinder the concept of solving an integral equation with the proposed optical-analog scheme. To prove this, Fig. 4.13 shows the robustness of the metagrating based integral equation solver concept against fabrication imperfections. First, the experimental refractive indices of the annealed silica sol-gel and sputtered SiO_2, measured with ellipsometry, are included in the simulations. Next, several unit cell contours are generated from the distribution in Fig. 4.3a by sweeping the binarization threshold (see Fig. 4.13a); this type of fabrication imperfection may arise from unintended resists over- or underexposure. The transmittance corresponding to these slightly eroded and expanded unit cells is simulated and compared to the experimental transmittance data showed in Fig. 4.10b-d. Both for the bare metasurface and for the metasurface including the SiO_2 spacer, the experimental

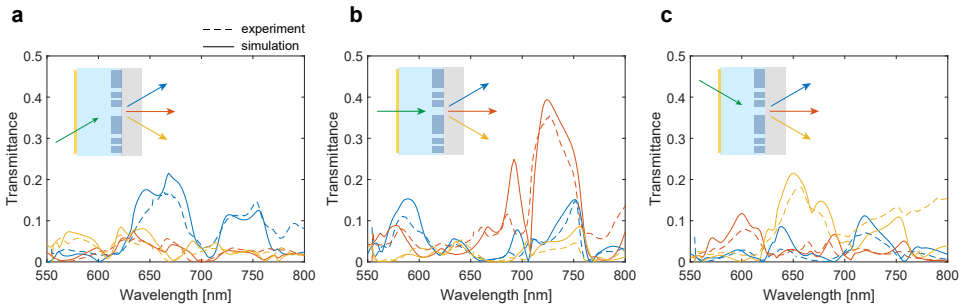

Figure 4.11: **a-c** Experimental (dashed lines) and simulated (solid lines) transmittance spectra of the completed metastructure. Insets: schematic visualization of the metastructure indicating the exciting input port (green arrows) representing orthogonal unit vectors, and the three output ports (yellow, orange, and blue matching the corresponding spectra). The input polarization is TE for all panels.

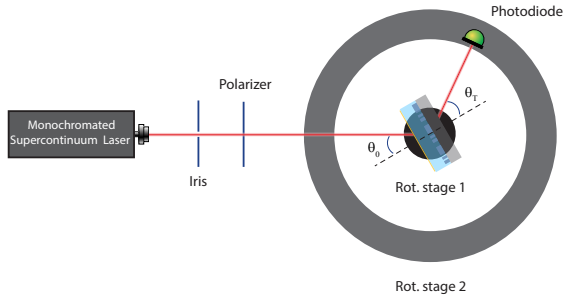

Figure 4.12: Schematics of the setup used to collect the data shown in Fig. 4.11.

data is bounded by the transmittance of an expanded unit cell (level 2.2) and that of an eroded one (level 3.2) being remarkably close to the data of a slightly eroded unit cell (level 2.8). Nonetheless, it is crucial to evaluate the impact of the described imperfections on the performance of the integral solver. For each unit cell the S-matrix was simulated and S_{1R} plotted in Fig. 4.13d-f. The consequence of the mentioned shape distortion is a shift in the operational wavelength. In fact, the minimum distance between the prescribed S-parameters and the simulated ones (i.e. the minimum FOM) is achieved at a different wavelength, which is blue-shifted for the eroded pattern and red-shifted for the expanded counterpart. Also, the FOM value at the minimum depends on the unit cell shape and this has a direct impact on the accuracy of the solution provided by the entire metastructure including the feedback semi-transparent mirror. Figure 4.13 g-i shows how the solution obtained with the three different contours compares to the ideal one. The overall trend is well represented for the different input vectors $(1,0,0)^\mathsf{T}$, $(0,1,0)^\mathsf{T}$, $(0,0,1)^\mathsf{T}$, both in real and imaginary part even for non-ideal designs. Similar results are obtained upon including additional nonidealities such as sloped sidewalls introducing only a small shift in wavelength and a small accuracy loss.

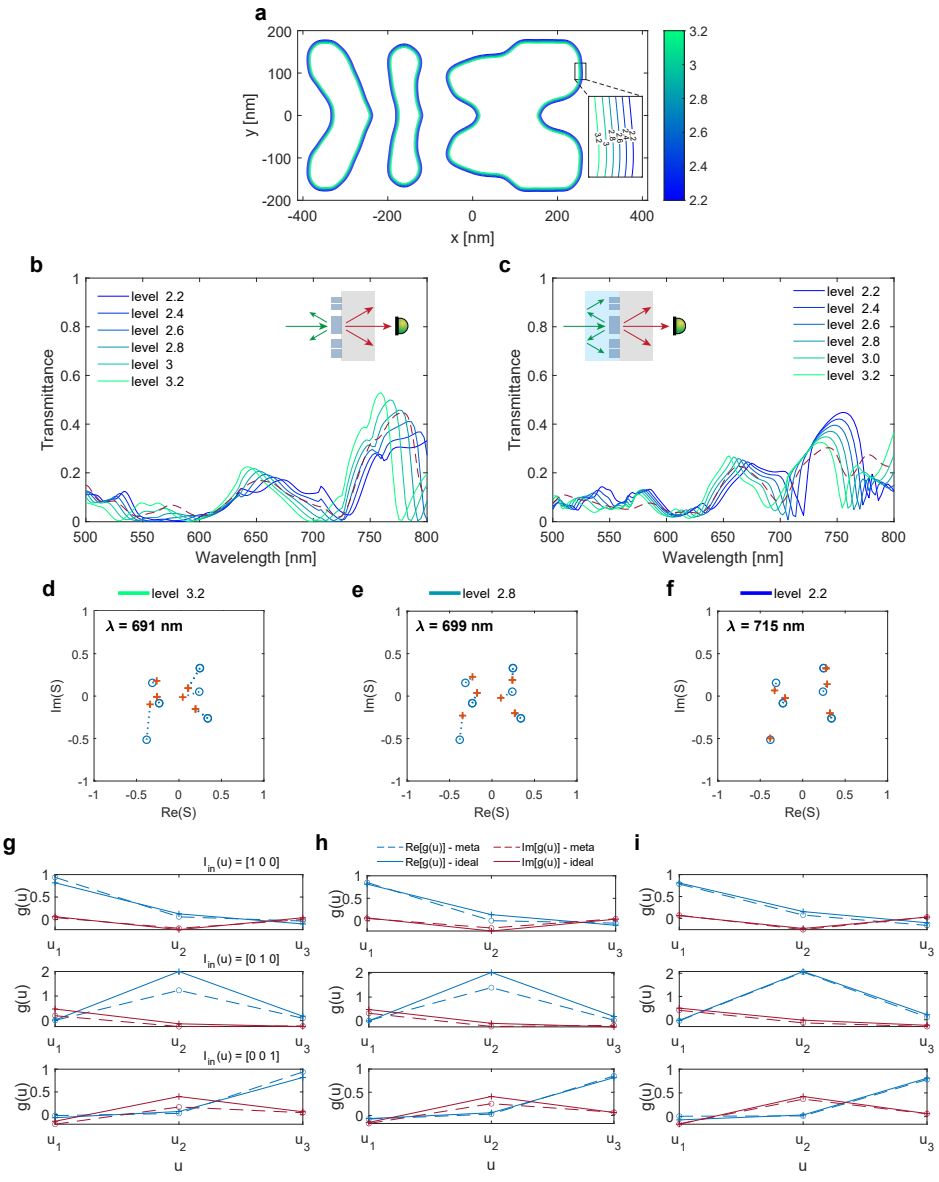

Figure 4.13: **a** Expanded and eroded contours generated from the optimal unit cell refractive index distribution in Fig. S2a. **b** Simulated (solid lines) transmittance spectra (0^{th} transmitted diffraction order) of the metagrating for the contours shown in a. The solid red dashed line is the experimental transmittance also shown in Fig. 4c of the main text. **c** Same as panel b but including the SiO_2 spacer layer. **d–f** Simulated S_{1R} s-matrix sub block for three different unit cell contours (levels 2.2, 2.8, 3.2). **g–i** Comparison between the analog solution obtained from the simulated metastructure transmission and the ideal solution for the same three contours as in d-f and for the three different orthogonal input vectors.

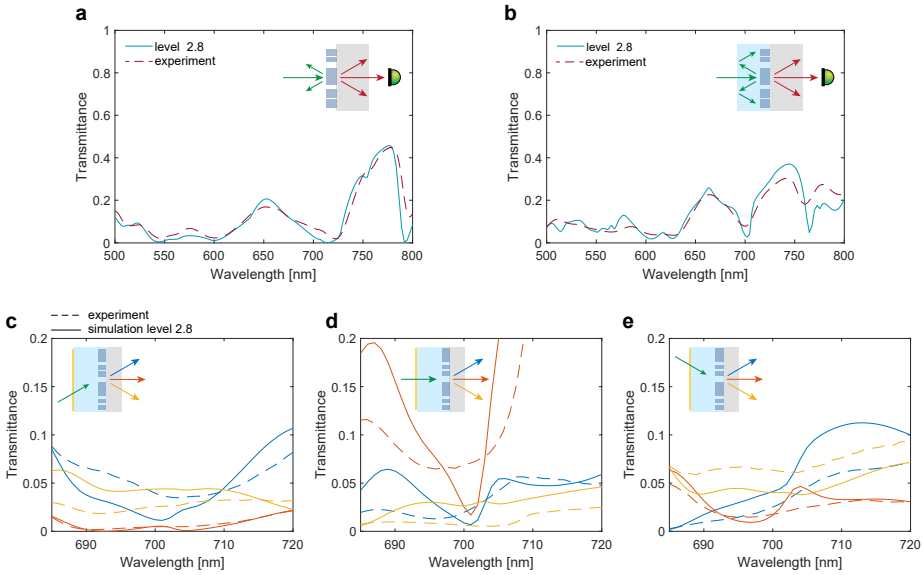

Figure 4.14: **a** Simulated (solid lines) transmittance spectra (0^{th} transmitted diffraction order) of the metagrating for the contour level 2.8. The red dashed line is the experimental transmittance also shown in Fig. 4c of the main text. **b** Same as panel a but including the SiO_2 spacer layer. **c–e** Experimental (dashed lines) and simulated (solid lines - contour level 2.8) transmittance spectra of the completed metastructure. Insets: schematic visualization of the metastructure indicating the exciting input port (green arrows) representing orthogonal unit vectors, and the three output ports (yellow, orange, and blue matching the corresponding spectra).

Next, we can use this fabrication tolerances analysis to benchmark our experimental data and give an estimate of the solution experimentally provided by the metastructure. In fact, it is possible to treat the contour level (i.e. binarization threshold) as a fitting parameter to find the closest matching simulation to the experimental data. Figure 4.14a-b shows the simulated 0^{th}–order transmittance spectra for a slightly eroded unit cell (level 2.8) and its experimental counterpart for the bare metagrating and including the SiO_2 spacer layer. The agreement over a broad wavelength range between simulation and experiment is very good.

Figure 4.14c-e compares the experimental and simulated (contour level 2.8) transmittance spectra of the fully fabricated metastructure relating to each S-parameter belonging to $|S_{2T}|^2$ in a narrower spectral range around the designed wavelength of operation. Again, the experimental spectra reproduce the key features present in the simulated counterpart with rather small deviations. However, in order to validate the use of the simulation with contour level 2.8 as the estimated experimental solution, it is important to assess the impact of such deviations. To do so, we use the generated expanded and eroded designs (contour levels from 2.2 to 3.2) to define a confidence region that bounds our experimental transmittance spectra. Figure 4.15 shows that, even though the experimental data does not correspond perfectly to one specific simulation, at $\lambda = 699$ nm the transmittance lies in the range defined by the simulations with the only exception of the matrix element S_{61} that differs from it by less than 1%. Hence, it

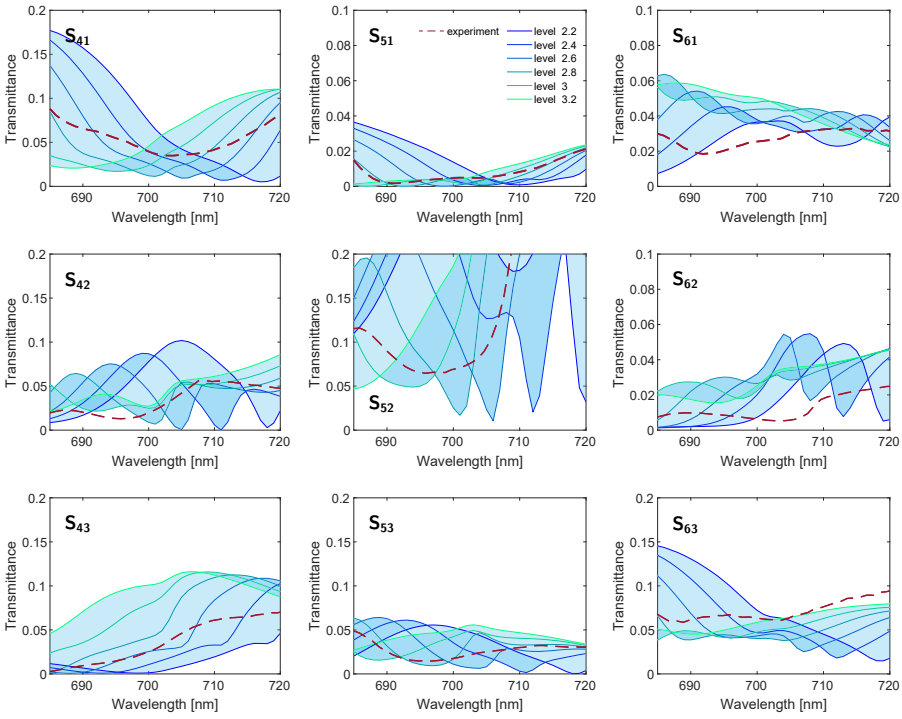

Figure 4.15: **a** Experimental (dashed lines) and simulated (solid lines - contour levels 2.8–3.2) transmittance spectra of the completed metastructure. Each panel corresponds to one element of the matrix S_{2T}.

is possible to select the solution corresponding to contour level 2.8 attributing to it an uncertainty defined by the response of all the other contours at the same wavelength $\lambda = 699$ nm. Figure 4.16 shows the final estimated experimental solution equipped with the latter uncertainty region. The metasurface-based analog solution and the ideal solution show good agreement and similar trends for all the inputs, both in terms of the real and imaginary parts. Furthermore, most of the values corresponding to the ideal solution are compatible with the estimated experimental solution (i.e. lie in its uncertainty region).

While fabrication imperfections have certainly an impact on the overall accuracy, they do not hinder the concept of solving an integral equation with the proposed optical-analog scheme. Moreover, we showed how to retrieve via simulations the solution provided by the metastructure via measuring its response in amplitude in a broad spectral range.

4.3. CONCLUSION

In conclusion, we have presented a Si-based optical metastructure that solves Fredholm integral equations of the second kind in a fully analog fashion at optical frequencies. First, we stated the mathematical problem in terms of the Neumann series successive

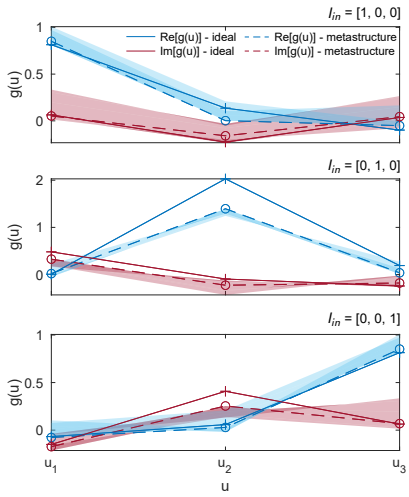

Figure 4.16: Estimated experimental analog solution (real and imaginary parts) of the integral equation (dashed line) compared to the ideal theoretical solution, for the three orthogonal input vectors $(1,0,0)^\mathsf{T}$, $(0,1,0)^\mathsf{T}$, $(0,0,1)^\mathsf{T}$. The wavelength of operation in this simulation is $\lambda = 699$ nm. The shaded regions indicate the uncertainty related to the solution and are generated by the response of several simulations with expanded and eroded designs.

approximation. Next, we discussed the analogy between the integral equation solving and the behavior of an optimized periodic metagrating coupled to a feedback system. At the foundations of this mapping lies the possibility of designing the S-matrix of a periodic structure by setting its periodicity (i.e., the number of input/output modes and hence the dimension of the S-matrix) and optimizing its unit cell (i.e., optimize the coupling of light into the defined diffraction modes in amplitude and phase). Consequently, we show how the designed metastructure effectively solves the problem of interest and compared the metasurface-based solution to the ideal solution. Electron beam lithography and reactive ion etching provide the deep subwavelength spatial resolution required to create a hardware representation of a predefined Kernel, with relatively small deviations between experiment and simulations. We optically characterized the output for different input signals showing good agreement with the ideal simulated response.

Our results demonstrate the possibility of solving complex mathematical problems and a generic matrix inversion at speeds that are far beyond those of the typical digital computing methods. Our solution converges (within 3% difference from the infinite sum) in less than ten passes, corresponding to a processing time of about 20 fs, five orders of magnitude faster than the clock speed of a conventional processor. Operation in the visible spectral range in combination with deep-subwavelength fabrication resolution creates metastructures that are sub-micron thick. This represents a very high degree of circuit integration given the complexity of the mathematical operation performed in this small volume.

Further extensions of this work may explore non-symmetric kernels in a transmissive setup. Also, a similar scheme could be used to estimate the eigenvalues of an inte-

gral operator (a matrix in the discretized form) by exploiting, for example, spontaneous emission of active materials. In fact, this would correspond to the solution of the homogeneous equation corresponding to the Fredholm integral equation of the second kind under study. Moreover, it is possible to scale up the dimensionality of the problem, increasing the number of input/output ports by using more diffraction orders or by encoding information in the polarization state of light. The main challenge in either of these extensions lies in one's ability to accurately fabricate unit cells of higher resolution and smaller feature size required to independently control more degrees of freedom. Of course, a larger number of diffraction orders would imply a larger periodicity and unit cell, partially alleviating this burden. One key advantage of our scheme is the possibility of integrating many designs within a unique feedback system, thus enabling parallelization whenever this is compatible with the problem under study.

Future applications of these concepts could include nonlinear materials within the feedback system (e.g., replacing the SiO_2 spacer layer) to explore nonlinear mathematical problems. Additionally, nonlinearity could also be applied after processing the information via linear operations. Hence, a dedicated external nonlinear device could be designed to process the outputs of our metastructure.

Finally, switchable metagratings (e.g. using phase change materials or mechanical modulation) could be envisioned to dynamically tune the encoded mathematical operation, paving the way for all-optical reconfigurable computing circuitry solving problems of further enhanced complexity.

REFERENCES

[1] C. Cohen-Tannoudji, B. Diu, and F. Laloe, *An elementary approach to the quantum theory of scattering by a potential,* in *Quantum Mechanics*, Vol. 2 (Wiley).

[2] G. B. Arfken, H. J. Weber, and F. E. Harris, *Mathematical Methods for Physicists* (Elsevier, 2013).

[3] N. Mohammadi Estakhri, B. Edwards, and N. Engheta, *Inverse-designed metastructures that solve equations,* Science **363**, 1333 (2019).

[4] M. Camacho, B. Edwards, and N. Engheta, *A single inverse-designed photonic structure that performs parallel computing,* Nature Communications **12**, 1466 (2021).

[5] D. Sell, J. Yang, S. Doshay, R. Yang, and J. A. Fan, *Large-Angle, Multifunctional Metagratings Based on Freeform Multimode Geometries,* Nano Letters **17**, 3752 (2017).

[6] T. W. Hughes, M. Minkov, I. A. D. Williamson, and S. Fan, *Adjoint Method and Inverse Design for Nonlinear Nanophotonic Devices,* ACS Photonics **5**, 4781 (2018), 1811.01255 .

[7] A. Y. Piggott, J. Petykiewicz, L. Su, and J. Vučković, *Fabrication-constrained nanophotonic inverse design,* Scientific Reports **7**, 1786 (2017).

[8] A. Y. Piggott, J. Lu, K. G. Lagoudakis, J. Petykiewicz, T. M. Babinec, and J. Vucković, *Inverse design and demonstration of a compact and broadband on-chip wavelength demultiplexer,* Nature Photonics **9**, 374 (2015).

[9] S. Molesky, Z. Lin, A. Y. Piggott, W. Jin, J. Vucković, and A. W. Rodriguez, *Inverse design in nanophotonics,* Nature Photonics **12**, 659 (2018).

[10] C. M. Lalau-Keraly, S. Bhargava, O. D. Miller, and E. Yablonovitch, *Adjoint shape optimization applied to electromagnetic design,* Optics Express **21**, 21693 (2013).

[11] G. Rosenblatt, B. Simkhovich, G. Bartal, and M. Orenstein, *Nonmodal Plasmonics: Controlling the Forced Optical Response of Nanostructures,* Physical Review X **10**, 011071 (2020).

[12] L. Li, *Bremmer series, R-matrix propagation algorithm, and numerical modeling of diffraction gratings,* Journal of the Optical Society of America A **11**, 2829 (1994).

[13] M. A. Verschuuren, M. W. Knight, M. Megens, and A. Polman, *Nanoscale spatial limitations of large-area substrate conformal imprint lithography,* Nanotechnology **30**, 345301 (2019).

[14] I. H. Malitson, *Interspecimen comparison of the refractive index of fused silica∗,†,* J. Opt. Soc. Am. **55**, 1205 (1965).

[15] J. Sukham, O. Takayama, A. V. Lavrinenko, and R. Malureanu, *High-Quality Ultrathin Gold Layers with an APTMS Adhesion for Optimal Performance of Surface Plasmon Polariton-Based Devices,* ACS Applied Materials & Interfaces **9**, 25049 (2017).

5

NANOPHOTONIC LIGHT MANAGEMENT

In this chapter, we present a nanophotonic light trapping scheme in the near-infrared wavelength range designed to increase the efficiency of high-performance two-terminal GaInP/GaAs/Si triple-junction solar cells.

A silver diffractive back-reflector at the bottom of the cell is designed to steer incoming light to diffraction angles for which total internal reflection occurs. The structural parameters are optimized and the physics behind the suppressed reflectance to 0^{th}*–order and simultaneous low parasitic absorption is explained with a simple yet insightful interference model. We numerically and experimentally assess the potential of the optimal design on the performance of single-junction Si solar cells, highlighting a short-circuit current increase over a planar back–reflector and over the design that is currently featured in the record cell.*

Finally, nanopatterned back-reflectors are fabricated on triple–junction solar cells via Substrate Conformal Imprint Lithography (SCIL) and characterized optically and electronically, demonstrating a power conversion efficiency improvement of $+1.8\%$ *over the planar reference. Overall, the results show the possibility of achieving efficiencies above the current record for III-V/Si triple-junction cells. Moreover, the same concepts could be flexibly applied to other Si-based tandem solar cells.*

NEW solar power conversion architectures are increasingly important to achieve large-scale sustainable power generation to satisfy the growing energy needs of our society [1]. In this regard, research focused on photovoltaics (PV) has made huge progress since the first practical solar cell was demonstrated at Bell Laboratories in 1954 [2]. Indeed, many types of solar cells have reached high efficiencies yet there is still some margin to achieve their full potential and thus reach the thermodynamic detailed-balance limit [3]. This can be traced back to incomplete light absorption, implying a loss in short-circuit current J_{sc}, as well as poor carrier management (e.g. carrier recombination, parasitic resistance, etc.) resulting in reduced open-circuit voltage V_{oc} or fill factor FF [4, 5]. Regarding light management, in particular, the majority of the current record cells still rely on single or double pass absorption and exploit relatively thick absorber layers (> 100 μm for Si and > 1 μm for thin-film architectures like GaAs, CdTe, etc.).

In this context, the field of nanophotonic light management in PV has emerged and it is well established in the broader area of nanophotonic research. In fact, smarter light managing strategies can lead to higher efficiencies but also to a dramatic reduction of the absorber thickness. This latter point, in turn, further implies numerous benefits:

- reducing material consumption has a direct impact on the overall cost. This is markedly important for scarce elements (e.g. Te, In, etc.),
- shorter deposition times directly imply higher production throughput and make low-cost CVD processes appealing for industry,
- thin absorbers can potentially enable new flexible form factors leading to more facile system integration into wearable technologies and vehicles,
- in space applications, reduced mass and increased radiation resilience are key advantages of thin-film PV,
- when the cell thickness becomes comparable to the carrier diffusion length, charge extraction is more efficient and less susceptible to bulk recombination.

Light management strategies in PV aim to address two main challenges. First, a source of optical losses in a solar cell is reflection off its surface. This is typically solved via micron-sized textured top surfaces or by interference coatings. Nonetheless, the former approach is not applicable to thin PV due to the texture dimensions exceeding the cell thickness, while the latter is typically optimized for a relatively narrow angle of incidence range. Second, once light reaches the absorber material it has to be trapped in order to be completely harvested. This is a particularly crucial task in indirect band–gap semiconductors where the absorption coefficient is relatively low.

Several nanophotonic strategies can be applied to tackle this latter challenge [6–8]. In thin-film PV, nanopatterned surfaces can be designed to couple incident light into waveguide modes inside the absorber [9–11]. In thicker cells, when standard texturing is not a viable option, diffraction gratings can be used to steer light at angles at which total internal reflection (TIR) is occurring at the top interface [12].

In the following, we will focus on light trapping applied to multi-junction solar cells. With single-junction Si solar cell reaching power conversion efficiencies [13] close to the theoretical limit [14, 15], efficiency improvement can still be obtained by combining

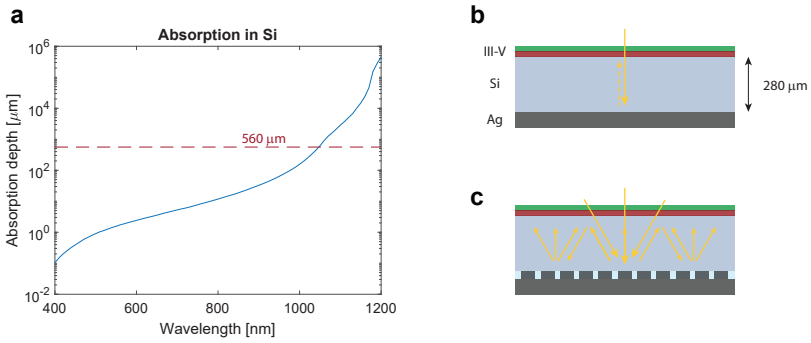

Figure 5.1: **a** Silicon absorption depth as a function of wavelength. The intersection between the red dashed line and the absorption curve indicates the wavelength beyond which light harvesting is incomplete in a fully planar cell. **b-c** Schematics illustrating the effect of a patterned back–reflector to enhance light trapping in a III-V/Si triple-junction solar cell.

multiple semiconductor materials with different band-gaps in a multi-junction configuration so that light is absorbed more efficiently over a broad range in the solar spectrum, and a smaller fraction of the photon energy is lost due to thermalization [16].

In particular, series-connected two-terminal devices, where sub-cells are monolithically stacked, are simpler (compared to spectral splitting configurations and four terminal devices) and more practical when it comes to implementation into photovoltaic modules. Taking advantage of the maturity of Si solar cell technology, researchers have been exploring the best high band-gap partners that can be coupled to state-of-the-art Si cells. Among the potentially compatible stacked materials, two materials are investigated the most: III-V semiconductors and perovskites. Organic-inorganic metal halide perovskite solar cells are one of the most rapidly advancing technology and among the most researched materials, recently reaching 29.8% [17, 18] in combination with Si. However, stability and reproducibility are important open questions.

On the other hand, a novel approach to combine a III-V top tandem cell (GaInP/GaAs) to a bottom Si cell via wafer bonding recently led to an overall efficiency of 35.9% [19]. One critical challenge affecting this type of cell is the weak absorption in the Si cell near the band gap (1000-1200 nm). In fact, in that wavelength range, the typical absorption length becomes larger than twice the cell thickness, as shown in Fig. 5.1a. Thus, part of the incoming solar light is able to escape from the front surface after being reflected at the bottom of the cell.

Furthermore, standard micro-texturing of the Si cell's backside is not compatible with this type of cell. The Si bottom cell employs the TOPCon (tunnel oxide passivated contact) technology developed at Fraunhofer ISE. This charge carrier-selective contact is based on an ultra-thin tunnel oxide in combination with a thin silicon layer and enables excellent charge carrier selectivity. The p-type TOPCon layer at the backside of the Si bottom cell provides the best passivation on a planar surface while carrier recombination is much higher on textured surfaces. This particular cell geometry thus poses a uniquely challenging scenario where conventional light trapping schemes are inapplicable. Therefore, it is thus of value to assess how ultra-thin nanophotonic metasurface

designs can tackle this challenge and selectively enhance the optical absorption in the 1000-1200 nm spectral range.

Here, we leverage our insights in optical metasurfaces to design a nano-structured back-reflector that steers incoming light to angles at which total internal reflection at the cell's top surface can occur. Specifically, we optimize a hexagonal array of Ag nano-disks and show how pitch, radius, and height of the individual scatterer control the amount of power that is distributed into the different diffraction orders. We present an intuitive interference model to explain the physical mechanism governing light steering at the back-reflector. Next, the impact of the optimized design on the absorption in a thick Si slab is evaluated, highlighting an increase over a planar back-reflector and over the design that is now featured in the current III-V/Si triple-junction record cell [19]. Finally, we demonstrate experimentally, first on Si single–junction cells and afterwards on full two–terminal triple–junction cells, improved power conversion efficiency (+1.8%), showing the benefits of the proposed light trapping scheme.

5.1. THEORY AND DESIGN

In order to maximize light trapping in the Si bottom cell, we optimize the periodicity p of the hexagonal array acting as the back-reflector, along with height h and radius r of the nano–disk constituting its unit cell. Specifically, the figure-of-merit of the minimization is the sum of parasitic absorption occurring in the metal and back-reflection to the 0^{th} diffraction order, FOM = Abs + $R0^{\text{th}}$ averaged in the bandwidth 1000-1200 nm. This, in turn, is equal to maximizing light intensity steered at an angle with the practical advantage of not having to take into account a changing number of diffraction channels for every simulation. Figure 5.2a schematically shows the design parameters that are optimized. To reduce the parameters' space explored by the optimization, the period is constrained to be $p_{\text{min}} < p < p_{\text{max}}$, where p_{min} is the minimum periodicity required to have diffraction in the entire bandwidth and p_{max} is the maximum periodicity for which the first diffraction orders are outside the escape cone ($\simeq 16.2°$ for the Si/air interface). The nano-disks' radius and height are constrained to practical values from the fabrication point of view. Employing a particle swarm optimization algorithm [20], the final set of retrieved optimal parameters is: $p = 534$ nm, $h = 240$ nm and $r = 171$ nm.

The corresponding spectra for parasitic absorption and reflectance back to the 0^{th} diffraction order are shown in Figure 5.2b. It is important to remark that reflection to the 0^{th}–order is almost completely canceled while no absorption peaks signaling plasmonic resonances are present in the entire bandwidth of interest. This, in turn, implies that $\simeq 92\%$ of the incoming light is reflected at an angle within the TIR range.

The distribution of reflected power to the different diffraction channels (averaged over the simulation wavelength range) is depicted in Fig. 5.2c for unpolarized light. Most of the light reaching the back-reflector at the bottom of the Si cell is reflected equally to 6 diffraction channels beyond the critical angle for the Si/air interface with a $\simeq 15.4\%$ efficiency for each channel. It is interesting to point out that, while the FOM is polarization independent the coupling efficiencies to the channels at an angle are not (see Fig. 5.2d-e). Indeed, at normal incidence and for a normally reflected wave (e.g. the 0^{th} diffraction order) the array is invariant under $\pi/3$ rotations. This implies that any in-plane polarization vector can be written as a linear combination of two basis vectors that span

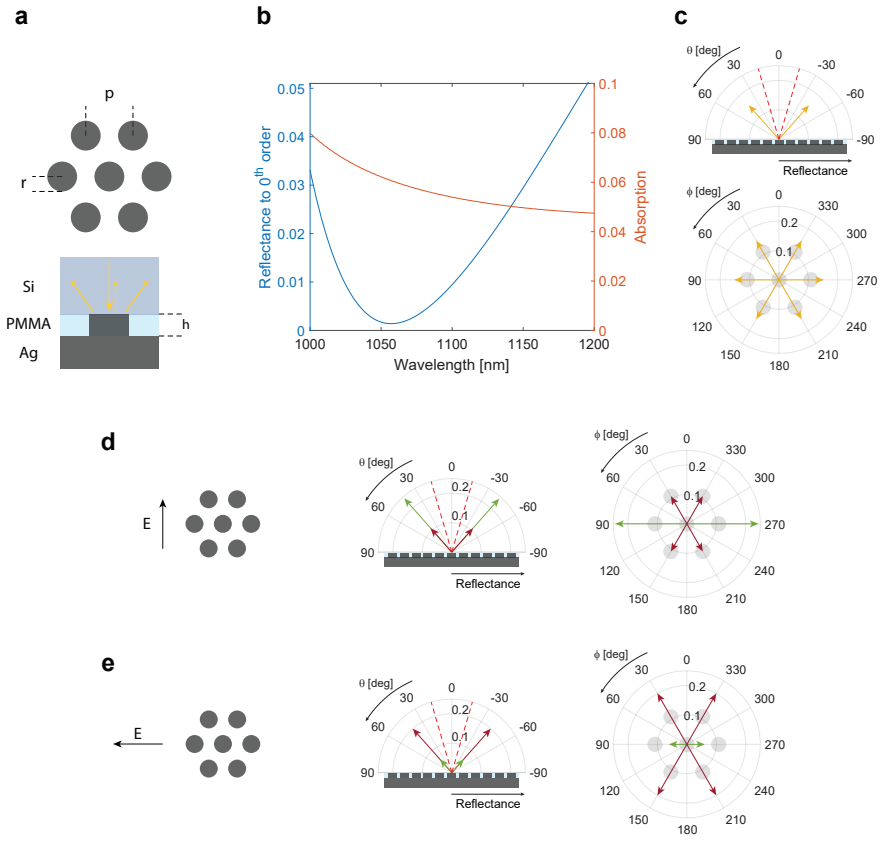

Figure 5.2: **a** Schematics of the back-reflector unit cell highlighting the relevant design parameters optimized. **b** Reflectance to the 0^{th} diffraction order (solid blue line) and parasitic absorption in the metal (solid orange line) as a function of wavelength. **c** Polar plots showing the fraction of incident power reflected (radial coordinate) to each diffraction channel (angular coordinates θ and ϕ) for unpolarized light averaged in the range 1000-1200 nm. **d-e** Polar plots showing the averaged fraction of incident power reflected to each diffraction channel for x- and y-polarized incident light.

the entire plane and for which the response is identical by symmetry (e.g. the primitive translation vectors of the hexagonal lattice that form an angle of $2\pi/3$ and are of equal length). On the other hand, for light impinging from an angle, and hence by reciprocity reflecting at an angle, the lattice would look distorted and not highly symmetric, therefore the response is polarization dependent.

To understand why it is possible to achieve such a low FOM and to unravel the mechanism behind the back-reflector operation, it is useful to analyze the parameter space beyond the optimum values. Figure 5.3a-b shows the reflectance to the 0^{th} diffraction order (a) and parasitic absorption (b), averaged in the range 1000-1200 nm, as a function of nano–disk height and periodicity if the lattice fill factor is kept constant ($p/r = 3$) and close to that of the optimal grating. As expected, if no diffraction channels are available

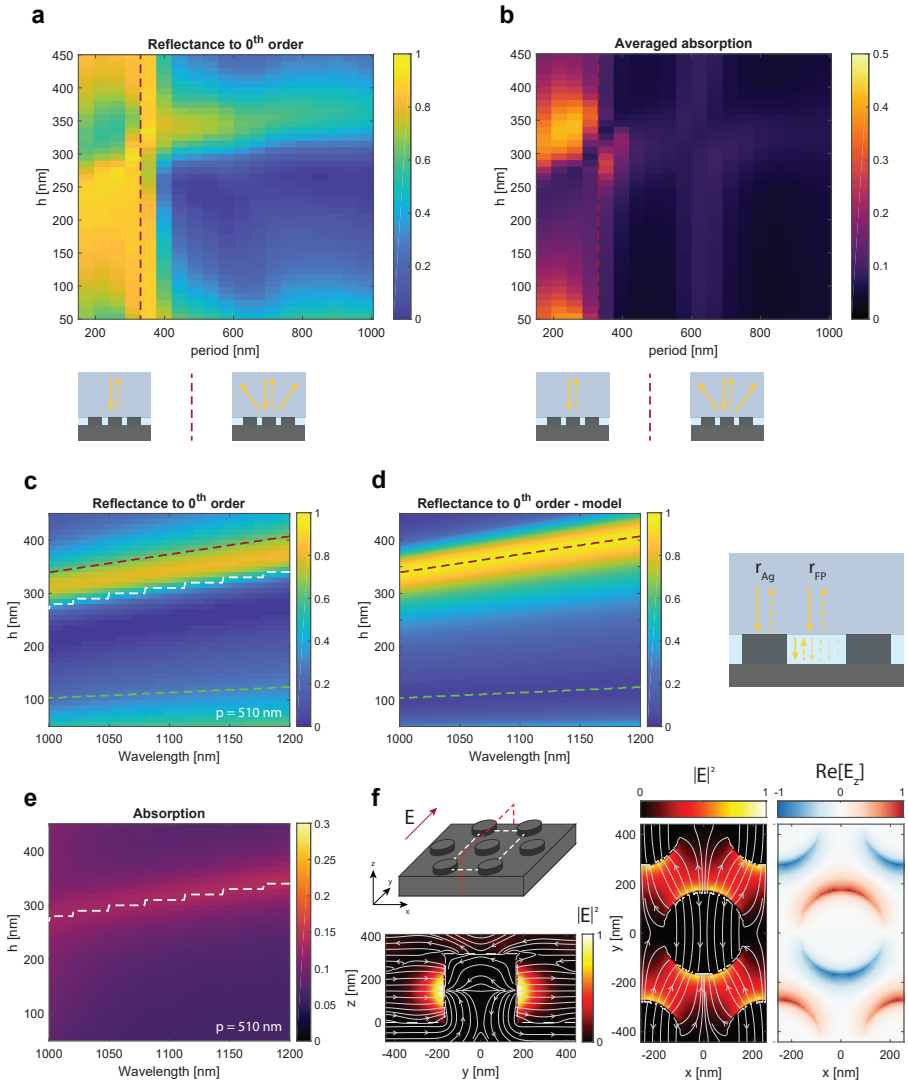

Figure 5.3: **a-b** Reflectance to the 0th diffraction order (a) and parasitic absorption in Ag (b), averaged in the range 1000–1200 nm, as a function of nanodisk height and periodicity if the lattice fill factor is kept constant ($p/r = 3$). The vertical red dashed lines indicate the onset of diffraction into Si, as schematically depicted in the insets. **c** Simulated and modeled (**d**) reflectance to the 0th diffraction order as a function of wavelength and nano–disk height for a fixed periodicity $p = 510$ nm. The red and green dashed lines indicate respectively the maxima and the minima locations in the modeled reflectance. The dashed white line corresponds to the location of the absorption maxima in (e). **e** Parasitic absorption in the metal as a function of wavelength and nano–disk height for a fixed periodicity $p = 510$ nm. The dashed white line marks the location of the absorption maxima. **f** Normalized electric field intensity and electric field z component profiles on the cross-cut planes highlighted in the schematics. The height of the nano-disk is $h = 320$ nm and the illumination wavelength is $\lambda = 1140$ nm. The xy cross–cut plane is taken at height $h = 160$ nm corresponding to the middle of the nano–disk. This cross-cut has a slight offset compared to the plane ($h \simeq 150$ nm) where the electric field z component is zero for a dipole oscillating in-plane.

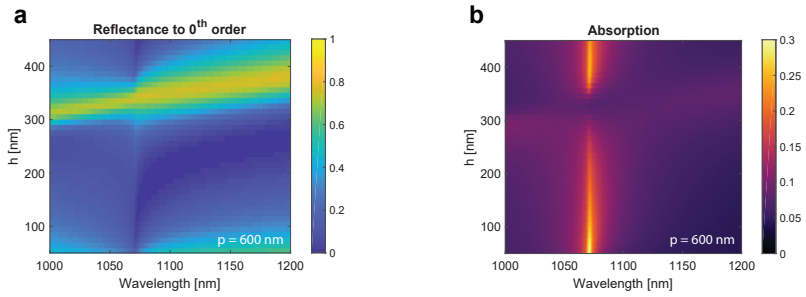

Figure 5.4: **a** Reflectance to the 0^{th} diffraction order as a function of wavelength and nano–disk height for a fixed periodicity $p = 600$ nm. **b** Parasitic absorption for the same parameter space.

the only way to have low reflectance is by having a high parasitic absorption. Indeed, for periodicities smaller than $p_{\text{min}} = \lambda_{\text{max}}/n_{\text{Si}} \simeq 336$ nm the minima in Fig. 5.3a correspond to maxima in Fig. 5.3b. However, when extra diffraction channels are opened in the superstrate it becomes possible to find regions in the parameter space where both reflectance and parasitic absorption are low.

Next, taking cross-cuts of the data in Fig. 5.3a-b at different periodicities it is possible to analyze the reflectance to 0^{th}–order and the parasitic absorption as a function of wavelength. Figure 5.3c-e shows such a cross-cut for $p = 510$ nm. Interestingly, the reflection to 0^{th}–order (panel c) can be approximated with a simple model assuming that light being reflected off the top of the nano–disks can interfere with light reflected off the PMMA and Ag interfaces. While the first contribution can be captured by the Fresnel coefficient for the single Si/Ag interface, the second should take into account multiple reflections at the PMMA/Si and PMMA/Ag interfaces and thus be modeled as a Fabry-Pérot interference, as schematically shown in Fig. 5.3d. Under these simple but insightful assumptions the resulting Fresnel reflection coefficient for the entire back-reflector is

$$r_{\text{tot}} = F\, r_{\text{Ag}} + (1 - F)\, r_{\text{FP}} \tag{5.1}$$

where $F = 2\pi r^2/\sqrt{3}p^2$ is the array fill factor, r_{Ag} is the Fresnel reflection coefficient for the Si/Ag interface and r_{FP} that of the PMMA etalon of height h sandwiched between Si and Ag (see Appendix A). Figure 5.3d shows the modeled reflectance $|r_{\text{tot}}|^2$ as a function of wavelength and height. The trends in Fig. 5.3c are well reproduced in Fig. 5.3d but it is easy to notice that the minima and maxima locations are not matching exactly (red and green dashed lines).

Indeed, this simple model does not take into account any plasmonic resonances in the Ag particle array. The presence of the latter is signaled by the peak in parasitic absorption in Fig. 5.3e. To further investigate its nature it is useful to inspect the near field profiles at the resonant wavelength. Figure 5.3f shows the electric field profiles corresponding to a nano–disks array of height $h = 320$ nm with an illumination wavelength $\lambda = 1140$ nm. Looking at the electric field intensity distribution at different planes (see inset) as well as its component along the z axis it can be seen that each nano–disk acts as plasmonic dipole antenna that interacts with its neighbors via near-field coupling.

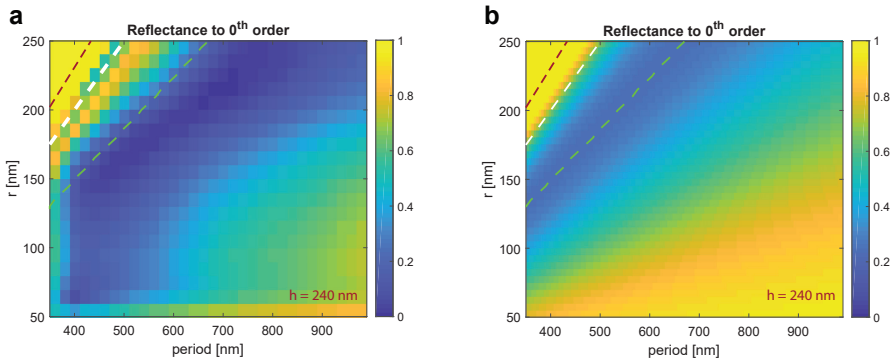

Figure 5.5: **a-b** Simulated (a) and modeled (b) reflectance to the 0^{th} diffraction order, averaged in the range 1000–1200 nm, as a function of nano–disk radius and periodicity for a fixed nano-disk height $h = 240$ nm. The white and red dashed lines indicate the fill factors values at which nano–disks are touching each other and fully covering the substrate respectively. The green dashed line indicates the minima in panel b.

This extra scattering pathway is interfering with non–resonantly reflected light, as described earlier and modeled with the coefficient r_{tot}. The interference between these *resonant* and *direct* pathways gives rise to a Fano lineshape where the resonance wavelength (white dashed line in Fig. 5.3c,e) is located between a maximum and a minimum in reflectance, as shown in Fig. 5.3c.

Next, referring back to Fig. 5.3b, it is worth highlighting a faint region around $p =$ 600 nm where parasitic absorption is higher. To further explore the physical mechanism behind this slight increase, Fig. 5.4a-b displays the reflectance to 0^{th}–order and the parasitic absorption as a function of wavelength for an array with $p = 600$ nm (and consequently $r = 200$ nm). The clearly visible sharp vertical feature in the reflectance spectra (panel a) corresponds to similarly sharp absorption peaks (panel b). This is due to the onset of higher diffraction modes that open up at grazing angles hence interacting more strongly with the nano-disks array and thereby inducing more losses. This phenomenon is known as Rayleigh anomaly (RA) [21–23].

To further test the applicability of Eq. (5.1), Fig. 5.5a-b demonstrates how the 0^{th}–order reflectance depends on the array periodicity and nano–disks radii and consequently on the fill factor F. Again, the general trend in reflectance is well captured by the simple model described above with a small discrepancy due to resonances that cause a slight mismatch in the minima locations (green dashed line) in panels (a) and (b). Understandably, there is an optimum fill factor to minimize reflection given the need of balancing the contributions from r_{Ag} and r_{FP}.

It is worth pointing out that, different from other light redirection strategies employing gratings [24, 25], in our case light is not steered at an angle by engineering the scattering of the single inclusion via resonances. On the contrary, sharp resonant modes should be avoided as they would result in severe parasitic loss. Our design redirects light at an angle by suppressing one of the available channels (0^{th}–order) essentially by destructive interference. Therefore, parasitic absorption in the metal can still be mitigated.

The analysis described so far concerns the metagrating only. Assessing the benefits

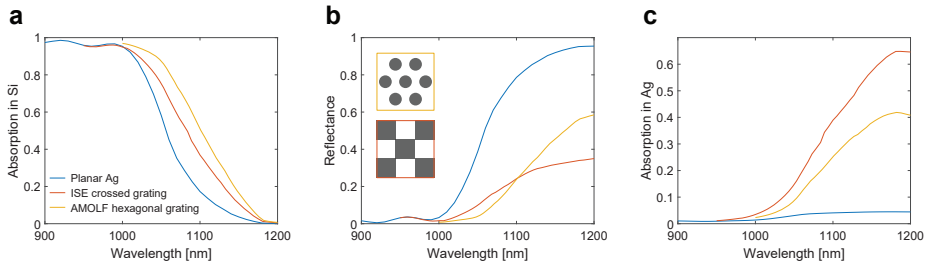

Figure 5.6: OPTOS calculated absorption in Si (**a**), reflectance (**b**), and parasitic absorption (**c**) spectra for the optimized design described above ("AMOLF hexagonal grating"), for the optimized design in Ref. [12] ("ISE crossed grating") and for a cell with a planar Ag back–reflector. The calculation assumes a double anti–reflection coating and a cell Si thickness of 280 μm. Inset: schematic of the two back-reflector geometries.

of this light trapping scheme on the entire solar cell level is a challenging task. Indeed, although in principle possible, simulating the entire cell via FDTD would be unfeasible from a computational point of view. Hence, the metagrating simulation/optimization and the calculation of the induced absorption enhancement within the Si bottom cell must be decoupled. One strategy to calculate optical properties of optically thick sheets with arbitrarily textured front- and rear surface is the OPTOS (Optical Properties of Textured Optical Sheets) formalism [26–28]. In this framework, the action of the textured surface, in the present case the optimized grating, is captured by a *redistribution matrix* where each element describes the fraction of light that is reflected from one diffraction channel to the other[1]. The redistribution matrix is calculated independently via FDTD by simulating the grating response when light is incident from each diffraction channel, for each wavelength in the bandwidth 1000–1200 nm and for both polarizations. The latter evaluation is rather time–consuming but has to be performed only once. Next, light propagation within the Si absorber is modeled with a *propagation matrix* that considers absorption according to Lambert–Beer's law. Thus, the optical properties of the entire stack (280 μm–thick Si absorber and Ag grating) can be calculated by a series of matrix multiplications similar to what is described in Chapter 4. The outcome of such calculation is shown in Fig. 5.6. Specifically, the optimized design described above ("AMOLF hexagonal grating") is compared to the grating geometry ("ISE crossed grating") [12] used in the current world record with a power conversion efficiency of η =35.9% and to a planar Ag back–reflector. Figure 5.6a demonstrates a clear enhancement in the absorption of both grating designs due to light trapping with a distinct advantage for the hexagonal design discussed here. Even though the total reflectance of the two designs is comparable, a lower parasitic absorption favors the AMOLF design.

Finally, it is important to remark that including OPTOS calculations in each FDTD optimization round would be the ideal way to maximize the cell performance as the relevant FOM is primarily the absorption in the thick Si bottom cell. However, this was not possible due to the heavy computational requirements for the computation of the redistribution matrix.

[1] In the scattering matrix formalism, the redistribution matrix is composed of the squared amplitudes of the s-parameters.

5.2. EXPERIMENT

In order to experimentally demonstrate the proposed nanophotonic light trapping structure, large-scale nanopatterns are fabricated on solar cells by Substrate Conformal Imprint Lithography (SCIL) [29, 30]. The silicon master used to mold the double-layer PDMS stamp was made at AMOLF by means of EBL and RIE. It consists of a 2.5 × 2.5 cm array of holes with the optimized periodicity and radius described above and a depth of about 100 nm which is optimal for solgel imprinting and PDMS demolding. Silicon bottom cells and full triple–junction cells are fabricated at Fraunhofer ISE with a planar Ag back-reflector and then characterized. Next, the planar Ag is peeled off mechanically, the front-side is protected with AZ520D resist and the cells are diced (2.1 × 2.1 cm) and shipped to AMOLF for patterning. In the following, the detailed fabrication procedure is explained step by step.

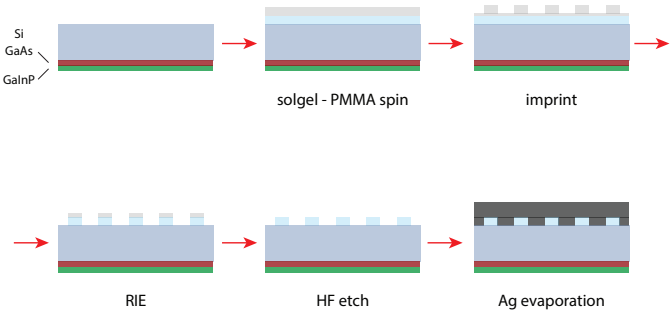

Figure 5.7: Overview of the fabrication steps needed to pattern the cells' back-reflector.

- A layer of PMMA (PMMA 950k A8, 240 nm) is spin-coated and baked at 150°C for 2 minutes. The thickness of the layer is equal to the final Ag nanodisks height.
- A layer of solgel (SCIL Nanoimprint Solutions NanoGlass T-1100, 75 nm) is spin-coated and, before solidification, the PDMS stamp is slowly brought in contact to mold the layer. After a 6 minutes curing time, the stamp is detached carefully.
- The solgel residual layer at the bottom of the imprinted holes is cleared via RIE using Oxford Instrument's PlasmaPro 80 and a process employing CHF_3 and Ar (etch rate 0.28 nm/s).

CHF_3 gas flow	25 [sccm]
Ar gas flow	25 [sccm]
pressure	15 [mTorr]
Set temperature	20 [°C]
RIE forward power	67 [W]
ICP power	0 [W]
time	150 [s]

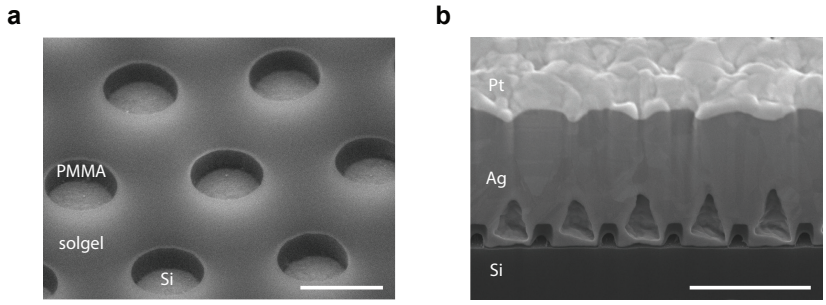

Figure 5.8: **a** Tilted SEM image of the patterned backside of Cell X623-7 after the RIE etch steps. The scale bar is 300 nm. **b** SEM image of a FIB cross section of the same cell after metal deposition. Conically-shaped air inclusions are clearly visible. The scale bar is 1 μm.

- The PMMA exposed in the solgel holes is etched down completely via Reactive Ion Etching (RIE) using an O_2 plasma (etch rate 7.94 nm/s).

O_2 gas flow	25 [sccm]
pressure	5 [mTorr]
Set temperature	20 [°C]
RIE forward power	200 [W]
ICP power	200 [W]
time	32 [s]

- The sample is shipped back to Fraunhofer ISE for further processing: a wet HF etch (5 min) removes the native oxide on the Si surface inside the PMMA holes to ensure proper electrical contact. Finally, 1 μm Ag followed by 200 nm Pt are sputtered and the front protection is removed.

Figure 5.8 shows the result of the fabrication procedure at two different steps. The samples are uniform over the entire patterned area with very few defects mainly due to dust particles. Figure 5.8a shows a SEM image of a triple-junction cell (sample X623-7) after the RIE etch steps. The solgel mask is smooth and uniform and the PMMA has a low sidewall roughness. Also, no residual PMMA is left in the holes after RIE. Metal deposition on such a patterned structure is quite challenging. Fig. 5.8b, shows conically-shaped air inclusions in the metal film. We attribute this to non–perfectly straight metal deposition during the sputtering process. Standard e-beam evaporation has been optimized to smoothly fill the PMMA holes but proved to have lower electrical performance. In the near future, a combination of sputtering and electrochemical deposition of Ag will be explored to avoid these issues.

In order to assess the impact of patterning on a device level, silicon bottom cells and full two–terminal triple–junction cells are optically and electronically characterized, first with a planar Ag back-reflector and finally with the fabricated optimized grating. External Quantum Efficiencies (EQEs) were measured using a grating monochromator set-up with adjustable bias voltage and bias spectrum while reflection measurements were performed on an integrated LOANA measurement device. One-sun I–V characteristics were

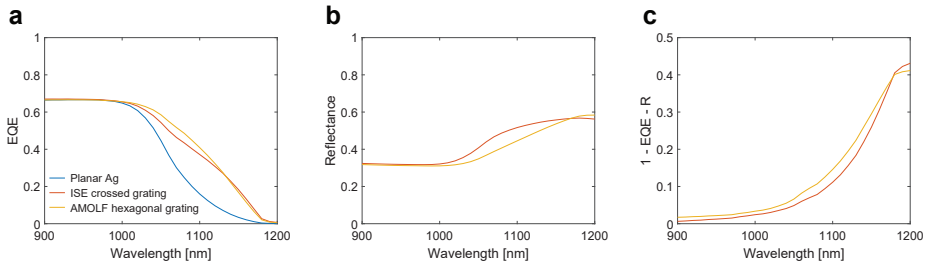

Figure 5.9: **a** Experimental EQE spectra for the optimized design described above ("AMOLF hexagonal grating"), for the optimized design in Ref. [12] ("ISE crossed grating") and for planar Ag back–reflector. **b** Measured reflectance spectra comparing the hexagonal and crossed gratings discussed above. **c** Calculated parasitic losses for the same two designs. All panels refer to a Si bottom cell with thickness 280 μm and no anti–reflection coating was applied to these samples.

measured under a spectrally adjustable solar simulator with one xenon lamp and two halogen lamp fields that are adjusted in intensity independently of each other to generate exactly the same current densities in each sub-cell as under illumination with the AM1.5G spectrum (IEC 90604-3, ed. 2 with 1000 $^{W}/_{m^2}$) [31]. The cell temperature was held at 25°C during the measurement. An aperture mask with an area of 3.984 cm^2 was placed on top of the III–V/Si solar cell to avoid any contribution of photo-generated carriers from outside the defined cell area.

Starting with Si bottom cells without anti–reflection coating, Fig. 5.9a highlights the enhancement in the External Quantum Efficiency (EQE) spectra due to the back–reflector nano-structuring. As anticipated by simulation, the experimental spectra demonstrate a distinct advantage in using the described optimized design. The lower reflectance achieved by the hexagonal grating (see Fig. 5.9b) can be ascribed to enhanced light–trapping capabilities but also to slightly increased parasitic losses. Indeed, the quantity 1 – EQE – R (see Fig. 5.9c) represents the fraction of photons that are absorbed but not collected as charges and hence lost due to parasitic plasmonic losses or collection inefficiencies. These are higher than estimated in simulation, most likely due to the non-ideal metal deposition possibly inducing higher parasitic absorption of optical and electrical nature (i.e. resistive losses). The high reflectance (and low EQE) compared to Fig. 5.6 is due to the absence of the anti–reflection coating at the top side of the cell.

Given the performance improvement validated on Si bottom cells, full two–terminal triple–junction GaInP/GaAs/Si cells were patterned and characterized. Similar to what observed in Fig. 5.9, also in this case there is a clear increase in EQE compared to the planar reference (see Fig. 5.10). The current density gain calculated from the EQE (data in Fig. 5.10a) amounts to 1.1 $^{mA}/_{cm^2}$. Again, the reflectance (see Fig. 5.10b) of the entire stack is greatly reduced in the bandwidth of interest.

It is important to stress that the very same cell is measured first with a planar Ag and, once the back–reflector is peeled off and a new patterned one is fabricated, with the optimized Ag grating design. However, this procedure cannot be repeated again, therefore the two different designs (i.e. "AMOLF hexagonal grating" and "ISE crossed grating" from Ref. [12]) cannot be compared directly on the same III-V/Si cell. Nonetheless, their com-

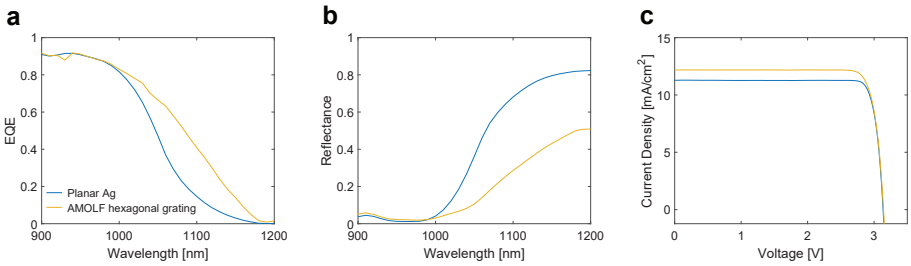

Figure 5.10: **a-b** Experimental EQE (a) and reflectance (b) spectra for the optimized hexagonal grating and for its planar reference. **c** Measured one-sun I–V characteristics comparing the cell with the optimized hexagonal grating and its planar reference. All the panels refer to the same triple–junction cell, with either a planar or a patterned back-contact.

	Planar Ag	AMOLF hex
η	31.2%	33%
J_{sc} [mA/cm^2]	11.3	12.2
V_{oc} [V]	3.135	3.142
FF	88.3%	86.2%

Table 5.1: Performance parameters (η, J_{sc}, V_{oc}, and FF) for the same cell (X623-7) with planar and patterned back-reflector.

parison is reliable on Si bottom cells (data in Fig. 5.9) as the manufacturing process of these cells is well controlled and efficiencies are very similar from cell-to-cell.

Lastly, one-sun I–V characteristics measurements conclude the cell performance characterization. The measured power conversion efficiency η, short circuit current density J_{sc}, open circuit voltage V_{oc}, and fill factor FF are summarized in Table 5.1. Corroborating the EQE enhancement, the I-V curves prove a clear increase in the J_{sc} due to optimized light–trapping and consequently higher absorption in Si. Importantly, any current gain in the Si sub-cell directly improves the J_{sc} of the entire stack as the silicon bottom cell is limiting the overall current flow in the series-connected device. It is worth pointing out that the J_{sc} value as extracted from the I–V characteristic differs slightly from its EQE–calculated counterpart. This could be due to a non perfect lamp calibration and to the different illumination area sizes used in the two techniques (3.984 cm^2 for the I-V measurements and 1 cm^2 for the EQE).

It is important to remark that the V_{oc} remains essentially unaltered compared to the planar reference. This implies that the cells are not damaged or electronically degraded by the back-reflector processing further proving the applicability of SCIL to high-efficiency solar cells.

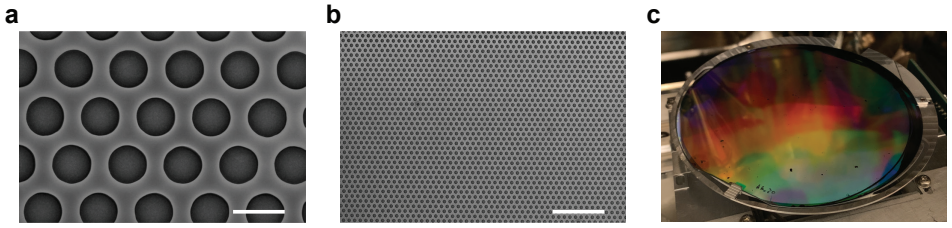

Figure 5.11: **a-b** SEM images of the patterned backside of a full 4 inch-diameter Si bottom cell after the RIE etch steps. The scale bar is 500 nm in panel a and 5 μm in b. **c** Photograph of the sample shown in panels a and b.

5.3. CONCLUSION

In conclusion, the results presented in this chapter demonstrate a nanophotonic light trapping scheme leading to an overall power conversion efficiency increase on a high performance GaInP/GaAs/Si triple-junction solar cell.

First, the concept of a diffractive back-reflector composed of a silver nano-disks hexagonal array is introduced and the relevant structural parameters are presented. Specifically, nano-disks' radius and height as well as the lattice periodicity are optimized employing a particle swarm optimization algorithm. Consequently, the performances of the optimal design are shown and analyzed, highlighting suppressed back-reflection to the 0^{th}-diffraction-order while keeping parasitic absorption low. To understand the working principle of such optimal design, the parameters' space is explored further and a simple model for the reflectance to the 0^{th}-diffraction-order is provided, along with its limitations. Next, the impact of the optimized design on the absorption in a thick Si slab is evaluated with OPTOS highlighting an increase over a planar back–reflector and over the design that is now featured in the current record cell. The fabrication process is described in depth and the resulting patterned Si bottom cells and full two–terminal triple–junction cells are characterized optically and electronically. We show experimentally a 1.8% efficiency gain on full GaInP/GaAs/Si triple-junction cells, and superior EQE on Si bottom cells compared to the design featured in the record cell, despite the presence of severe fabrication imperfections such as the air inclusions in Fig. 5.8b.

It is important to stress that the integration of a nanopatterned surface in the process flow of a high efficiency cell is far from trivial, yet it proved to be possible via SCIL with no signs of electrical degradation. As mentioned above, a combination of sputtering and electrochemical deposition of Ag will be explored in the near future to obtain better metal coverage. In addition, to avoid potential losses due to cells dicing, the whole fabrication process flow is now being scaled up to full 4–inch wafers. Figure 5.11 shows the first successfully patterned large-scale Si bottom cell.

Altogether, these results show a nanophotonic light trapping scheme based on gratings that can enhance the performances of cells where more traditional random texture strategies are not possible. Furthermore, the EQE data on Si sub-cells and the successful

implementation on full triple-junction solar cells support the possibility of GaInP/GaAs/Si cells featuring a patterned back-reflector with power conversion efficiencies above the current world record.

REFERENCES

[1] *World energy outlook 2020,* (2020).

[2] D. M. Chapin, C. S. Fuller, and G. L. Pearson, *A new silicon p-n junction photocell for converting solar radiation into electrical power,* Journal of Applied Physics **25**, 676 (1954).

[3] W. Shockley and H. J. Queisser, *Detailed balance limit of efficiency of p-n junction solar cells,* Journal of Applied Physics **32**, 510 (1961).

[4] A. Polman, M. Knight, E. C. Garnett, B. Ehrler, and W. C. Sinke, *Photovoltaic materials: Present efficiencies and future challenges,* Science **352** (2016), 10.1126/science.aad4424.

[5] E. C. Garnett, B. Ehrler, A. Polman, and E. Alarcon-Llado, *Photonics for photovoltaics: Advances and opportunities,* ACS Photonics **8**, 61 (2021).

[6] H. A. Atwater and A. Polman, *Plasmonics for improved photovoltaic devices,* Nature Materials **9**, 205 (2010).

[7] M. L. Brongersma, Y. Cui, and S. Fan, *Light management for photovoltaics using high-index nanostructures,* Nature Materials **13**, 451 (2014).

[8] Z. Yu, A. Raman, and S. Fan, *Fundamental limit of nanophotonic light trapping in solar cells,* Proceedings of the National Academy of Sciences **107**, 17491 (2010).

[9] V. E. Ferry, M. A. Verschuuren, M. C. v. Lare, R. E. I. Schropp, H. A. Atwater, and A. Polman, *Optimized spatial correlations for broadband light trapping nanopatterns in high efficiency ultrathin film a-si:h solar cells,* Nano Letters **11**, 4239 (2011).

[10] G. Yin, M. W. Knight, M.-C. van Lare, M. M. Solà Garcia, A. Polman, and M. Schmid, *Optoelectronic enhancement of ultrathin $CuIn_{1-x}Ga_xSe_2$ solar cells by nanophotonic contacts,* Advanced Optical Materials **5**, 1600637 (2017).

[11] L. van Dijk, J. van de Groep, L. W. Veldhuizen, M. Di Vece, A. Polman, and R. E. I. Schropp, *Plasmonic scattering back reflector for light trapping in flat nanocrystalline silicon solar cells,* ACS Photonics **3**, 685 (2016).

[12] R. Cariou, J. Benick, F. Feldmann, O. Höhn, H. Hauser, P. Beutel, N. Razek, M. Wimplinger, B. Bläsi, D. Lackner, M. Hermle, G. Siefer, S. W. Glunz, A. W. Bett, and F. Dimroth, *III–V-on-silicon solar cells reaching 33% photoconversion efficiency in two-terminal configuration,* Nature Energy **3**, 326 (2018).

[13] K. Yoshikawa, H. Kawasaki, W. Yoshida, T. Irie, K. Konishi, K. Nakano, T. Uto, D. Adachi, M. Kanematsu, H. Uzu, and K. Yamamoto, *Silicon heterojunction solar cell with interdigitated back contacts for a photoconversion efficiency over 26%,* Nature Energy **2**, 17032 (2017).

[14] D. D. Smith, P. Cousins, S. Westerberg, R. D. Jesus-Tabajonda, G. Aniero, and Y.-C. Shen, *Toward the practical limits of silicon solar cells,* IEEE Journal of Photovoltaics **4**, 1465 (2014).

[15] A. Richter, M. Hermle, and S. W. Glunz, *Reassessment of the limiting efficiency for crystalline silicon solar cells,* IEEE Journal of Photovoltaics **3**, 1184 (2013).

[16] M. A. Green and S. P. Bremner, *Energy conversion approaches and materials for high-efficiency photovoltaics,* Nature Materials **16**, 23 (2017).

[17] A. W. Y. Ho-Baillie, J. Zheng, M. A. Mahmud, F.-J. Ma, D. R. McKenzie, and M. A. Green, *Recent progress and future prospects of perovskite tandem solar cells,* Applied Physics Reviews **8**, 041307 (2021).

[18] NREL, *Best research-cell efficiency chart,* (2022).

[19] P. Schygulla, R. Müller, D. Lackner, O. Höhn, H. Hauser, B. Bläsi, F. Predan, J. Benick, M. Hermle, S. W. Glunz, and F. Dimroth, *Two-terminal III–V//Si triple-junction solar cell with power conversion efficiency of 35.9% at AM1.5g,* Progress in Photovoltaics: Research and Applications , 1 (2021).

[20] Lumerical Inc., *Optimization utility - particle swarm optmization,* (2022).

[21] A. A. Maradudin, I. Simonsen, J. Polanco, and R. M. Fitzgerald, *Rayleigh and Wood anomalies in the diffraction of light from a perfectly conducting reflection grating,* **18**, 024004 (2016).

[22] J. W. Strutt, *III. Note on the remarkable case of diffraction spectra described by Prof. Wood,* The London, Edinburgh, and Dublin Philosophical Magazine and Journal of Science **14**, 60 (1907).

[23] R. Wood, *XLII. On a remarkable case of uneven distribution of light in a diffraction grating spectrum,* The London, Edinburgh, and Dublin Philosophical Magazine and Journal of Science **4**, 396 (1902).

[24] E. Khaidarov, H. Hao, R. Paniagua-Domínguez, Y. F. Yu, Y. H. Fu, V. Valuckas, S. L. K. Yap, Y. T. Toh, J. S. K. Ng, and A. I. Kuznetsov, *Asymmetric nanoantennas for ultra-high angle broadband visible light bending,* Nano Letters **17**, 6267 (2017).

[25] Y. Ra'di, D. L. Sounas, and A. Alù, *Metagratings: Beyond the limits of graded metasurfaces for wave front control,* Phys. Rev. Lett. **119**, 067404 (2017).

[26] J. Eisenlohr, N. Tucher, O. Höhn, H. Hauser, M. Peters, P. Kiefel, J. C. Goldschmidt, and B. Bläsi, *Matrix formalism for light propagation and absorption in thick textured optical sheets,* Opt. Express **23**, A502 (2015).

[27] N. Tucher, J. Eisenlohr, P. Kiefel, O. Höhn, H. Hauser, M. Peters, C. Müller, J. C. Goldschmidt, and B. Bläsi, *3D optical simulation formalism OPTOS for textured silicon solar cells,* Opt. Express **23**, A1720 (2015).

[28] N. Tucher, J. Eisenlohr, H. Gebrewold, P. Kiefel, O. Höhn, H. Hauser, J. C. Goldschmidt, and B. Bläsi, *Optical simulation of photovoltaic modules with multiple textured interfaces using the matrix-based formalism OPTOS,* Opt. Express **24**, A1083 (2016).

[29] M. A. Verschuuren, M. Megens, Y. Ni, H. van Sprang, and A. Polman, *Large area nanoimprint by substrate conformal imprint lithography (SCIL),* Advanced Optical Technologies **6**, 243 (2017).

[30] M. A. Verschuuren, M. W. Knight, M. Megens, and A. Polman, *Nanoscale spatial limitations of large-area substrate conformal imprint lithography,* Nanotechnology **30**, 345301 (2019).

[31] M. Meusel, R. Adelhelm, F. Dimroth, A. Bett, and W. Warta, *Spectral mismatch correction and spectrometric characterization of monolithic III–V multi-junction solar cells,* Progress in Photovoltaics: Research and Applications **10**, 243 (2002).

6

CONCLUSION AND OUTLOOK

THE field of all–optical analog computing gained significant attention in the past and for quite some time seemed a promising alternative to standard electronic computing. However, as Moore's law kicked in, optical processors became quickly obsolete and were overwhelmed by what we nowadays mean by "computers".

The tremendous advances in nano–lithography that boosted the number of transistors per unit area also played a crucial role in the much more recent field of Nanophotonics. Metamaterials, metasurfaces, photonic crystals, plasmonics, and micro–resonators have now demonstrated the ability to mold the flow of light at the nano-scale with unprecedented precision. From this perspective, optical analog computing is still uncharted territory and the impact of nanophotonics on this field can be groundbreaking.

In this context, the work presented in this thesis helps to establish the field of all-optical processing via metasurfaces showing three different platforms that are compact and on-chip amenable. The possibility of integration into standard CMOS technology, in turn, enables exciting opportunities for hybrid analog-digital processing that operates at a higher data rate while simultaneously consuming less power.

Figure 6.1 shows an overview of the main experimental results presented in each chapter of the thesis.

In Chapter 2, we demonstrate how dielectric metasurfaces sustaining Fano resonances with suitably engineered dispersion can be designed to impart transfer functions in momentum space that correspond to 1^{st}– and 2^{nd}–order spatial differentiation. We show that the ideal amplitude and phase transfer functions can be realized over a relatively wide range of input angles spanning a numerical aperture up to 0.35 and a transmission amplitude larger than 0.8 can be achieved for large angles. Such NA ensures high spatial resolution and enables the implementation into standard imaging systems (e.g. smartphone cameras). Moreover, as our metasurface design operates in the image plane of the object and not in the Fourier plane, it can be placed directly onto the imaging chip for compact device implementations. The deviations from the ideal transfer functions, which are intrinsic to the design, are small enough to still achieve derivative operations close to ideal 1^{st}- and 2^{nd}-derivative. Furthermore, we experimentally demon-

strate metasurface-based optical processing using a suitably designed sub-wavelength array of Si nanobeams. As shown in Figure 6.1a, when the image of our institute logo is projected to the metasurface for resonant illumination (λ = 726 nm), clear edge detection is achieved, as a result of the 2nd-order spatial differentiation. Finally, we extend the metasurface for analog processing concept to 2D operations and unpolarized illumination. Optimized designs performing quasi-isotropic even- and odd-order spatial differentiation are presented and numerically demonstrate edge detection in all directions.

In Chapter 3, we couple a metasurface sustaining a Fano resonance to a gated WS_2 monolayer to achieve electrically-controllable optical processing. We leverage the impact of excitonic resonance quenching on the monolayer TMD's optical response to actively tune the metasurface transfer function. To demonstrate this, we design a device that acts as a high-pass filter that can be controlled by the presence (or absence) of excitons in the WS_2 monolayer. The optimum design achieves a numerical aperture of 0.2 and a transmission amplitude close to 0.8 at the maximum k-vector processed. Numerical tests on multiple input test functions and images clearly demonstrate reliable edge filtering that can be turned on and off at λ = 626 nm and λ = 620 nm. Next, we fabricate a chip containing several devices, each composed of an array of TiO_x nanowires on a WS_2 monolayer gated via a MOSFET-like configuration (see Figure 6.1b). Optical reflectance spectra clearly show both the A-exciton feature and the GMR-based Fano lineshape. Figure 6.1b demonstrates reflectance modulation under an applied external bias, showing the potential of the proposed hybrid metasurface–2D-TMD platform.

To go beyond image processing tasks, in Chapter 4 we present a Si metasurface-based platform for analog computing that is able to solve Fredholm integral equations of the second kind using free-space visible radiation. Inverse design routines enable the implementation of a specific scattering matrix synthesizing a prescribed kernel into a Si metagrating. To prove the generality of this technique, we set as the optimization goal a random passive and reciprocal kernel. The optimum design provides a scattering matrix that is very close to the desired one at the target wavelength λ = 706 nm. Next, a semi-transparent mirror is incorporated into the sample to provide adequate feedback and thus perform the required Neumann series solving the corresponding equation in the analog domain at the speed of light. The solution provided by the metasurface in simulation effectively solves the problem of interest and is very close to its ideal counterpart. The designed metagrating is patterned onto a Si-on-sapphire substrate (see Figure 6.1c) showing small deviations between experiment and simulations. The comparison between the retrieved experimental solution and the ideal solution with the chosen kernel shows good agreement at a slightly blue-shifted wavelength of λ = 699 nm, as shown in Figure 6.1c. Visible wavelength operation enables a highly compact, ultra-thin device, which results into high processing speeds and the possibility of on-chip integration.

Finally, in Chapter 5 we apply the insights gained on grating design to a nanophotonic light trapping scheme in the near-IR wavelength range to boost the efficiency of high-performance GaInP/GaAs/Si triple-junction solar cells. We optimize a nanopatterned Ag back-reflector at the bottom of the Si sub-cell to redirect light at diffraction angles beyond the escape cone of the Si absorber. The back-reflector consists of a hexagonal array of silver nanodisks embedded in a PMMA layer and in direct contact with Si.

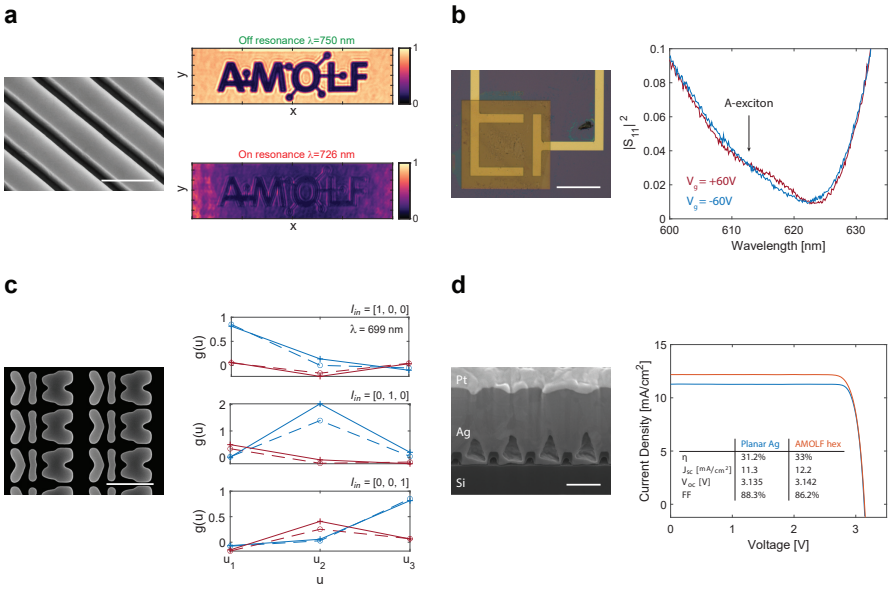

Figure 6.1: **a** Chapter 2. Left: tilted SEM image of the Si metasurface performing the 2nd–derivative operation (scalebar 400 nm). Right: optical microscopy image of the metasurface output for resonant (λ = 726 nm) and off-resonant (λ = 750 nm) illumination, demonstrating experimentally 2nd–order image differentiation. **b** Chapter 3. Left: optical microscopy image (scalebar 100 μm) of a representative completed device. Right: measured reflectance spectra for the same device as the bias voltage is switched from $V_g = +60$ V to $V_g = -60$ V. **c** Chapter 4. Left: top-view SEM image of the patterned Si metagrating (scalebar 500 nm). Right: estimated experimental analog solution (real and imaginary parts in blue and red respectively) of the integral equation (dashed line) compared to the ideal theoretical solution (solid lines), for the three orthogonal input vectors $(1,0,0)^\mathsf{T}$, $(0,1,0)^\mathsf{T}$, $(0,0,1)^\mathsf{T}$. The wavelength of operation in this simulation is $\lambda = 699$ nm. **d** Chapter 5. Left: SEM image of a FIB cross-section of the patterned Ag back-reflector on a triple–junction cell (scale bar 500 nm). Right: experimental one-sun I–V characteristics comparing the cell with the optimized hexagonal grating and its planar reference. Inset: performance parameters (η, J_{sc}, V_{oc}, and FF) of the same cell with planar and patterned back-reflector.

A simple interference model explains the physics governing reduced reflectance to the 0th diffraction order and further provides a guide on how to optimize the structural parameters. Next, the impact of the optimized design on the absorption in a thick Si slab is evaluated, highlighting an increase compared to a planar back–reflector as well as the design that is featured in the current record cell. Figure 6.1d shows a fabricated nanopatterned back-reflector on a full two–terminal triple–junction cell. The experimental external quantum efficiencies and one-sun current–voltage characteristics demonstrate a significant performance improvement over the planar reference (see inset of Figure 6.1d) without any measurable electrical degradation in the V_{oc} due to the patterning process. These results highlight the potential to achieve efficiencies above the current record cell. Moreover, similar strategies can be applied to other Si-based tandem cells where standard random texture is not viable.

OUTLOOK

The results of this thesis offer a path to a wide range of applications and can open new opportunities in hybrid optical and electronic computing that operates at low cost, low power, and small dimensions. Future research directions could include:

- Demonstration of other mathematical operations including convolutions with specific functions. Also, 1^{st}–order spatial differentiation has still to be demonstrated experimentally. This, in turn, would require upgrades to the setup described in Section 2.6.2 targeting phase measurements in order to assess the asymmetric phase response of odd operations.

- Scaling–up of metasurface dimensions via SCIL and device integration. In order to apply the proposed designs to standard imaging chips, the patterned area has to be drastically increased to the cm-scale. This has been demonstrated to be possible without compromising resolution via SCIL, as shown in Chapter 5. It is worth stressing that the spatial differentiator metasurfaces presented in this thesis operate in the image plane and therefore can be directly applied onto the CCD of an existing imaging system (see Figure 6.2a). For best efficiency, the NA of the metasurface should match that of the imaging system. This is possible due to the design flexibility shown in Chapter 2.

- Monolithic compound optical elements. It is possible to envision a monolithic stack composed of a metalens, a free-space compressor metasurface, and a spatial differentiator, representing the ultimate miniaturization of an optical imaging system. Notice that precise lateral alignment of the components is not required.

- Non-reciprocal image processing. Optical isolators are components that allow light transmission only in one direction. This requires breaking reciprocity and can be achieved, among other schemes, relying on the optical Kerr effect: the permittivity of a material depends on the local electric field intensity via the third-order nonlinear susceptibility $\chi^{(3)}$. Fano resonators based on gratings supporting GMR and with Kerr nonlinearity have been proposed as isolators given their sharp response in frequency and transmission swinging from zero to a peak in a narrow bandwidth. If the resonator is designed to exhibit a different field distribution upon excitation from opposite directions, the Fano lineshape spectral location will also be dependent on the excitation port. This offset in wavelength between the Fano lineshape for forward and backward excitation defines a bandwidth where isolation can be achieved. As demonstrated in Chapter 2 the same structures can be designed to have a certain transfer function and thus to impart a given mathematical operation on an input signal. The combination of this concept with Kerr nonlinear isolators suggests the possibility of designing a structure with different transfer functions when excited from opposite directions. For instance, the minimum in transmission in the forward direction at normal incidence can be aligned to a maximum for backward propagation, leading in one case to edge detection (high-pass filter) yet to image blurring (low-pass filter) in the other direction, as schematically illustrated in Figure 6.2b.

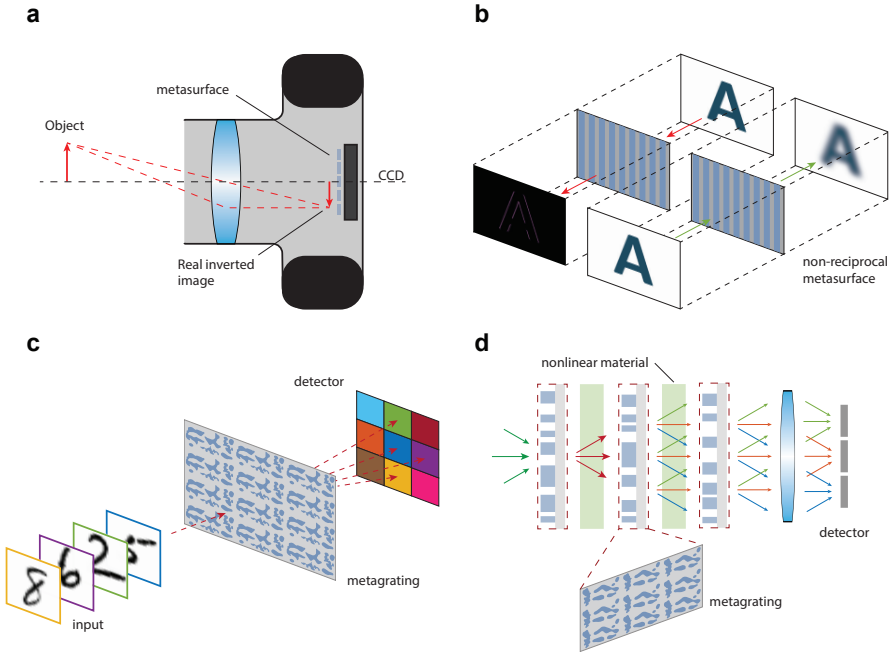

Figure 6.2: **a** Ray diagram for a standard imaging system. The metasurface can be placed directly on the imaging sensor (CCD). **b** Nonreciprocal image processing metasurface performing edge detection in the forward direction and image blurring in the backward direction. **c** A metagrating is designed to send light to a specific direction depending on the input character. **d** Schematic representation of a metagrating-based analog neural network. A wave signal is sent to the first layer and is diffracted by the first metasurface. Next, the power diffracted into the output channels is modulated by a nonlinear material (i.e. transmission changes with intensity). This process is repeated N times (i.e. N layers) until the final outcome is focused onto a standard detector.

Furthermore, a metasurface could be designed to have a transfer function that depends on the intensity of the input image.

- TMD-based metasurfaces with continuously tunable functionality. The excitonic resonance exploited in Chapter 3 shows a blue shift as the temperature goes down (see Figure 3.13). This can be used in combination with a metasurface sustaining a GMR to engineer the k-space response to continuously change as a function of temperature for a fixed illumination wavelength.

- Pattern recognition. Using inverse design routines, an optimized metagrating could be "trained" to recognize an input image by steering light to a specific diffraction channel (Figure 6.2c). This requires optimization of the k-space response of each element of the grating scattering matrix. Note that the unit cell can be large to allow for more degrees of freedom in the design and some diffraction channels may also be discarded. Essentially, this can be thought of as the character recognition

scheme based on matched filters illustrated in Chapter 1 but squeezed into a single surface.

- Metagrating-based analog neural networks. Neural networks can be thought of as a series of matrix multiplication and nonlinear renormalizations. Both ingredients are available and can be designed in the realm of nanophotonics.Utilizing topology optimization and adjoint method, we can devise and manufacture metasurfaces with designer scattering matrices. Regarding non-linearity, on the other end, there are several ways to obtain nonlinear behavior for light. For example with Kerr-type non-linearity, saturable absorber or coupling with atomic systems with discrete levels. The proposed device consists of a series of 2D crossed gratings with an inverse-designed unit cell that will provide the needed matrix multiplication (in phase and amplitude) between the diffraction channels in input and output. Next, a nonlinear material is sandwiched between the metasurfaces to provide the required renormalization. Eventually, a lens focuses the diffracted plane waves onto different pixels of a CCD detector. As schematically depicted in Figure 6.2d, a wave signal is sent to the first layer and is diffracted by the first metasurface. Next, the power diffracted into the output channels is modulated by a nonlinear material (i.e. transmission changes with intensity). This process is repeated N times (i.e. N layers) until the final outcome is focused onto a standard CCD detector. It is worth pointing out that, similar to standard neural networks, the connectivity of hidden layers can be increased at will by suitably changing the pitch of the metagratings and hence increasing the number of diffracted channels. One important advantage regarding fabrication is that lateral alignment across the layers is not needed. This in turn means that each metasurface can be fabricated independently.

- Nonlinear integral equation solver. By including nonlinear materials within the feedback system (e.g., replacing the SiO_2 spacer layer) of the integral solver proposed in Chapter 4, it would be possible to solve nonlinear mathematical problems. Additionally, nonlinearity could also be applied after processing the information via linear operations. Hence, a dedicated external nonlinear device could be designed to process the outputs of our metastructure.

To conclude, these and other opportunities will be explored in the near future at AMOLF (Amsterdam) in close collaboration with the groups of Prof. Andrea Alù at ASRC (New York) and Dr. Jorik van de Groep at Universiteit van Amsterdam.

A

APPENDIX

This appendix contains the calculations that support the model presented in Chapter 2. Specifically, the scattering matrix formalism and the coupled-mode-theory model used are shown in a step-by-step fashion.

A.1. SCATTERING MATRIX FORMALISM

Light interaction with a generic optical system may be described by a set of linear equations which relate incident, transmitted and reflected wave amplitudes. These linear relationships define a matrix called *scattering matrix* or S – matrix. In particular, it relates the outgoing complex wave amplitudes $\mathbf{s}_-$ to the incoming complex wave amplitudes $\mathbf{s}_+$. For a two–ports configuration[1]

$$\begin{pmatrix} s_{1-} \\ s_{2-} \end{pmatrix} = \begin{pmatrix} S_{11} & S_{12} \\ S_{21} & S_{22} \end{pmatrix} \begin{pmatrix} s_{1+} \\ s_{2+} \end{pmatrix} \quad \leftrightarrow \quad \mathbf{s}_- = \mathsf{S}\mathbf{s}_+ \tag{A.1}$$

where the complex wave amplitudes are defined and normalized such that, for example, $|s_{1+}|^2$ is the power per unit area incident on the the system

$$s_{1+} = \sqrt{\frac{cn_0\epsilon_0}{2}}\mathbf{E}_{1+} \tag{A.2}$$

with analogous definitions for the remainder components of the vectors $\mathbf{s}_-$ and $\mathbf{s}_+$. General requirements such as energy conservation, reciprocity and time reversibility constrain the matrix elements of S [3].

First, if the system is lossless all the energy pumped into the system has to go out. Hence power conservation implies

$$|s_{1+}|^2 + |s_{2+}|^2 = |s_{1-}|^2 + |s_{2-}|^2 \quad \leftrightarrow \quad \mathbf{s}_+^\dagger \mathbf{s}_+ = \mathbf{s}_-^\dagger \mathbf{s}_- \tag{A.3}$$

Parts of this chapter have been re-adapted from Refs. [1, 2].

[1] It is straightforward to generalize this to a m port system using a M×M scattering matrix

and using $\mathbf{s}_- = \mathsf{S}\mathbf{s}_+$

$$\mathbf{s}_+^\dagger \mathbf{s}_+ = \mathbf{s}_+^\dagger \mathsf{S}^\dagger \mathsf{S} \mathbf{s}_+ \quad \rightarrow \quad \mathbf{s}_+^\dagger \mathbf{s}_+ - \mathbf{s}_+^\dagger \mathsf{S}^\dagger \mathsf{S} \mathbf{s}_+ = 0 \tag{A.4}$$

$$\rightarrow \quad \mathbf{s}_+^\dagger \left[\mathbb{I} - \mathsf{S}^\dagger \mathsf{S} \right] \mathbf{s}_+ = 0 \quad \forall \mathbf{s}_+ \implies \mathsf{S}^\dagger \mathsf{S} = \mathbb{I} \tag{A.5}$$

where $\mathbb{I}$ is the identity matrix. The constraint implied by unitarity on the matrix elements are

$$\begin{cases} |S_{11}|^2 + |S_{12}|^2 = 1 \\ |S_{22}|^2 + |S_{21}|^2 = 1 \\ S_{11}^* S_{12} + S_{21}^* S_{22} = 0 \end{cases}$$

Another property that holds for lossless media is *time reversibility*. To show its implications on the S – matrix elements the complex conjugate of (A.1) is taken

$$\mathbf{s}_-^* = \mathsf{S}^* \mathbf{s}_+^* \tag{A.6}$$

The complex wave amplitudes $\mathbf{s}_-^*$ may be interpreted as time reversed out-going wave amplitudes thus incoming wave amplitudes ($\mathbf{s}_-^* \rightarrow \mathbf{s}_+$) and the same reasoning applies for $\mathbf{s}_-^*$ (i.e. $\mathbf{s}_+^* \rightarrow \mathbf{s}_-$). With these substitutions (A.1) becomes

$$\mathbf{s}_+ = \mathsf{S}^* \mathbf{s}_- \quad \rightarrow \quad \mathbf{s}_- = \left[\mathsf{S}^* \right]^{-1} \mathbf{s}_+ \tag{A.7}$$

Comparing this last equation with (A.1) yields

$$\left[\mathsf{S}^* \right]^{-1} = \mathsf{S} \quad or \quad \mathsf{S}^* = \mathsf{S}^{-1} \tag{A.8}$$

This condition together with the first discussed property $\mathsf{S}^\dagger = \mathsf{S}^{-1}$ leads to

$$\mathsf{S}^\top = \mathsf{S} \tag{A.9}$$

This same result can be obtained also from the reciprocity principle for an isotropic medium. Therefore time reversibility and power conservation imply reciprocity [3].

A.2. COUPLED MODE THEORY

The *Coupled Mode Theory* (CMT) formalism is very powerful in describing the behavior of a resonator coupled to input and output ports. This theory has been developed mainly by Hermann Haus [3] and further refined by Fan et al. [4]. Moreover, it enables the possibility of calculating the transmission of an optical system by modeling its interaction with incoming light through a direct process and a resonant process. Thus, it is a valuable tool to model guided–mode–resonances.

The first step is to defining the optical system and the output and input planes. Hence, suppose our resonant structures (nanopillars or nanowires) are enclosed inside a "black box" simply stating that the complex field inside the box is u (normalized such that $|u|^2$ is the energy stored within the box due to the resonance) and that this system has a certain resonance frequency ω_0. In our case the latter is a guided–mode–resonance, however within the frame of CMT there is no need to further specify the nature of the resonance.

The outgoing wave amplitudes $\mathbf{s}_-$ are the result both of the box's leakage and of the action of a scattering matrix C, which would describe the system if the resonances were turned off, to the incoming wave amplitudes $\mathbf{s}_+$

$$\mathbf{s}_- = \mathsf{C}\,\mathbf{s}_+ + u\,\mathbf{d} \tag{A.10}$$

where $\mathbf{d} = (d_1, d_2)^\top$ is a vector of coupling coefficients. As mentioned in Chapter 2, the direct process is modeled by the interaction of light with a dielectric slab of index $n_{\text{eff}} = [(1-F)n_0^2 + Fn^2]^{1/2}$ (with $n = 4$) in air ($n_0 = 1$) where F is the structure fill-factor [5]. Thus in our model (A.10) reads

$$\begin{pmatrix} s_{1-} \\ s_{2-} \end{pmatrix} = \begin{pmatrix} r & t \\ t & r \end{pmatrix} \begin{pmatrix} s_{1+} \\ 0 \end{pmatrix} + u \begin{pmatrix} d_1 \\ d_2 \end{pmatrix} \tag{A.11}$$

where r and t are the Fresnel coefficients for a Fabry-Pérot etalon of thickness d equal to the height of the metasurface

$$r = \frac{r_1 + r_2 e^{-2i\delta}}{1 + r_1 r_2 e^{-2i\delta}} \qquad t = \frac{t_1 t_2 e^{-i\delta}}{1 + r_1 r_2 e^{-2i\delta}} \tag{A.12}$$

r_1, r_2, t_1, t_2, are the standard Fresnel reflection and transmission coefficients for the two slab interfaces and $\delta = (2\pi/\lambda)\, n_{\text{eff}}\, d \cos\theta_1$ (θ_1 is the angle at which light is refracted inside the slab in case of not normal incidence).

Equation (A.11) shows clearly that the output of the optical system is the sum of a direct process (first product on the right-hand side) and a resonant process (second product on the right-hand side). Notice that s_{2+} is zero since no light is coming from the substrate.

Coupled to (A.11), another equation is needed to describe the complex field inside the system

$$\frac{du}{dt} = \left(i\omega_0 - \gamma\right) u + \kappa_1 s_{1+} \tag{A.13}$$

where γ is the radiative leakage and κ_1 is the coupling coefficient for s_{1+} pumping the resonator[2]. In the frequency domain $\frac{d}{dt} \to i\omega\cdot$ therefore, from (A.13)

$$i\omega u = \left(i\omega_0 - \gamma\right) u + \kappa_1 s_{1+} \quad \to \quad u = \frac{\kappa_1 s_{1+}}{i(\omega - \omega_0) + \gamma} \tag{A.14}$$

The product of (A.11) leads instead to

$$\begin{cases} s_{1-} = r s_{1+} + u d_1 \\ s_{2-} = t s_{1+} + u d_2 \end{cases}$$

Using the second equation of this system and (A.14) it is straightforward to write the following expression for s_{2-}

$$s_{2-} = t s_{1+} + \frac{d_2 \kappa_1 s_{1+}}{i(\omega - \omega_0) + \gamma} \tag{A.15}$$

[2] κ_1 is the first component of the vector κ of coupling coefficients

A

and to define the quantity

$$S_{21} = \frac{s_{2-}}{s_{1+}} = t + \frac{d_2 \kappa_1}{i(\omega - \omega_0) + \gamma} \tag{A.16}$$

This last quantity is of great importance in our derivation since the transmittance of the whole system is $T = |S_{21}|^2$ as can be noted recalling the definitions of $\mathbf{s}_-$ and $\mathbf{s}_+$. However, (A.16) is not our final result. Indeed, the coupling coefficients showing in the last equation cannot be unbound since the transmittance itself is bound to be $T \leqslant 1$. Actually they are constrained by the direct pathway through these properties [4, 6, 7]

$$\mathbf{d}^\dagger \mathbf{d} = 2\gamma \tag{A.17}$$

$$\kappa = \mathbf{d} \tag{A.18}$$

$$\mathsf{C}\,\mathbf{d}^* = -\mathbf{d} \tag{A.19}$$

where C is a generic scattering matrix describing the direct pathway and γ is the sum of the leakage rates into the ports.

These properties[3] and those previously discussed regarding the S – matrix will be of great use in further refining the expression obtained for S_{21}. Indeed, applying (A.18) to (A.16) and exploiting the mirror symmetry of the problem ($d_1 = \pm d_2$, the sign being chosen according to the even or odd symmetry of the resonant mode)[4]

$$S_{21} = t \pm \frac{d_1^2}{i(\omega - \omega_0) + \gamma} \tag{A.20}$$

Furthermore, (A.17) and (A.19) will enable the possibility of deducing an expression for d_1^2. In our case $\mathsf{C}\,\mathbf{d}^* = -\mathbf{d}$ reads

$$\begin{pmatrix} r & t \\ t & r \end{pmatrix} \begin{pmatrix} d_1^* \\ \pm d_1^* \end{pmatrix} = - \begin{pmatrix} d_1 \\ \pm d_1 \end{pmatrix} \tag{A.21}$$

and performing the product the following expression for d_1 is extracted

$$d_1^* (r \pm t) = -d_1 \tag{A.22}$$

next, multiplying the latter for d_1 and using (A.17)

$$d_1^2 = -(r \pm t)\gamma \tag{A.23}$$

Hence, the final expression used in Chapter 2 for the transmission S_{21} is

$$\boxed{S_{21} = t \pm \frac{-(r \pm t)\gamma}{i(\omega - \omega_0) + \gamma}}$$

Before moving on, it is worth commenting this last result. This relatively simple equation elegantly embodies the intuitive working principle of our structure and highlights

[3] The detailed proofs will be discussed in the next section.

the origin of the Fano asymmetric lineshape. The quantity S_{21} is evidently the sum of two terms: t is simply the Fresnel coefficient for a dielectric slab and plays the role of the *direct pathway* mentioned earlier while the second term is due to the resonant behavior displayed by our structure and hence is referred to as *resonant pathway*. Furthermore, the direct path itself contains the resonant path (A.23) as a consequence of the constraints imposed ultimately by fundamental concepts such as energy conservation and time-reversal symmetry.

Since the two terms appearing in S_{21} are complex numbers, it is important to study their relative phase difference to understand how that influences the shape parameter, as discussed in Chapter 2.

A.2.1. PROOFS OF PROPERTIES (A.17) - (A.19)

For ease of notation the properties above will be proved for a single port resonator and then generalized. Hence (A.11) and (A.13) become

$$\frac{du}{dt} = \left(i\omega_0 - \gamma\right) u + \kappa s_{1+} \tag{A.24}$$

$$s_{1-} = C s_{1+} + d u \tag{A.25}$$

where C is now a number and γ is the leakage into the only port.

Proof. $dd^* = 2\gamma$
Suppose that the incoming wave amplitudes are turned off ($s_{1+} = 0$). Using (A.24)

$$\begin{aligned}
&\frac{d|u|^2}{dt} = \frac{duu^*}{dt} = u\frac{du^*}{dt} + u^*\frac{du}{dt} = \\
&= u\left[(-i\omega_0 - \gamma)u^*\right] + u^*\left[(i\omega_0 - \gamma)u\right] = \\
&= -i\omega_0|u|^2 - \gamma|u|^2 + i\omega_0|u|^2 - \gamma|u|^2 = -2\gamma|u|^2 \\
&\implies \frac{d|u|^2}{dt} = -2\gamma|u|^2
\end{aligned}$$

Since $|u|^2$ is the energy stored inside the resonator and given the definition of s_{1-}, power conservation implies

$$\begin{aligned}
&\frac{d|u|^2}{dt} = -|s_{1-}|^2 = -|d|^2|u|^2 = -dd^*|u|^2 \\
&\implies \frac{d|u|^2}{dt} = -dd^*|u|^2
\end{aligned}$$

Looking at both the results it is clear that $dd^* = 2\gamma$. □

Proof. $\kappa = d$
Again, if the incoming wave amplitudes are turned off ($s_{1+} = 0$) it is straightforward to give a solution for (A.24)

$$\begin{cases} \frac{du}{dt} = \left(i\omega_0 - \gamma\right) u \\ s_{1-} = d u \end{cases} \quad \rightarrow \quad \begin{cases} u = Ae^{(i\omega_0 - \gamma)t} \\ s_{1-} = dAe^{(i\omega_0 - \gamma)t} \end{cases}$$

where A is a constant. As expected, the energy stored inside the resonator decays with time as does the amplitude of the outgoing wave s_{1-}. Next, a time-reversal transformation is performed

$$\begin{cases} u(t) \to u^*(-t) \\ s_{1-}(t) \to s_{1-}^*(-t) \end{cases} \quad \to \quad \begin{cases} u^* = A^* e^{(i\omega_0+\gamma)t} \\ s_{1-}^* = d^* A^* e^{(i\omega_0+\gamma)t} \end{cases}$$

In this new configuration an exponentially growing incoming wave amplitude is building-up the energy stored from 0 at $t=-\infty$ to $|A|^2$ at $t=0$. The coupled equations describing this new situation are

$$\frac{du^*}{dt} = \left(i\omega_0 - \gamma\right) u^* + \kappa s_{1-}^* \tag{A.26}$$

$$0 = C s_{1-}^* + d u^* \tag{A.27}$$

in a similar manner as done previously to obtain (A.14), from these last two equation

$$u^* = \frac{\kappa s_{1-}^*}{i(\omega - \omega_0) + \gamma} \tag{A.28}$$

The complex field u^* is driven by s_{1-}^* at a frequency ω_0 and with an amplitude growing at the rate γ. Thus the complex frequency of the drive is $\tilde{\omega} = \omega_0 + i\gamma$ and also the complex field u^* will have the same

$$u^*(\tilde{\omega}) = \frac{\kappa s_{1-}^*}{i(\omega_0 - i\gamma - \omega_0) + \gamma} = \frac{\kappa s_{1-}^*}{2\gamma} = \frac{\kappa d^* u^*}{2\gamma}$$

$$\to u^* = \frac{\kappa d^* u^*}{2\gamma} \implies 1 = \frac{\kappa d^*}{2\gamma}$$

where $s_{1-}^* = d^* u^*$ has been used [4]. From this last result it follows that $\kappa d^* = 2\gamma$ and exploiting the property proved earlier $d d^* = 2\gamma$ it is evident that $\kappa = d$. □

Proof. $C d^* = -d$
Starting from the time-reversed situation discussed above, notice that no outgoing wave shall occur i.e.

$$0 = C s_{1-}^* + d u^*$$

exploiting again $s_{1-}^* = d^* u^*$ the property is proved

$$0 = C d^* u^* + d u^* \quad \forall u \implies C d^* = -d$$

□

The three properties just shown can be generalized for a multi-port resonator obtaining (A.17), (A.18) and (A.19). In particular (A.17) for m ports is equivalent to

$$d_1^* d_1 + d_2^* d_2 + \dots d_m^* d_m = \sum_i \gamma_i = \gamma$$

[4] Notice that this substitution is valid only at t=0. In fact, s_{1-}^* is a function growing from 0 at $t=-\infty$ to $d^* A^*$ at $t=0$ while s_{1-} is decreasing from dA at $t=0$ to 0 at $t=+\infty$. Thus s_{1-}^* is the complex conjugate of s_{1-} only at t=0

being γ_i the leakage into port i. Further, from the equation above it can be set

$$
\begin{aligned}
d_1^* d_1 &= \gamma_1 \\
d_2^* d_2 &= \gamma_2 \\
&\dots \\
d_m^* d_m &= \gamma_m .
\end{aligned}
$$

A

REFERENCES

[1] A. Cordaro, *All-silicon metasurfaces for anti-reflection*, Masters' thesis, Stanford University, University of Catania (2017).

[2] A. Cordaro, J. van de Groep, S. Raza, E. F. Pecora, F. Priolo, and M. L. Brongersma, *Antireflection High-Index Metasurfaces Combining Mie and Fabry-Pérot Resonances,* ACS Photonics **6**, 453 (2019).

[3] H. A. Haus, *Waves and fields in optoelectronics* (Prentice-Hall, Englewood Cliffs, N.J, 1984) p. 402.

[4] S. Fan, W. Suh, and J. D. Joannopoulos, *Temporal coupled-mode theory for the fano resonance in optical resonators,* Journal of the Optical Society of America. A **20**, 569 (2003).

[5] D. L. Brundrett, E. N. Glytsis, and T. K. Gaylord, *Homogeneous layer models for high-spatial-frequency dielectric surface-relief gratings: conical diffraction and antireflection designs,* Applied Optics **33**, 2695 (1994).

[6] K. X. Wang, Z. Yu, S. Sandhu, and S. Fan, *Fundamental bounds on decay rates in asymmetric single-mode optical resonators,* Optics Letters **38**, 100 (2013).

[7] K. X. Wang, Z. Yu, S. Sandhu, V. Liu, and S. Fan, *Condition for perfect antireflection by optical resonance at material interface,* Optica **1**, 41 (2014).

SUMMARY

The world's ever-growing need for efficient computing has been driving researchers from diverse research fields to explore alternative pathways to the current digital computing paradigm. The processing speed and energy efficiency of standard electronics have become the limiting factors for novel disruptive applications entering our everyday life, including artificial intelligence, machine learning, and computer vision. Image processing is at the core of many of these technologies and is typically performed digitally using integrated electronic circuits and algorithms, implying fundamental speed limitations and significant power consumption. These processes can also be performed instantaneously and at low power by purely analog Fourier optics. However, this requires bulky optical components.

In this context, analog computing has resurfaced and regained significant attention as a complementary route to traditional architectures. Specifically, the tremendous recent advances in the field of metamaterials and metasurfaces have been unlocking new opportunities for all-optical computing strategies, given the possibility of shaping optical fields in extreme ways over sub-wavelength thicknesses. Analog processing metasurfaces would benefit from the speed and low power consumption of optics while simultaneously being a chip-scale technology enabling hybrid optical and electronic data processing on a single chip.

The idea of using light to outsource specific computing tasks comes with several advantages. First, there is a clear enhancement in processing speed as the computation is performed at the speed of light traveling through metamaterials with typical sizes smaller than or comparable with the wavelength of operation. Also, processing signals in the optical domain enables massive parallelization and may potentially avoid unnecessary analog-to-digital conversion. For example, several image processing tasks can be performed before the image is discretized into pixels, relying on the possibility of engineering the angular response of metasurfaces and hence impart instantaneously a mathematical operation to the spatial content of an input signal. Finally, analog computing meta-devices can be passive, implying extremely low energy consumption.

The work presented in this thesis helps to establish the field of all-optical processing via metasurfaces showing different platforms that are compact and on-chip amenable. The possibility of integration into standard CMOS technology, in turn, enables exciting opportunities for hybrid analog-digital processing that operates at higher data rates and lower power usage.

In Chapter 2, we demonstrate for the first time that judiciously engineered silicon metasurfaces can perform mathematical operations and optical image edge detection in a fully analog way. The key to our work is that Fano-resonances in a compact geometry of silicon nanobeam arrays unlock a diversity of operations in the Fourier domain, acting both on amplitude and phase. We describe how to tailor the spatial dispersion of the metasurface by manipulating its leaky modes and the related Fano resonance asymme-

try and linewidth. Based on this, we present metasurface designs that perform either 1st- or 2nd-order spatial differentiation. We experimentally demonstrate the 2nd–derivative operation on two-tone and gray-scale input images, directly showing the potential of all-optical edge detection. A unique advantage of our silicon metasurface geometry is that it operates at a large numerical aperture of 0.35, more than 25 times higher than previously explored schemes, which implies it can be readily integrated into practical imaging systems. In addition, it also offers largely enhanced efficiency, ensuring close-to-ideal transmission for differentiation using passive devices. Finally, we extend the formalism to 2D operations and unpolarized illumination. Optimized designs performing quasi-isotropic even– and odd–order spatial differentiation are presented and numerically demonstrate edge detection in all directions.

Chapter 3 describes an electrically-controllable metasurface for optical processing. To achieve this, a metasurface sustaining leaky modes guided along its surface is coupled to an electrically gated WS_2 monolayer. We leverage the impact of excitonic resonance quenching on the monolayer TMD's optical response to alter the metasurface transfer function. This rationale is used to design a switchable Fourier spatial filter. Specifically, the device acts as a high-pass filter that can be perturbed by the presence (or absence) of excitons in the WS_2 monolayer. The optimum design achieves a numerical aperture of 0.2 and a transmission close to 0.8 at the maximum k-vector processed. Numerical tests on an optimized design clearly demonstrate reliable edge filtering that can be turned on and off at $\lambda = 626$ nm and $\lambda = 620$ nm illumination wavelengths. Next, we fabricate a chip containing several devices each composed of an array of TiO_x nanowires on a WS_2 monolayer gated via a MOSFET-like configuration. Optical characterization under an applied external bias shows modulation of the Fano resonance in reflectance following the same trends of the simulations, showing the potential of the proposed hybrid metasurface–2D-TMD platform. The results are a major first step for optical computing metasurfaces devices with functionalities that can be actively tuned during operation.

In Chapter 4, we present an ultra-thin Si metasurface-based platform for analog computing that is able to solve Fredholm integral equations of the second kind using free-space visible radiation. Using topology optimization, we implement a specific scattering matrix synthesizing a prescribed kernel into a Si metagrating. To prove the generality of this technique, we set as the optimization goal a random passive and reciprocal kernel. The optimum design provides a scattering matrix very close to the desired one at the target wavelength $\lambda = 706$ nm. Next, a semi-transparent mirror is incorporated into the sample to provide adequate iterative feedback and thus perform the required Neumann series solving the corresponding equation in the analog domain at the speed of light. The solution provided by the metasurface in simulations effectively solves the problem of interest and is very close to its ideal counterpart. The designed metagrating is fabricated using Si-on-sapphire substrate to create a hardware representation of the predefined kernel. The feedback system is composed of a thin gold mirror on top of a SiO_2 spacer layer. We optically characterize the output for different input signals showing good agreement with the ideal simulated response. Next, we use the spectral data to retrieve the experimental solution and compare it to its ideal counterpart with the chosen kernel, demonstrating a close match at a slightly blue-shifted wavelength $\lambda = 699$ nm. Visible-wavelength operation enables a highly compact, ultra-thin device that can be

interrogated from free-space, resulting in high processing speed and the possibility of on-chip integration.

Finally, in Chapter 5 we apply the insights gained on grating design to a nanophotonic light trapping scheme in the near-IR wavelength range to boost the efficiency of a high-performance GaInP/GaAs/Si triple-junction solar cell. A silver diffractive back reflector at the bottom of the cell is designed to redirect incoming light to diffraction angles outside the escape cone in a wavelength range where light is poorly absorbed by the Si sub-cell. The back-reflector consists of a hexagonal array of silver nanodisks embedded in a PMMA layer and in direct contact with the Si absorber. A simple interference model explains the physics governing reduced reflection to the 0^{th} diffraction order and further provides guidelines on how to optimize the structural parameters. Next, the impact of the optimized design on the absorption in a thick Si slab is evaluated, highlighting an increase over a planar back–reflector and over the design that is featured in the current record cell. Large-area Si bottom cells and full two–terminal triple–junction cells are patterned via SCIL and characterized optically and electronically. The experimental external quantum efficiencies and one-sun current–voltage characteristics demonstrate a +1.8% efficiency improvement over the planar reference for complete triple-junction solar cells and increased EQE spectra for the single junction Si sub-cells over the current world record design. Furthermore, the cells are not damaged or electronically degraded by the back-reflector fabrication process, further proving the applicability of SCIL to high-efficiency devices. The results presented show a nanophotonic light trapping scheme based on gratings that can enhance the performances of cells where more traditional random texture strategies are not possible. Furthermore, the EQE data on Si sub-cells and the successful implementation on full triple-junction solar cells support the possibility of GaInP/GaAs/Si cells featuring a patterned back-reflector with power conversion efficiencies above the current world record.

Altogether, this thesis provides new insights into the field of optical analog processing via metasurfaces and metamaterials at visible wavelengths, demonstrating its potential with structures that can realistically be combined with existing CMOS technology. We present experimental demonstrations of different metasurface-based platforms that perform image processing tasks or solve complex mathematical problems. These results could inspire the next computing paradigm, featuring a synergy between digital and analog processing.

SAMENVATTING

Meta-oppervlakken voor analoge optische procesbewerkingen
Hoge-index diëlektrische meta-oppervlakken die wiskundige berekeningen uitvoeren

De groeiende behoefte aan efficiënt computergebruik in de wereld heeft onderzoekers uit verschillende onderzoeksgebieden ertoe aangezet om alternatieven te verkennen op het huidige digitale computerparadigma. De rekensnelheid en energie-efficiëntie van standaardelektronica zijn de beperkende factoren geworden voor de introductie van innovatieve toepassingen in ons dagelijks leven zoals kunstmatige intelligentie, 'machine learning' en 'computer vision'. Beeldverwerking vormt de kern van veel van deze technologieën en wordt doorgaans digitaal uitgevoerd met behulp van geïntegreerde elektronische schakelingen en algoritmen. Dit brengt fundamentele snelheidsbeperkingen en een aanzienlijk stroomverbruik met zich mee. Deze processen kunnen ook direct en met weinig vermogen worden uitgevoerd door analoge Fourier-optica. Echter, dit vereist omvangrijke optische componenten.

In deze context krijgen analoge computerberekeningen weer veel aandacht als aanvulling op traditionele architecturen. In het bijzonder hebben de recente vorderingen op het gebied van meta-materialen en meta-oppervlakken de deur geopend voor volledig optische computerstrategieën. Dit komt door de mogelijkheid om optische velden op extreme manieren te manipuleren op afstanden korter dan de golflengte van het licht. Meta-oppervlakken voor analoge procesverwerking zouden profiteren van de snelheid en het lage stroomverbruik van optica, en ze maken het mogelijk om optische en elektronische gegevensverwerking tegelijkertijd uit te voeren in een hybride chip.

Het idee om licht te gebruiken om specifieke computertaken uit te besteden heeft verschillende voordelen. Ten eerste is er een duidelijke verhoging van de verwerkingssnelheid, aangezien de berekening wordt uitgevoerd met de snelheid van het licht dat door meta-materialen reist met typische afmetingen die kleiner zijn dan, of vergelijkbaar zijn met de golflengte van de procesbewerking. Ook maakt het verwerken van signalen in het optische domein massale parallellisatie mogelijk en kan eventueel onnodige analoog-naar-digitaal conversie vermeden worden. Er kunnen bijvoorbeeld verschillende beeldverwerkingstaken worden uitgevoerd voordat het beeld in pixels wordt omgezet, waarbij gebruik wordt gemaakt van de mogelijkheid om de hoekrespons van meta-oppervlakken te manipuleren en zo onmiddellijk een wiskundige bewerking te geven aan de ruimtelijke inhoud van een ingangssignaal (het beeld). Ten slotte kunnen meta-apparaten voor procesbewerking passief zijn, waardoor het energieverbruik extreem laag is.

Het werk dat in dit proefschrift wordt gepresenteerd helpt om het gebied van volledig optische procesverwerking via meta-oppervlakken tot stand te brengen door verschillende platforms te tonen die compact zijn en op een chip passen. De mogelijkheid van

integratie in standaard computerchip-technologie (CMOS) biedt interessante mogelijkheden voor hybride analoog-digitale procesverwerking, die werkt met hogere datasnelheden en een lager stroomverbruik.

In Hoofdstuk 2 demonstreren we voor het eerst een ontwerp van silicium meta-oppervlakken die op een volledig analoge manier wiskundige bewerkingen kunnen uitvoeren en randen detecteren in optische beelden. Het belangrijkste inzicht van dit werk is dat optische Fano-resonanties in een compacte geometrie van silicium nano-roosters een diversiteit aan bewerkingen mogelijk maakt in het Fourier-domein die zowel invloed heeft op de amplitude als de fase van het licht. We beschrijven hoe de plaats-afhankelijke dispersierelatie van het meta-oppervlak kan worden gemanipuleerd door controle over de lekkende golfgeleider-modi en de gerelateerde asymmetrie en lijnbreedte van Fano-resonanties. Op basis hiervan presenteren we een ontwerp voor meta-oppervlakken die de eerste- of tweede-orde afgeleide uitvoeren. We demonstreren experimenteel de tweede-afgeleide operatie op tweekleurige- en grijsschaal-afbeeldingen, waarmee we direct de potentie van volledig optische randdetectie laten zien. Een uniek voordeel van onze silicium meta-oppervlak-geometrie is dat deze werkt bij een grote numerieke apertuur van 0.35, wat meer dan 25 keer hoger is dan eerder onderzochte mogelijkheden. Dit houdt in dat het gemakkelijk kan worden geïntegreerd in praktische beeldvormingssystemen. Bovendien biedt het ook een aanzienlijk verbeterde efficiëntie, wat zorgt voor een bijna ideale transmissie voor afgeleide operaties met behulp van passieve apparaten. Ten slotte breiden we het formalisme uit tot 2D-verwerkingen bij gebruik van een ongepolariseerde lichtbron. Geoptimaliseerde ontwerpen worden gepresenteerd die zowel even- als oneven-orde ruimtelijke afgeleiden quasi-isotroop kunnen uitvoeren en randdetectie in alle richtingen wordt gedemonstreerd.

Hoofdstuk 3 beschrijft een elektrisch bestuurbaar meta-oppervlak voor optische procesverwerking. Om dit te bereiken is een meta-oppervlak nodig dat lekkende golf-geleider-modi ondersteunt die langs het oppervlak van een mono-atomaire laag WS_2 lopen, waarbij de elektrostatische potentiaal in het WS_2 extern gecontroleerd kan worden. Het effect van het uitdoven van de aangeslagen resonantie van de mono-atomaire laag door de externe potentiaal gebruiken we om de procesbewerking van het meta-oppervlak te veranderen. Dit concept wordt gebruikt om een schakelbaar, plaats-af-hankelijk Fourier-filter te ontwerpen. In het bijzonder fungeert het apparaat als een hoogdoorlaatfilter dat kan worden verstoord door de aanwezigheid (of afwezigheid) van excitonen in de mono-atomaire laag WS_2. Het optimale ontwerp bereikt een numerieke apertuur van $0,2$ en een transmissie van bijna $0,8$ bij de maximale verwerkte k-vector. Numerieke tests op een geoptimaliseerd ontwerp tonen duidelijk betrouwbare randfiltering aan die kan worden in- en uitgeschakeld voor licht met een golflengte van $\lambda = 626$ nm en $\lambda = 620$ nm. Vervolgens fabriceren we een chip die verschillende apparaten bevat die elk zijn samengesteld uit een reeks TiO_x nanodraden op een mono-atomaire laag WS_2. De elektrostatische potentiaal in het WS_2 worden gecontroleerd via een MOSFET-achtige configuratie. Optische karakterisering onder een toegepaste externe potentiaal toont modulatie aan van de Fano-resonantie in de reflectie-meting volgens dezelfde trends als de simulaties laten zien. Dit demonstreert de potentie van het hybride platform van meta-oppervlak met WS_2 mono-atomaire laag dat we voorstellen. De resultaten zijn een belangrijke eerste stap voor optische procesverwerking in meta-oppervlakken met functionaliteiten die

tijdens gebruik actief kunnen worden afgestemd.

In Hoofdstuk 4 presenteren we een ultradunne silicium architectuur die is gebaseerd op meta-oppervlakken en kan worden gebruikt voor analoge procesverwerking. Dit platform is in staat om Fredholm-integraalvergelijkingen van de tweede soort op te lossen met behulp van zichtbaar licht. Met behulp van topologie-optimalisatie implementeren we een specifieke verstrooiingsmatrix die een voorgeschreven nulruimte (Engels: kernel) synthetiseert in een silicium meta-rooster. Om de algemeenheid van deze techniek aan te tonen, stellen we als optimalisatiedoel een willekeurige passieve en wederkerige kernel. Het optimale ontwerp verschaft een verstrooiingsmatrix die zeer dicht bij de gewenste matrix ligt bij de optimale golflengte van $\lambda = 706$ nm. Vervolgens wordt een semitransparante spiegel in het ontwerp opgenomen om voldoende feedback te geven en zo de vereiste Neumann-reeksen uit te voeren om de overeenkomstige vergelijking in het analoge domein met de snelheid van het licht op te lossen. De oplossing die door het meta-oppervlak in simulaties wordt geboden, lost effectief het probleem op en ligt heel dicht bij zijn ideale tegenhanger. Het ontworpen meta-rooster is gefabriceerd uit een silicium-op-saffiersubstraat om de vooraf gedefinieerde kernel te creëren. Het feedbacksysteem bestaat uit een dunne gouden spiegel bovenop een SiO_2-separatielaag. We karakteriseren het optische uitgangssignaal voor verschillende invoersignalen, welke een goede overeenkomst vertonen met de ideale gesimuleerde respons. Vervolgens gebruiken we de spectrale gegevens om de experimentele oplossing op te halen en te vergelijken met zijn ideale tegenhanger van de gekozen kernel, wat een nauwe overeenkomst aantoont bij een licht blauw-verschoven golflengte van $\lambda = 699$ nm. Metingen met zichtbaar licht maken een zeer compact, ultradun apparaat mogelijk dat draadloos kan worden uitgelezen. Dit resulteert in een hoge verwerkingssnelheid van de berekening en de mogelijkheid van integratie op een chip.

Ten slotte passen we in Hoofdstuk 5 de inzichten die zijn verkregen over het ontwerp van meta-roosters toe op een systeem dat het invangen van licht mogelijk maakt in het nabij-infrarood-golflengtebereik om het rendement van een hoogwaardige GaInP/GaAs/Si heterojunctie zonnecel te verhogen. Een zilveren diffractie-spiegel aan de onderkant van de zonnecel is ontworpen om binnenkomend licht te verstrooien naar diffractiehoeken buiten de ontsnappingskegel in een golflengtebereik waar licht slecht wordt geabsorbeerd door de Si-subcel. De diffractie-spiegel bestaat uit een hexagonale reeks zilveren nanoschijven ingebed in een PMMA-laag die in direct contact is met de Si-absorber. Een eenvoudig interferentiemodel verklaart de fysica die de verminderde reflectie voor de nulde-orde diffractie veroorzaakt en geeft richtlijnen voor het verder optimaliseren van de structurele parameters. Vervolgens wordt de impact van het geoptimaliseerde ontwerp op de absorptie in een dikke Si-laag geëvalueerd, waarbij de toename wordt vergeleken met die voor een vlakke spiegel en voor het ontwerp van de huidige record-zonnecel. Si-subcellen met een groot oppervlak en volledige twee-terminale tripel-junctiecellen worden via SCIL van een patroon voorzien, en optisch en elektronisch gekarakteriseerd. De experimentele externe kwantumefficiëntie (EQE) en stroomspanningskarakteristieken onder één-zon belichting tonen een redementsverbetering aan van +1,8% ten opzichte van de vlakke referentie voor volledige tripel-junctie zonnecellen en verhoogde EQE-spectra voor de single-junctie Si-subcellen ten opzichte van huidige wereldrecord ontwerp. Bovendien worden de cellen niet beschadigd of elektro-

nisch beschadigd door het fabricageproces van de diffractie-spiegel, wat de toepasbaarheid van SCIL op zeer efficiënte apparaten verder aantoont. De gepresenteerde resultaten tonen een methode die het invangen van licht mogelijk maakt op basis van metaroosters die de prestaties van zonnecellen kunnen verbeteren waar meer traditionele willekeurige textuurstrategieën niet mogelijk zijn. Bovendien ondersteunen de EQE-gegevens van Si-subcellen en de succesvolle implementatie in volledige tripel-junctie-zonnecellen de mogelijkheid van GaInP/GaAs/Si-cellen met een diffractie-spiegel met een stroomconversie-efficiëntie die hoger is dan het huidige wereldrecord.

Samenvattend biedt dit proefschrift nieuwe inzichten op het gebied van optische analoge procesverwerking via meta-oppervlakken en meta-materialen bij zichtbare golflengten, waarbij de potentie ervan wordt aangetoond met structuren die realistisch kunnen worden gecombineerd met bestaande CMOS-technologie. We presenteren experimentele demonstraties van verschillende platforms die op meta-oppervlakken zijn gebaseerd die beeldverwerkingstaken uitvoeren of complexe wiskundige problemen oplossen. Deze resultaten zouden het volgende computerparadigma kunnen inspireren, met een synergie tussen digitale en analoge verwerking.

SOMMARIO

Meta-superfici per elaborazione analogica ottica
Meta-superfici con dielettrici ad alto indice di rifrazione che eseguono operazioni matematiche

La domanda crescente di efficienza di elaborazione numerica di dati ed equazioni in svariati campi applicativi e di ricerca fondamentale suggerisce l'esplorazione di percorsi alternativi all'attuale paradigma di *digital computing*. La velocità di elaborazione e l'efficienza energetica dell'elettronica standard sono diventati fattori limitanti per le nuove dirompenti tecnologie che entrano nella nostra vita quotidiana, tra cui l'intelligenza artificiale (*artificial intelligence,* AI), l'apprendimento automatico (*machine learning*) e la visione artificiale (*computer vision*). L'elaborazione delle immagini è al centro di molte di queste tecnologie e viene in genere eseguita digitalmente utilizzando circuiti elettronici integrati e algoritmi. Ciò implica fondamentali limitazioni in termini di velocità, e un consumo energetico significativo. Questi processi possono anche essere eseguiti istantaneamente, a bassa potenza, ed in maniera analogica sfruttando concetti di ottica di Fourier. Tuttavia, ciò richiede componenti ottici ingombranti.

In questo contesto, è tornata a svilupparsi la ricerca sulla computazione analogica, riguadagnando una notevole attenzione come percorso complementare alle architetture tradizionali. In particolare, i recenti progressi nel campo dei metamateriali e delle metasuperfici hanno aperto nuove opportunità per schemi di computazione completamente ottici, data la possibilità di modellare i campi elettromagnetici in modi estremi in spessori minori della lunghezza d'onda. Le metasuperfici per computazione analogica traggono vantaggio dalla velocità e dal basso consumo energetico dell'ottica, essendo allo stesso tempo una tecnologia integrabile su chip che consente l'elaborazione ibrida (ottica ed elettronica) di dati su un singolo chip.

L'idea di utilizzare la luce per eseguire specifici tipi di computazione presenta numerosi vantaggi. In primo luogo, c'è un chiaro incremento della velocità di elaborazione poiché il calcolo viene eseguito alla velocità della luce che viaggia attraverso metamateriali con dimensioni tipiche inferiori o paragonabili alla lunghezza d'onda dell'operazione. Inoltre, l'elaborazione dei segnali nel dominio ottico consente parallelizzazione e può potenzialmente evitare inutili conversioni da analogico a digitale. Ad esempio, è possibile eseguire diverse funzioni di elaborazione delle immagini prima che l'immagine stessa venga discretizzata in pixel, basandosi sulla possibilità di ingegnerizzare la risposta angolare delle metasuperfici e quindi impartire istantaneamente un'operazione matematica al contenuto spaziale di un segnale di ingresso. Infine, i meta-dispositivi per computazione analogica possono essere passivi, il che implica un consumo energetico estremamente basso.

Il lavoro presentato in questa tesi contribuisce a definire il campo di ricerca della computazione ottica tramite metasuperfici, mostrando diverse piattaforme compatte

e implementabili su chip. La possibilità di integrazione nella tecnologia CMOS, a sua volta, offre interessanti opportunità per la computazione ibrida analogico-digitale che opera a velocità più elevate e con un consumo di energia inferiore.

Nel Capitolo 2, dimostriamo per la prima volta che metasuperfici ottiche di silicio possono eseguire operazioni matematiche e rilevamento ottico dei bordi di un'immagine in modo completamente analogico. La chiave del nostro lavoro è che le risonanze di Fano in un reticolo di nano-fili di silicio permettono l'esecuzione di operazioni nel dominio di Fourier, agendo sia sull'ampiezza che sulla fase del campo elettromagnetico incidente. Descriviamo come ottimizzare la dispersione spaziale della metasuperficie manipolando i suoi modi quasi-guidati e la relativa asimmetria nella risonanza di Fano e larghezza di linea. Quindi, presentiamo geometrie di metasuperfici che eseguono differenziazione spaziale del primo e del secondo ordine. Dimostriamo sperimentalmente l'operazione di derivata seconda su immagini di input a due toni e in scala di grigi, mostrando direttamente il potenziale del rilevamento-bordi completamente ottico. Un vantaggio della metasuperficie in silicio presenatata è che opera con un'ampia apertura numerica pari a 0.35, più di 25 volte superiore rispetto agli schemi precedentemente esplorati, questo implica la possibilità di integrazione in sistemi ottici tradizionali (e.g. fotocamere). Inoltre, offre anche un'efficienza ampiamente migliorata, garantendo una trasmissione quasi ideale per la differenziazione utilizzando dispositivi passivi. Infine, estendiamo il formalismo alle operazioni bi-dimensionali e all'illuminazione con luce non polarizzata. Vengono presentate geometrie ottimizzate che eseguono differenziazione spaziale quasi-isotropa di ordine pari e dispari e dimostrano numericamente il rilevamento di bordi orientati in tutte le direzioni.

Il capitolo 3 descrive una metasuperficie per elaborazione ottica controllabile elettricamente. A questo fine, una metasuperficie capace di sostenere modi quasi-guidati lungo la sua superficie è accoppiata a un monostrato di WS_2 controllato elettricamente tramite gate. L'impatto della soppressione della risonanza eccitonica sulla risposta ottica del monostrato TMD è sfruttato per alterare la funzione di trasferimento della metasuperficie. Questa logica viene utilizzata per progettare un filtro spaziale di Fourier commutabile. In particolare, il dispositivo si comporta come un filtro passa-alto che può essere perturbato dalla presenza (o assenza) di eccitoni nel monostrato di WS_2. La geometria ottimale raggiunge un'apertura numerica di 0.2 e una trasmissione vicina a 0.8 al massimo vettore d'onda k elaborato. Test numerici su un design ottimizzato dimostrano un affidabile rilevamento dei bordi che può essere attivato e disattivato alle lunghezze d'onda di illuminazione λ = 626 nm e λ = 620 nm. Successivamente, fabbrichiamo un chip contenente diversi dispositivi, ciascuno composto da un reticolo di nanofili TiO_x su un monostrato di WS_2 controllato elettricamente tramite gate in una configurazione simile ad un MOSFET. La caratterizzazione ottica al variare del voltaggio esterno applicato mostra una modulazione della risonanza di Fano in riflessione che segue lo stesso andamento delle simulazioni, mostrando il potenziale della piattaforma ibrida metasuperficie–2D-TMD. I risultati presenati sono un primo passo importante per i dispositivi basati su metasuperfici per computazione ottica con funzionalità che possono essere modulate attivamente durante il funzionamento.

Nel Capitolo 4, presentiamo una piattaforma ultrasottile basata su una metasuperficie di silicio che è in grado di risolvere equazioni integrali di Fredholm del secondo

tipo usando luce visibile. Tramite l'ottimizzazione della topologia della cella primitiva, è possibile implementare un meta-reticolo di silicio con una matrice di scattering tale da sintetizzare un kernel specifico. Per dimostrare la generalità di questa tecnica, abbiamo impostato come obiettivo dell'ottimizzazione un kernel casuale, passivo e reciproco. Il design ottimale fornisce una matrice di scattering molto vicina a quella desiderata alla lunghezza d'onda desiderata $\lambda = 706$ nm. Quindi, uno specchio semitrasparente viene incorporato nel campione per fornire un feedback iterativo adeguato e quindi eseguire la serie di Neumann necessaria per risolvere l'equazione corrispondente, nel dominio analogico e alla velocità della luce. La soluzione fornita dalla metasuperficie in simulazione risolve efficacemente il problema di interesse ed è molto vicina alla controparte ideale. Il meta-reticolo progettato viene fabbricato su un substrato di silicio su zaffiro per creare una rappresentazione hardware del kernel predefinito. Il sistema di feedback è composto da un sottile specchio d'oro sopra uno strato distanziatore di SiO_2. L'output per diversi segnali di ingresso viene caratterizzato otticamente mostrando un buon accordo con la risposta simulata ideale. In seguito, utilizziamo i dati spettrali per recuperare la soluzione sperimentale e confrontarla con la sua controparte ideale corrispondente al kernel scelto, dimostrando una stretta corrispondenza ad una lunghezza d'onda leggermente spostata verso il blu $\lambda = 699$ nm. Il funzionamento ad una lunghezza d'onda nel visibile consente un dispositivo estremamente compatto e ultrasottile che può essere interrogato con luce in spazio libero, con conseguente elevata velocità di elaborazione e possibilità di integrazione su chip.

Infine, nel capitolo 5 applichiamo le conoscenze acquisite sul design di reticoli di diffrazione ad uno schema di intrappolamento della luce nel vicino infrarosso per aumentare l'efficienza di una cella solare a tripla giunzione GaInP/GaAs/Si ad alte prestazioni . Un reticolo diffrattivo riflettore d'argento posto sulla superficie inferiore della cella è progettato per reindirizzare la luce in ingresso verso angoli di diffrazione maggiori dell'angolo critico in un intervallo di lunghezze d'onda in cui la luce è scarsamente assorbita dalla sotto-cella di silicio. Il reticolo è costituito da una lattice esagonale di nano-dischi d'argento incorporati in uno strato di PMMA e a diretto contatto con l'assorbitore di silicio. Un semplice modello di interferenza spiega la fisica che governa la soppressione della riflessione verso l'ordine zero di diffrazione e fornisce inoltre linee guida su come ottimizzare i parametri strutturali. Successivamente, viene valutato l'impatto del design ottimizzato sull'assorbimento in una lastra di silicio spesso, evidenziando un incremento rispetto ad un riflettore planare e rispetto al design presente nella cella solare che detiene tuttora il record di efficienza. Sotto-celle di silicio e celle complete a tripla giunzione a due terminali sono fabbricate tramite SCIL su una ampia superficie e seguentemente caratterizzate otticamente ed elettronicamente. Le efficienza quantica esterna (EQE) sperimentale e la caratteristica di corrente-tensione con illuminazione AM 1.5 dimostrano un miglioramento dell'efficienza pari a +1,8% rispetto alla cella di riferimento planare per celle solari complete a tripla giunzione e spettri EQE migliorati per le sotto-celle di silicio a giunzione singola rispetto al design della cella record. Inoltre, le celle non vengono danneggiate o degradate elettronicamente dal processo di fabbricazione del riflettore posteriore, dimostrando ulteriormente l'applicabilità di SCIL a dispositivi ad alta efficienza. I risultati presentati mostrano uno schema di cattura della luce nanofotonico basato su reticoli in grado di migliorare le prestazioni di celle in cui

non sono possibili strategie più tradizionali. Inoltre, gli spettri di EQE sulle sottocelle di Si e la riuscita implementazione su celle solari a tripla giunzione supportano la possibilità di realizzare celle GaInP/GaAs/Si dotate di un riflettore posteriore ottimizzato con efficienze superiori all'attuale record.

Complessivamente, il presente lavoro di tesi fornisce nuove conoscenze nel campo dell'elaborazione analogica ottica tramite metasuperfici e metamateriali che operano a lunghezze d'onda visibili, dimostrandone il potenziale con strutture che possono essere realisticamente combinate con la tecnologia CMOS esistente. Vengono altresì presentate dimostrazioni sperimentali di diverse piattaforme basate su metasuperfici che eseguono attività di elaborazione delle immagini o risolvono complessi problemi matematici. Questi risultati potrebbero ispirare il prossimo paradigma di computazione, caratterizzato da una sinergia tra elaborazione digitale e analogica.

LIST OF PUBLICATIONS AND AUTHOR CONTRIBUTIONS

Chapter 2:

- **A. Cordaro**, H. Kwon, D. Sounas, A.F. Koenderink, A. Alù, and A. Polman, *High-index dielectric metasurfaces performing mathematical operations*, Nano Letters **19**, 8418 (2019).

  A.C. designed and fabricated Si metasurface samples, performed numerical simulations and optical measurements. A.C., H.K., and D.S. performed theoretical analyses. A.F.K., A.A., and A.P. supervised the project. All authors contributed to the analysis and writing of the paper.

- H. Kwon, **A. Cordaro**, D. Sounas, A. Polman, and A. Alù, *Dual-polarization analog 2D image processing with nonlocal metasurfaces*, ACS Photonics **7**, 1799 (2020).

  H.K. performed numerical simulations, H.K., A.C. and D.S. performed theoretical analyses. A.A. and A.P. supervised the project. All authors contributed to the analysis and writing of the paper.

- H. Kwon, D. Sounas, **A. Cordaro**, A. Polman, and A. Alù, *Nonlocal metasurfaces for optical signal processing*, Physical Review Letters **121**, 173004 (2018).

  H.K. performed numerical simulations, H.K., A.C. and D.S. performed theoretical analyses. A.A. and A.P. supervised the project. All authors contributed to the analysis and writing of the paper.

Chapter 3:

- **A. Cordaro**, L. Guarneri, A. Alù, J. van de Groep, and A. Polman, *Two-dimensional WS_2–based switchable computing metasurfaces*, (in preparation).

  A.C. designed and fabricated the samples, performed numerical simulations and optical measurements. L.G. and A.C. performed low-temperature optical measurements. J.v.d.G, A.A., and A.P. supervised the project. All authors contributed to the analysis and writing of the paper.

Chapter 4:

- **A. Cordaro**, B. Edwards, V. Nikkhah, A. Alù, N. Engheta, and A. Polman, *Solving integral equations in free-space with inverse-designed ultrathin optical metagratings*, (submitted).

  A.C. designed and fabricated the samples, performed numerical simulations and optical measurements. A.C., B.E. and V.N. performed theoretical analyses A.A., N.E. and A.P. supervised the project. All authors contributed to the analysis and writing of the paper.

Chapter 5:

- **A. Cordaro**, R. Müller, S. W. Tabernig, N. Tucher, H. Hauser, O. Höhn, B. Bläsi, and A. Polman *Nano-patterned back-reflector for enhanced light management in III–V-on-silicon solar cells*, (in preparation).

  A.C. performed numerical simulations, designed the back-reflector and retrieved OPTOS matrices. N.T. performed OPTOS calculations. Si sub-cells and triple-junction cells are fabricated at Fraunhofer ISE (R.M.). A.C. and S.W.T. fabricated the Ag back-reflector on the samples. Cell performances are tested at Fraunhofer ISE. B.B and A.P. supervised the project.

OTHER PUBLICATIONS

1. S. W. Tabernig, L. Yuan, **A. Cordaro**, Z. Li Teh, Y. Gao, R. Patterson, A. Pusch, S. Huang, and A. Polman, *Optically resonant bulk heterojunction PbS quantum dot solar cell*, (submitted).

2. M. Cotrufo, **A. Cordaro**, A. Polman, and A. Alù, *Nonlinearity-induced nonreciprocity in passive silicon gratings supporting quasi-bound states in the continuum*, (in preparation).

3. L.A. Muscarella, **A. Cordaro**, G. Krause, D. Pal, G. Grimaldi, D. Langhorst, A. Callies, B. Bläsi, O. Höhn, F. A. Koenderink, A. Polman, and B. Ehrler, *Substrate conformal imprint lithography for light management in perovskite-based LEDs*, (in preparation).

4. M. D. Wobben, M. Valenti, Y. Bleiji, **A. Cordaro**, S. W. Tabernig, M. Aarts, R. D. Buijs, S.R.K. Rodriguez, A. Polman, and E. Alarcón Lladó, *Plasmonic indium lattices fabricated via electrochemical deposition*, (in preparation).

5. Y. Bleiji, M. Dieperink, **A. Cordaro**, S. W. Tabernig, A. Polman, and E. Alarcón Lladó, *Bottom-up filling of nanosized trenches with silver and copper to fabricate transparent conducting electrodes*, (in preparation).

6. F. Uleman, V. Neder, **A. Cordaro**, A. Alù, and A. Polman, *Resonant metagratings for spectral and angular control of light for colored rooftop photovoltaics*, ACS Applied Energy Materials **4**, 3150 (2020).

7. **A. Cordaro**, J. van de Groep , S. Raza , E. F. Pecora, F. Priolo, and M. L. Brongersma, *Antireflection high–index metasurfaces combining Mie and Fabry-Pèrot resonances*, ACS Photonics **6**, 453 (2019).

8. E. F. Pecora, **A. Cordaro**, P. G. Kik, and M. L. Brongersma, *Broadband antireflection coatings employing multiresonant dielectric metasurfaces*, ACS Photonics **5**, 4456 (2018).

9. **C.E.A. Cordaro**, G. Piccitto, and F. Priolo, *Quantum plasmonic waveguides: Au nanowires*, Eur. Phys. J. Plus **132**, 453 (2017).

PUBLICATIONS IN CONFERENCE PROCEEDINGS

1. **A. Cordaro**, B. Edwards, V. Nikkhah, A. Alù, N. Engheta, and A. Polman, *Solving integral equations with inverse-designed metagratings at optical wavelengths*, 2021 Conference on Lasers and Electro-Optics (CLEO), San Jose, CA, 2021, pp. 1-2.

2. **A. Cordaro**, N. Tucher, S. W. Tabernig, H. Hauser, O. Hoehn, R. Müller, B. Bläsi, and A. Polman, *Plasmonic and Mie scattering in nanopatterned back reflectors for III–V-on-silicon solar cells*, Proc. SPIE 11366, Photonics for Solar Energy Systems VIII, 1136607 (2020).

3. **A. Cordaro**, B. Edwards, V. Nikkhah, A. Alù, A. Polman, and N. Engheta, *Inverse designed metagratings for far-field integral equations solving*, 2020 Conference on Lasers and Electro-Optics (CLEO), San Jose, CA, 2020, pp. 1-2.

4. **A. Cordaro**, H. Kwon, D. Sounas, Femius Koenderink, A. Polman, and A. Alù, *Dielectric metasurfaces performing all-analog computing*, 2019 Conference on Lasers and Electro-Optics (CLEO), San Jose, CA, 2019, pp. 1-2.

5. S. W. Tabernig, Z. Li Teh, **A. Cordaro**, R. Patterson, G. Conibeer, S. Huang, and A. Polman, *Light management for absorption enhancement in PbS quantum dot solar cells*, Proceedings of the Asia Pacific Solar Research Conference 2019.

6. **A. Cordaro**, H. Kwon, D. Sounas, A. Polman, and A. Alù, *Non-local computing metasurfaces performing mathematical operations*, 2018 Conference on Lasers and Electro-Optics (CLEO), San Jose, CA, 2018, pp. 1-2.

PATENT

1. **C.E.A. Cordaro**, E. F. Pecora, M. L. Brongersma, and J. Van de Groep, *Broadband, polarization-independent, omnidirectional, metamaterial-based antireflection coating*, Worldwide patent applications, US Patent WO2018175874A1.

ACKNOWLEDGMENTS

This is the final and most important part of the thesis. In the following, I would like to thank all the people that supported and helped me during this tough but exciting journey.

I want to deeply thank Albert for being more than just an excellent supervisor. From an academic perspective, he is continuously providing me with great opportunities, giving me the chance to interact with top scientists from all over the world. In the most stressful moments in the lab, his intrinsic optimism has often rescued me, teaching me to always seek the silver lining. Far more than that, Albert has simply been a reference point in my life for the last 5 years. He has always been present and carefully helpful in the toughest moments, showing me what really means to care and building a relationship based on reciprocal trust that is going to last.

Next, I would like to thank my second advisor Andrea for being such a crucial part of this adventure. The period I spent in Austin within his group has been a turning point for me and shaped the work of the entire Ph.D. His excitement about our ideas and the way he constantly challenged me have been an incredible drive. At the same time, he has constantly supported my growth always making time to chat and give me honest and sharp advice. *Grazie!*

Since my time at Stanford, Jorik has been a good friend and an unbiased source of advice. His critical and rational thinking coupled with careful attention to personal matters has guided me through key decisions. I am excited to see the group of talented kids he is putting together and I hope we can work in the future on the next new exciting ideas. Moreover, I am really grateful for the time he spent reading carefully this thesis, providing critical and essential comments that certainly improved it.

This work would have never been possible without some outstanding collaborators. Working with Femius has been greatly instructive and fun. I truly appreciate his willingness to share his deep knowledge about Photonics as well as to discuss science in a deep and very sincere way. Later in my Ph.D. I was lucky enough to work with Nader. He is one of the most brilliant and, at the same time, most humble scientists I met. Thanks for hosting me at Penn and for sharing with us one of the most exciting projects. Thanks to Ralph, Benedikt, Hubert, and Nico for the 5-years effort on the back-reflector project.

Furthermore, I would like to thank my first mentors prof. Francesco Priolo and prof. Giuseppe Angilella who helped shape my path from the very beginning (and still do). Among other people I met at SSC, thanks to Giampi and Bruno for visiting me in Amsterdam and for still giving me sincere advice. Thanks to the Alumni board and to the Zürich folks, it was great to catch up.

Special thanks go to the Photonic Materials group! Working with such a fantastic group has made all the difference and I am grateful for all the unplanned outings, for striving to keep the group close and social even during the pandemic, and simply for making my time here truly *gezellig!* Thanks to Tom, Magda, and Verena. Sharing this

path with them from the very beginning to the end has been awesome and I am thrilled to look back at what we have achieved together as well as to see how their bright future is already unfolding. Thanks to Matthias and his cheerful randomness that keeps everyone happy. Thanks to Stefan, my first cleanroom initiate, who has shared its pain with me without compromising on humor and funny moments. Thanks to Nika and Evelijn, the young-&-promising side of the group, for always being willing to take care of planning social events, trips, gifts, and much more. It is clear that the baton has passed to the next generation and it is in very good hands. Thanks to Kelly for all the fun activities, dinners, pizza nights, and also for teaching me new tricks in the lab. Thanks to Nick for his inextinguishable and contagious good mood as well as for his willingness to help with tough theoretical questions. I would like to thank the present and past master's students and interns that kept the group's vibe young and vibrant. Thanks to Hannah, Hollie, Daphne, Floris, and Joris.

My time in the U.S. has been very exciting thanks to the awesome people in Andrea's and Nader's groups. I want to thank Hoyeong and Dimitrios for their crucial help in setting up the theory for this work but also for the trip to the White Sands, Austin City Limits, the GP of The Americas, and the countless cheerful moments together. Let me also mention a secret group of scientists performing only cutting-edge research: Yarden, Michele, and Sander, thanks for all the advice and good times in Austin and New York. I would also like to thank Brian and Vahid who shared the efforts in developing the integral solver as well as many joyful moments together. Dimitrios (T.) and Miguel, thanks for all the fun I had in such a brief time in Philadelphia.

I can confidently state that none of the experimental work would have been possible without Bob, Dimitry, Andries, Igor, Hans, and Dion. The passion that drives them is impressive and the quality and attention to details of their work are beyond what is expected. Other than discussing the limits of nano-fabrication, I also undoubtedly enjoyed sharing a sip of amaro in a glass beaker while discussing Formula 1.

Thanks to the LMPV group leaders for creating such a nice atmosphere at AMOLF and for always being available for advice.

Let me also thank all the people at AMOLF who make it such a magical place: Marko, Christiaan, Hugo and Ruslan, Julia, Carolyn, Agustin, Lukas, Christian, Harshal, Jenny, John, Kevin, Lucie, Moritz (senior), Moritz (junior), Nikhil, Annemarie, Ilan, Eitan, Nasim, Sven, Benjamin, Gianluca, Hongyu, Susan, Imme, Yorick, Daphne, Ariane, Arno, Jesse, and Alex. With all of them, I have shared legendary and amazingly-planned parties (e.g. all of Lukas' parties) as well as smaller but equally fun events in the cozy DUWO rooms (e.g. Jenny's random parties and Carolyn's traditional glühwein nights). All the light-hearted chats at the coffee corner, AMOLF borrels, and random nights out made these years very special. As usual, anywhere abroad is full of Italian folks and they always find each other. Thanks to Alessandro, Marco, Giorgio, Giulia, Federica (B.), Piero, Vanessa, Lorenzo, and Laura for making me feel closer to home, for sharing all the emotions of the last Euro cup, and for taking control over the music at each party. I would also like to thank Gianluca who welcomed me in Amsterdam more than 5 years ago. My time in Botterstraat was one of the best and most fun periods ever. Thanks to Greta for actually providing me with a room (an extremely valuable asset in Amsterdam) and for making sure I had a reference point from *Piazza* in Amsterdam. I also want to thank my latest

Sicilian lab mate Ludovica for sharing with me the long evenings with the cryo stage but also some beers.

The second COVID lock-down was undoubtedly one of the most distressing periods of the last years. I am very thankful to Robin, Karol, Jente, René, Cesare, and Alexander for easing this burden by means of dinners at each other's places, board games nights, and lit up discussions about (mainly Italian) politics. During the same period, I found out that Federica had moved to Amsterdam. I really loved our dinners, random sleep-overs, and traditional Sunday lunches. These made me feel at home and gave me a sense of normality when the times were actually crazy.

Next, I would like to acknowledge all the new friends I made during my frequent escapes to Rome. Thanks to Jacopo for always organizing lovely day trips around with a special eye for good restaurants and cultural activities. Thanks to Carlo, Tommy, and the Lambs for all the fun I had in June and to Severino and the Crocchette for the amazing trip to Salento.

Coming back home to Sicily is always special. I want to thank Elisa and Raimondo for being such good friends and for sticking with me no matter the geographical distances. Thanks to Carmelo for all the precious advice and sharp analysis on academia and the support during the last bits of writing. Cheers to Gianfranco and Marina for traveling all the way here for the defense, I really appreciate this.

A big shout out to the Sacchitello group, a bunch of talented and amazing friends that make me feel as if we all never left home. Among these, I want to thank Mauro for taking up the task of being my paranymph. He has been constantly present in my life since middle school, always making sure I wouldn't take problems too seriously. Thanks for boosting the mood on every occasion and for the loads of fun stuff you have got me into.

Furthermore, big thanks to my other paranymph Loret(t)a. In the last years, we have faced together a lot of challenges always with a touch of sarcasm and humor. I am amazed to see what a great scientist she has become and I am sure her future is bright. Thanks for being such a loyal and pleasant traveling companion during this adventure.

The nicest surprise of last year was certainly Sara. Thanks for being so lovely and patient with me. Grazie per avermi regalato leggerezza senza mai essere superficiale.

I would like to conclude with my family. Their unconditional support, encouragement, and love have always been crucial in my life.

About the author

Andrea was born in Catania (Sicily, Italy) on April 26th 1992. He grew up in Piazza Armerina, a small town in the heart of Sicily, where he attended high school. During that time he got passionate about Physics and won the regional phase of the Physics Olympiad thus participating in the national competition. In 2011, Andrea moved to study Physics at the University of Catania within the honors program of the Scuola Superiore di Catania (SSC). He got his bachelor's degree cum laude with a thesis about Au quantum plasmonic waveguides under the supervision of prof. Piccitto. He continued his studies at the University of Catania within the Condensed Matter Physics track. In 2016, he moved to Stanford University (California, USA) to carry out his master's research project in the group of prof. dr. Brongersma and under the supervision of prof. dr. Priolo. In his master's thesis, he used coupled-mode theory to design metasurfaces that act as broadband and efficient anti-reflection coatings by combining Mie and Fabry-Perot resonances and has demonstrated these experimentally. Shortly after, he obtained his master's degree cum laude and joined the group of prof. dr. Polman at AMOLF first as an intern and later as a Ph.D. student focusing on the theoretical analysis, fabrication, and characterization of optical metasurfaces for all-analog processing/computation and photovoltaic applications. In 2019, he obtained his diploma degree from the SSC cum laude. During his Ph.D., Andrea visited the group of prof. dr. Alù at UT Austin (Texas, USA) and CUNY-ASRC in New York (New York, USA) and the group of prof. dr. Engheta at University of Pennsylvania in Philadelphia (Pennsylvania, USA). In 2020, he was awarded the Piero Brovetto prize from the Italian Physical Society. The results of his research are shown in this thesis.

During his free time, Andrea enjoys running, playing tennis and football, and hanging out with friends. He loves traveling and often escapes to Rome and to Sicily.

La leggerezza per me si associa con la precisione e la determinazione,
non con la vaghezza e l'abbandono al caso.

Lezioni americane - Italo Calvino